STUDIES ON GAUGE-LINK SMEARING AND THEIR APPLICATIONS TO LATTICE QCD AT FINITE TEMPERATURE

A thesis submitted to

Tata Institute of Fundamental Research, Mumbai, India

for the degree of

Doctor of Philosophy

in

Physics

By

Nikhil Karthik

Department of Theoretical Physics

Tata Institute of Fundamental Research

Mumbai - 400 005, India

May, 2014

Final Version Submitted in June, 2014

Declaration

This thesis is a presentation of my original research work. Wherever contributions of others are involved, every effort is made to indicate this clearly, with due reference to the literature, and acknowledgement of collaborative research and discussions.

The work was done under the guidance of Professor Sourendu Gupta, at the Tata Institute of Fundamental Research, Mumbai.

(Nikhil Karthik)

In my capacity as the supervisor of the candidate's thesis, I certify that the above statements are true to the best of my knowledge.

(Sourendu Gupta)

Acknowledgments

Collaborators

This thesis is based on the work done in collaboration with Sourendu Gupta.

To My Parents

Contents

Synopsis

Introduction

Quantum Chromodynamics (QCD) is the part of the standard model of particle physics which describes the strong interaction between quarks which is mediated by gluons. Since the long distance behaviour of QCD is not amenable to perturbative calculations, one has to resort to alternatives to calculate, for example, the spectrum of hadrons or to study the confinement-deconfinement cross-over (at temperature T_c) known to exist in very hot hadronic matter. Lattice QCD [1–3] offers a first principles numerical computation of the properties of hadronic matter.
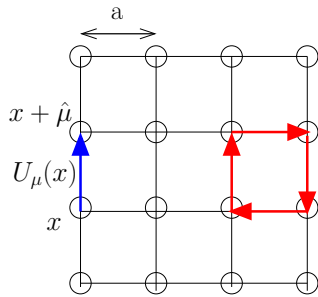
Figure 1: Space-time is discretized with the lattice spacing as a. The gauge-link, $U_\mu(x)$, lives on the link connecting the lattice site, x, to $x+\hat{\mu}$. The smallest Wilson loop, trace of which is the plaquette, is shown in red.
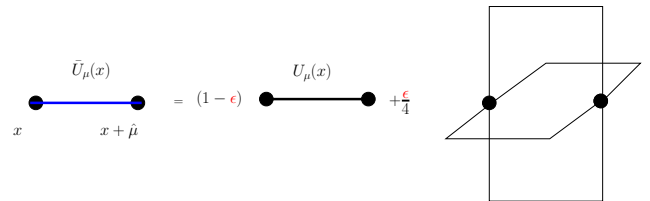
Figure 2: Construction of APE smeared link. The APE smeared link (blue) is constructed as a weighted sum of the original thin-link and the neighbouring paths (staples in this case) connecting the same two points. The resulting link is projected to SU(3).

QCD is a non-abelian quantum field theory with the symmetry group as SU(3). Like any generic quantum field theory, QCD needs to be regulated and lattice QCD provides

an ultra-violet (UV) regulator through the discretisation of space-time, as shown schematically in Figure 1. The lattice spacing, a, acts as a UV regulator. The gluon fields are introduced through the SU(3) gauge-links, $U_\mu(x)$, which live on the links connecting the lattice sites x to $x + \hat{\mu}$. In the continuum, the Grassmann-valued quark fields can be written in a component-wise manner as $\psi^{\alpha,i}(x)$, where the spin index, α, runs from 1 to 4, and the colour index, i, runs from 1 to 3. Naively introducing such quark fields at all the lattice sites automatically produces 16 different copies of itself called the doublers. A partial solution to the fermion doubling problem is offered by staggered quarks [4]. In this formulation, the staggered fields, $\chi^i(x)$, which have a single spin component, live on all lattice sites. The quark fields are constructed at even lattice sites, x, using the staggered fields on the 16 corners of the hypercube at x. Since 4 components are required for a Dirac fermion, this construction leads to 4 copies of each quark, called the tastes. Thus, the quark fields are given by $\psi^{\alpha,t,i}(x)$, where the taste index, t, runs from 1 to 4. The pion, which consists of one up and one down quark, now has 16 copies of itself called its taste partners. The staggered pion operators [5] are written as $\overline{\psi}^{\alpha,t}(x)\gamma_5^{\alpha\alpha'}\Gamma^{tt'}\psi^{\alpha',t'}(x)$, where the matrix γ_5 determines the pseudoscalar nature of the pion and Γ, which acts in the taste space of quarks, are products of the γ-matrices which determine the tastes of the pion taste partners.

Gauge invariant pure-gauge observables are constructed by taking the trace of products of gauge-links along closed loops (called Wilson loops). The trace of the smallest Wilson loop constructed out of four such link matrices is called a plaquette. The gluon part of the QCD action is proportional to the sum of plaquettes at all lattice sites, with the proportionality constant being a coupling, $\beta/3$. The staggered quark action can be written as

$$S_f = \sum_{x,y} \sum_{i,j=1}^{3} \overline{\chi}^i(x) D_{x,y}^{ij}(U) \chi^j(y), \tag{1}$$

with the Dirac operator, D, being a function of gauge links. In free field theory, S_f has an SU(4) taste symmetry. However, in the presence of gauge fields (at a finite lattice spacing), the taste symmetry is broken. As a consequence, only one of the pion taste partner (with $\Gamma = \gamma_5$) is the Goldstone boson while the others are heavier and non-degenerate. We measure the extent of this taste breaking through the taste splitting, δm_Γ, defined as the

difference between the mass of a taste partner, Γ, and the Goldstone pion *i.e.*,

$$\delta m_\Gamma \equiv m_\Gamma - m_{\gamma_5}. \tag{2}$$

In the continuum limit, the taste symmetry is restored and the taste splittings vanish.

Qualitatively, the reason for taste breaking is the following. The different tastes of the quark field, $\psi^t(x)$, are different combinations of the staggered fields, χ, on a hypercube. Thus, in the presence of gauge fields, the different tastes experience different $U_\mu(x)$. Therefore, we expect rapidly fluctuating gauge fields to increase the taste breaking. Gauge-link smearing is an algorithm to suppress such UV fluctuations in the gauge field. The algorithm is to replace $U_\mu(x)$ with a gauge covariant average over paths, $\overline{U}_\mu(x)$, connecting x to $x + \hat{\mu}$. Various smearing schemes differ in the paths that are included and in their weightage. We use four different smearing schemes, namely, APE [6], Stout [7], HYP [8], and HEX [9]. We show the construction of APE smeared link in Figure 2. The weightage given to the neighbouring paths over the original thin-link is determined by the smearing parameter, ϵ. In a fully dynamical simulation, one replaces the thin-links occurring in the quark action with smeared links *i.e.*, the improved Dirac operator is $D(\overline{U})$. Our studies are partially quenched and we use thin-links in the fermion action, while using smeared links whenever D occurs in the construction of operators, whose expectation values are to be determined. Thus, we improve the valence quarks while using unimproved sea quarks.

In this thesis, we show that the lattice corrections to measurements made with smearing, factorize into a smearing dependent part and a lattice spacing dependent part to a very good approximation. Such a factorization is exact for the plaquette calculated at the tree level in perturbation theory. This also occurs in the case of pion taste splittings in the confined phase (studied at $T = 0$) *i.e.*,

$$\delta m_\Gamma = f(\epsilon) g_\Gamma(a). \tag{3}$$

This is the reason smearing offers a computational advantage (provided the value of f is less than one). We discuss this in the next section.

We find smearing to perform better in reducing the taste breaking in the deconfined phase than in the confined phase. An improvement by a factor $f(\epsilon)$ in taste at $T = 0$ causes a factor $f^2(\epsilon)$ improvement in taste in the deconfined phase (as we show in a later section). With the taste breaking in the deconfined phase reduced by an order of magnitude with

optimal HYP smearing, we expect our measurements of physical quantities (in particular, the hadronic screening masses) in the deconfined phase to be nearer to the continuum after HYP-improvement.

Screening masses are the inverse screening lengths in the equilibrated QCD medium and they are measured from the spatial correlators of different quantum channels [10]. In the deconfined phase, weak coupling calculations [11, 12] predict that the screening masses approach the free field theory (FFT) value, μ_{FFT}, as

$$\mu = \mu_{\text{FFT}} + \alpha_S \Delta \quad \text{with} \quad \Delta > 0, \tag{4}$$

where α_S is the strong coupling constant at a momentum scale of $2\pi T$. Results with Wilson quarks [13] gave results that are closer to the FFT, though they differed in detail from weak coupling prediction. On the other hand, the staggered screening masses of the pseudoscalar (PS) and scalar (S) in the past studies with no gauge link smearing were found to lie much below μ_{FFT} at high temperatures. Improving the taste symmetry with optimal HYP-smeared valence quarks, we find the PS/S screening masses also to lie close to their lattice FFT value, for $T > 1.5T_c$. Also, they approach the lattice FFT value from above, as predicted. We find that the effect of taste breaking is to make the smallest eigenvalue of the Dirac operator to increase slowly above T_c, thereby affecting all screening phenomena.

Studies on Smearing

First, we demonstrate that smearing works by suppressing the UV more than the IR. For this, we divide the Brillouin zone of plaquettes into UV and IR regions, and we quantitatively study how smearing suppresses the power in the two regions differently. In this way, we are able to identify the optimal value of ϵ where the UV is maximally suppressed for each of the smearing schemes. We observe a similar effect on the extremal eigenvalues of D, which we take as the UV and IR in the quark sector.

We find that the effect of UV suppression and the effect of finite lattice spacing factorize. For the plaquette, P, such a factorization is exact perturbatively at the tree level, where we find

$$1 - P = \frac{2}{\beta} w(\epsilon), \tag{5}$$
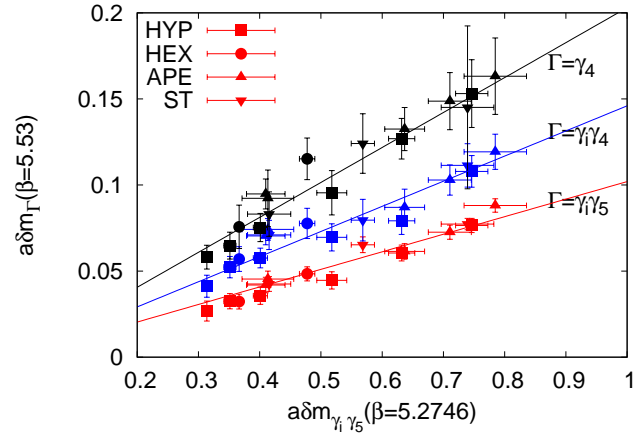
Figure 3: Evidence for factorization of pion taste splittings, δm_Γ, into smearing and lattice spacing effects. Different δm_Γ at a lattice spacing of $a = 0.17$ fm is plotted against $\delta m_{\gamma_i \gamma_5}$ at $a = 0.34$ fm, with both measured using the same smearing schemes and the smearing parameter values. The different symbols correspond to various smearing schemes, while the color specifies the taste Γ.
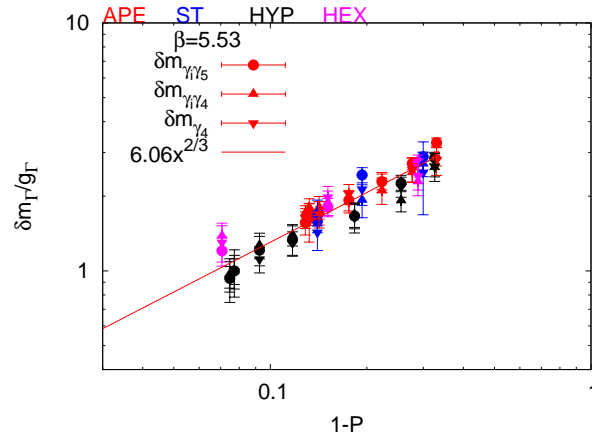
Figure 4: Universality in taste splitting as seen when plotted as a function of plaquette value at a fine lattice spacing of 0.17 fm. The data falls on a universal curve described by a power-law $x^{2/3}$. This is true at both coarse and fine lattices.

where the coupling, β, determines the lattice spacing, and the factor w is purely smearing dependent. Deviations from such a factorization shows up non-perturbatively due to a fine measurement of the plaquette, but they are less than a percent. A similar factorization occurs in the case of pion taste splittings, δm_Γ. Taste splitting with improved actions has been studied before [14–16], however in this thesis, we make a systematic study of it, by treating the smearing parameter as an independent variable. Doing so, we find the splitting to factorize as

$$\delta m_\Gamma(\epsilon, a) = f(\epsilon) g_\Gamma(a), \tag{6}$$

for a taste and lattice spacing dependent factor g_Γ, and a purely smearing dependent factor, f, defined such that $f = 1$ at $\epsilon = 0$. An evidence for such a factorization is shown in Figure 3, where we plot the pion taste splittings at a lattice spacing, $a = 0.17$ fm, against a taste splitting at $a = 0.34$ fm, such that both of them are measured using the same smearing schemes and the same values of ϵ. The linear dependence seen universally across the different smearing schemes and smearing parameter values is possible only if there is such a factorization. Through this study, we understand that gauge-link smearing offers a computational advantage by making the taste splittings nearer to zero at a finite a due to the factor f, while their dependence on a remain the same. This also means that approaching the continuum limit is mandatory even with smearing, just as in the case of thin-links.

We find an interesting connection between the effect of smearing in the quark and gluon sectors. Even though the pion taste splittings are smearing scheme and taste channel dependent, it shows a behaviour which is universal across the different smearing schemes when plotted as a function of the plaquette value. This result is shown in Figure 4. The universal dependence on plaquette is of the form

$$\frac{\delta m_\Gamma(\epsilon, a)}{g_\Gamma(a)} \approx A(1 - P)^{2/3}, \tag{7}$$

for a constant A which is universal for all the pion taste partners at a given β. The exponent is also universal and takes the value 2/3. However, this universal behaviour breaks down for very large values of ϵ.

Application of Smearing to Finite Temperature

A major part of this thesis concerns the applications of smearing to finite temperature QCD, with the main emphasis on hadronic screening correlators and masses. The screening masses are important after the advent of relativistic heavy ion collisions as they determine the finite volume effects in a fireball. They are also interesting from a theoretical standpoint as they address the nature of the deconfined phase of QCD.

As shortly discussed in the introduction, the screening masses presented a confused picture in the deconfined phase: most computations were performed with staggered quarks [10, 17–20], and these indicated that there are strong deviations from weak-coupling prediction (see eq. (4)). On the other hand, computations with Wilson quarks gave results that are closer to the free field theory [13]. Since, the continuum limit of the screening masses from all quark formulations have to agree, the observed effect can only be a lattice artifact. From our study of smearing, we expect that the lattice corrections to staggered screening masses, μ, in the deconfined phase to behave as

$$\mu = \mu_{cont} - k(\epsilon)a^2,\tag{8}$$

with a smearing dependent factor, $k(\epsilon)$, which is reduced with smearing. This motivates us to study staggered screening masses with optimal gauge-link smearing to obtain measurements nearer to the continuum at finite lattice spacings.

Unexpectedly, we find an even more convincing reason to use gauge-link smearing for the problem. In Figure 5, we show the taste splitting, $\delta\mu_\Gamma$, at $T = 2T_c$ as a function of the corresponding taste splitting, δm_Γ, at $T = 0$ for the taste $\Gamma = \gamma_i\gamma_5$. The different points correspond to the optimal ϵ in different smearing schemes. From the figure, we find that the two taste splittings are related quadratically:

$$\frac{\delta\mu_\Gamma}{T} \propto (a\delta m_\Gamma)^2.\tag{9}$$

We explain this observation as due to complete or almost complete restoration of taste symmetry in the limit of vanishing quark mass. If smearing decreases δm_Γ by a factor $f(\epsilon)$, then it decreases the splitting in the deconfined phase by $f^2(\epsilon)$. Thus, smearing works more effectively in the deconfined phase than in the confined phase.

Using optimal HYP-improved staggered valence quark, we determine the pseudoscalar
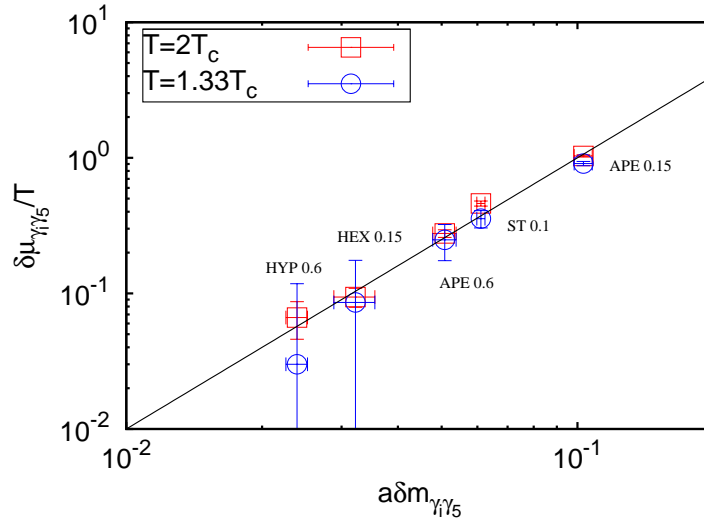
Figure 5: Super-linear improvement of taste splitting in deconfined phase compared to the confined phase. The taste splitting $a\delta m_\Gamma$ at $T = 0$ is plotted against the splitting of the corresponding screening masses, $a\delta\mu_\Gamma$, at $2T_c$, both at same lattice spacing and $\Gamma = \gamma_i\gamma_5$. The line $y = 100x^2$, is superposed to indicate the slope.

(PS), scalar (S), vector (V), axialvector (AV) and nucleon (N) screening masses in the temperature range from $0.92T_c$ to $2T_c$. Our result for the hadron screening spectrum with optimum HYP smearing, as a function of temperature is shown in Figure 6. The most important result in this thesis, is the PS/S screening masses lying close to the lattice FFT value at high temperatures. The blue and green bands are predictions from perturbative calculations [11, 12]. Both the calculations predict that irrespective of quantum number, all the meson screening masses have to approach the FFT value from above. Our result, given about 15% uncertainty due to scheme dependence at a finite cut-off, indeed shows a similar behaviour and a close agreement with the weak coupling predictions. This behaviour remains robust when the Goldstone pion mass is decreased from 240 MeV to 190 MeV. With the results for PS screening mass at $2T_c$ from two different lattice spacings, we roughly estimate using eq. (8) that the slope, $k(\epsilon)$, with optimal HYP is about 5 times smaller than that with the thin-link.

The rapid approach to behaviour similar to weak-coupling theory has implications for the spectrum of the staggered Dirac operator. It was shown in an earlier study with thin-link quarks that a gap developed in the massless staggered eigenvalue spectrum a little
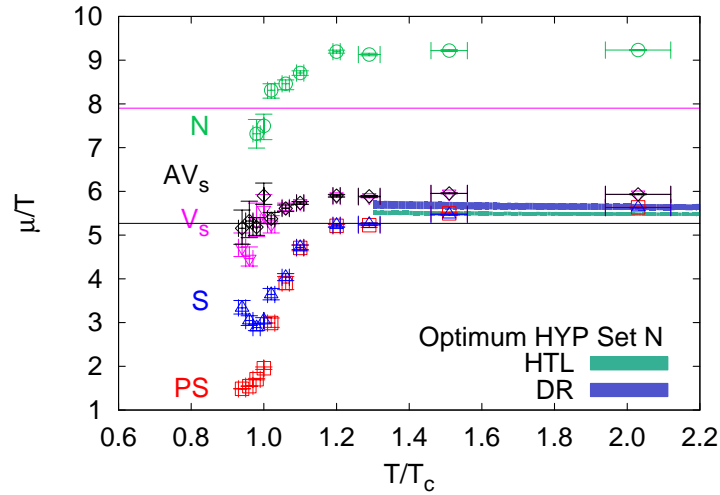
Figure 6: Hadron screening masses for the ensemble with pion mass of about 190 MeV and on lattice with the temporal extent $N_t = 4$, using optimum HYP-smeared correlators. The horizontal lines are the lattice free theory screening mass for the nucleon and the mesons respectively. DR denotes the weak-coupling prediction of [11]; HTL is the prediction from [12].
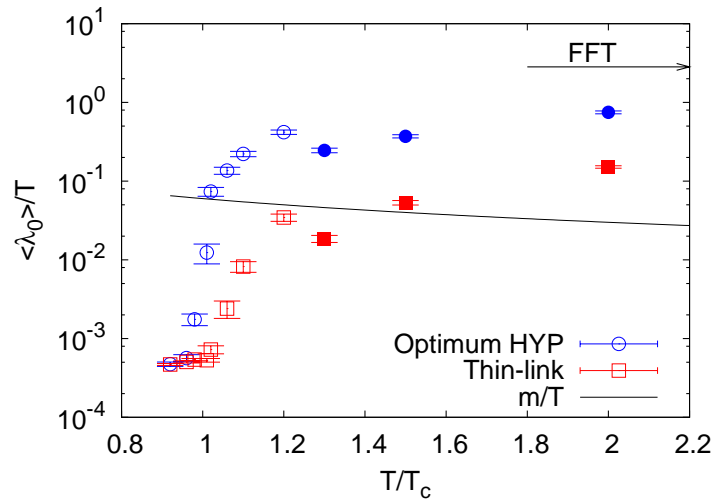
Figure 7: Ensemble averaged smallest eigenvalue of the massless staggered Dirac operator, $\langle \lambda_0 \rangle$, for the ensemble with the pion mass of about 190 MeV, with and without smearing. LT specifies the aspect ratio of the lattice.

above T_c, and that the hot phase contained localized Dirac eigenvectors [21]. In this thesis, we study the gap by measuring the smallest eigenvalue of the massless staggered Dirac operator, λ_0. As can be seen in in Figure 7, with reduced taste breaking, it rises very rapidly between T_c and $1.06T_c$. Whereas, with no improvement, λ_0 rises at significantly higher temperature, thereby affecting all screening phenomena in the deconfined phase.

Publications

- S. Gupta and N. Karthik,
  Hadronic Screening with Improved Taste Symmetry,
  Phys. Rev. D 87, 094001 (2013).

- S. Gupta and N. Karthik,
  UV Suppression by Smearing and Screening Correlators,
  PoS LATTICE 2013, 025 (2013).

- N. Karthik,
  A Concise Force Calculation for Hybrid Monte Carlo with Improved Actions,
  arXiv:1401.1072 (2014).

Chapter 1

Introduction

1.1 Quarks and Hadrons

Science has come a long way from philosophizing about the nature of building blocks of matter to a point where we could test the nature of such fundamental particles experimentally. Combined theoretical and experimental efforts have culminated in the now well-tested standard model of particle physics which describes the interactions between different fundamental particles [22]. Quantum Chromodynamics (QCD) is the part of the standard model which describes the strong interaction between the quarks mediated by gluons. Bulk of the visible matter in the universe is made of neutrons and protons. These particles along with a plethora of others such as π, K, ρ, Ω *etc.*, classified as hadrons, are tightly bound systems of quarks and gluons confined within a few femtometers. It is an intriguing observation that the final states detected in collision experiments are always hadrons, and never quarks and gluons separately. The evidence for quarks and gluons rather comes indirectly when hadrons are probed through deep inelastic scattering of electrons, an experiment which is analogous to the Rutherford gold-foil experiment [23]. These experiments suggested that the constituents of hadrons behaved like free particles [24]. These aspects are unique to the QCD part of the standard model — the long distance behaviour being described in terms of hadrons while the short distance behaviour being in terms of free quarks and gluons.

When a bulk of such hadronic matter is heated to high temperaratures or compressed to high densities, its behaviour changes. In fact, quarks and gluons get deconfined in a phase called quark gluon plasma (QGP) [25]. Both experimental and theoretical efforts

are underway to understand the properties of hadronic medium under extreme conditions.

Our current theoretical understanding of the phases of hadronic matter from first principles is through the technique of lattice QCD, which is computational in nature. Lattice QCD discretizes space-time into a four dimensional lattice. Effects of such a discretization remain in any computation doable on a computer. Finding algorithms to reduce such lattice artifacts is an important and still evolving sub-field of lattice QCD. This thesis is an exploration of one such method called gauge-link smearing. We show that smearing is indispensable in the study of static correlation lengths in a hot hadronic medium.

We first briefly review the methods of lattice QCD. This involves a discussion on staggered fermions and taste symmetry breaking which forms a central theme in this thesis. Then we remind the reader about different aspects of the phase diagram of QCD. Through this, we introduce the reader to screening lengths in the plasma, and to the problem thereby.

1.2   A Brief Introduction to Lattice QCD

1.2.1   QCD in the continuum

The standard model of particle physics is formulated as a renormalizable quantum field theory based on the principle of gauge-invariance *i.e.*, the physics should not be dependent of certain local transformations on the fields. The QCD part of the standard model is by itself a stand-alone QFT invariant under $\mathrm{SU}(3)$ color gauge transformations — Each flavour of quark is described by a fermion field $\psi^a(x)$ with the color components $a = 1, 2, 3$, and the gluons are described by $\mathrm{SU}(3)$ algebra-valued bosonic fields $A_\mu(x)$, such that they transform under a local $\mathrm{SU}(3)$ transformation $\Omega(x)$ as

$$\psi'(x) = \Omega(x)\psi(x) \quad \text{and} \quad A_\mu(x) = \Omega^{-1}(x)A_\mu(x)\Omega(x) + i\left(\frac{\partial}{\partial x}\Omega(x)\right)\Omega^\dagger(x). \qquad (1.1)$$

Henceforth in this thesis, we consider only the degenerate light up and down quarks each of bare mass m *i.e.*, the number of flavours $N_f = 2$. The dynamics of these fields are governed by the action S_{QCD} which has to be invariant under the above gauge-transformation. It

turns out that the action is the simplest of many such possibilities, and it is given by

$$S_{\text{QCD}} = S_{\text{quark}} + S_{\text{glue}}, \tag{1.2}$$

with the quark part of the action being

$$S_{\text{quark}} = \sum_{f=1}^{N_f} \int d^4x \overline{\psi}_f(x) \left[\gamma_\mu D_\mu + m\right] \psi_f(x) \quad \text{with} \quad D_\mu = \partial_\mu + iA_\mu, \tag{1.3}$$

and the gluon part of action as

$$S_{\text{glue}} = \frac{1}{2g^2} \int d^4x \text{Tr}\left(F_{\mu\nu}F_{\mu\nu}\right) \quad \text{with} \quad F_{\mu\nu} = -i[D_\mu, D_\nu]. \tag{1.4}$$

The operator $\gamma_\mu D_\mu + m$ is called the Dirac operator. Any regularization of QCD should not break gauge symmetry, and one such method is the lattice regularization which is discussed next.

Using this action, one could calculate the expectation values of different operators at a temperature $T = 0$ or $T > 0$ using the path integral of QCD. At $T > 0$, the temporal direction has to be of a finite extent $1/T$, with a periodic boundary condition for gluons, and an anti-periodic boundary condition for quarks. This ensures that quarks follow Fermi-Dirac statistics [26].

1.2.2 Gauge-fields on Lattice

A gauge-invariant way to regularize QCD is through discretization of space-time into a 4d lattice with a lattice spacing a, and the fields being "gauge-links" and quark fields [27]. The lattice spacing acts as the UV regulator for the path integrals. The temporal extent of the lattice is N_t in lattice units, and for simplicity, we take the lattice to have N_s lattice sites along all the spatial directions. It is a common practice to refer to such a lattice as an $N_t \times N_s^3$ lattice.

The gauge-links $U_{x,\mu}$ are 3×3 SU(3) matrices which live on the links connecting lattice sites x to $x + \hat{\mu}$. The quark fields $\psi(x)$ live on lattice sites. We defer a discussion on quarks on lattice to the next subsection. The boundary conditions depend on the temperature T. If $T = 0$, then periodic boundary condition is imposed on all four directions for both
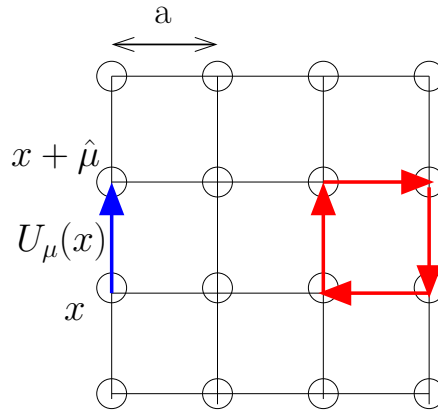
Figure 1.1: Space-time is discretized with the lattice spacing as a. The gauge-link, $U_\mu(x)$, lives on the link connecting the lattice site, x, to $x + \hat{\mu}$. The smallest Wilson loop, trace of which is the plaquette, is shown in red.

quarks and gauge-links. For a finite temperature calculation, the temporal direction is anti-periodic for quarks, and the temperature is related to the lattice spacing through

$$T = \frac{1}{N_t a}. \tag{1.5}$$

Under a gauge-transformation $\Omega(x)$, the gauge-links transform as

$$U'_\mu(x) = \Omega(x) U_{x,\mu} \Omega^\dagger(x + \hat{\mu}). \tag{1.6}$$

These gauge-links are the gauge-transporters which ensure that $\psi(x)$ and $U_{x,\mu}\psi(x + \hat{\mu})$ transform identically under gauge-transformations. With this identification, for small enough lattice spacing a, $U_{x,\mu} \approx \exp(iga A_\mu(x))$. Due to the above transformation property, gauge-invariant pure-gluonic quantities can be constructed by taking the trace of products of gauge-links along closed loops. The simplest such object is the plaquette

$$P_{\mu\nu}(x) = \text{ReTr}\left[U_{x,\mu} U_{x+\hat{\mu},\nu} U^\dagger_{x+\hat{\nu},\mu} U^\dagger_{x,\nu}\right]. \tag{1.7}$$

This is shown as the red loop in Figure 1.1. The simplest action for the gauge-field is

therefore proportional to the plaquette

$$S_g = \frac{\beta}{6} \sum_{x,\mu>\nu} \left[1 - P_{\mu\nu}(x) \right].$$ (1.8)

Not surprisingly, in the limit $a \to 0$, the above action reduces to the gluon action in eq. (1.4). This leads to the identification $\beta = 6/g^2$. The above form of the gauge-link action is called the Wilson action. At finite lattice spacings, S_g differs from eq. (1.4) by $\mathcal{O}(a^2)$.

Due to asymptotic freedom, the bare coupling g decreases when the lattice spacing a is decreased, while maintaining constant physics. This offers a handle on tuning the lattice spacing by changing the value of the inverse coupling β — larger the value of β, smaller the lattice spacing is. This also means that at a given N_t, one can tune to higher temperatures by increasing the value of β.

1.2.3   Tastes of Staggered Quark

We noted in the last subsection that the quark fields $\psi(x)$ live on lattice sites x. Component-wise, the quark fields are of the form $\psi_f^a(x)$, where a is the color index, and f is the flavour. The lattice Dirac operator D could be constructed using a discretized version of the gauge-covariant derivative $\partial_\mu + iA_\mu$,

$$\Delta_\mu \equiv \frac{1}{2} \left[U_{x,\mu} \delta_{x+\hat{\mu},y} - U_{x-\hat{\mu},\mu}^\dagger \delta_{x-\hat{\mu},y} \right].$$ (1.9)

Doing so, the naive fermion action is

$$S_{\text{naive}} = \sum_{f=1}^{N_f} \sum_{x,y} \overline{\psi}_f^a(x) D_{x,y}^{ab} \psi_f^b(y) \quad \text{where} \quad D_{xy} = \frac{1}{2} \sum_\mu \gamma_\mu \Delta_\mu + m\delta_{x,y}.$$ (1.10)

This immediately leads to 16 copies of each flavour of quark, also called the doublers, or tastes . This can be seen easily by taking the case of zero quark mass in free field theory *i.e.*, by setting all the gauge-links to identity. In this case, the Fourier transform of the Dirac operator is diagonal, and the quark propagator is

$$D^{-1}(k) = \frac{\sum_\mu \gamma_\mu \sin(k_\mu)}{\sum_\mu \sin^2(k_\mu)}.$$ (1.11)
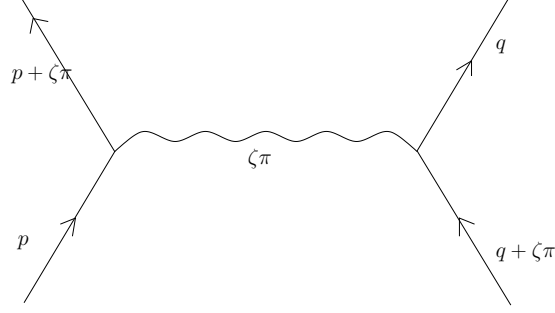
Figure 1.2: A taste mixing process. Two quarks, one at a low momentum mode around $k = 0$ and another around $k = \zeta\pi$, interact via an ultra-violet gluon of momentum $\zeta\pi$, and exchange taste.

In addition to the pole at $k = 0$ which corresponds to the quark we introduced, there are 15 additional poles at the corners $\zeta\pi$ of the Brillouin zone, where $\zeta_\mu = 0$ or 1. This is the infamous fermion doubling problem. As discussed in [28], it is also possible to see this fermion doubling by constructing interpolating fields $\Psi^\zeta(x)$ for the 16 tastes whose low momentum modes are around $k = \zeta\pi$.

Staggered fermion formulation [2, 4, 28] is a clever way of reducing the number of tastes from 16 to 4 by noting that the transformation $\psi(x) \to \psi'(x) = \left(\prod_\mu \gamma_\mu^{x_\mu} \right) \psi(x)$ makes the Dirac operator diagonal in spin space:

$$D_{xy} = \frac{1}{2} \sum_\mu \eta_\mu \left[U_{x,\mu}\delta_{x+\hat{\mu},y} - U_{x-\hat{\mu},\mu}^\dagger \delta_{x-\hat{\mu},y} \right] + m\delta_{x,y} \quad \text{where} \quad \eta_\mu(x) = (-1)^{x_1+...x_{\mu-1}}.$$

$$(1.12)$$

Except for one of the spin component χ in ψ', the rest of the components are set to zero. This procedure reduces the number of tastes from 16 to 4 (refer [28]). The interpolating fields constructed out of the staggered fields within a hypercube are of the form $\Psi^{\alpha,t}(x)$, where α is the usual spin index while t is the taste index ranging from 1 to 4. These are the four tastes of staggered quark.

As long as there is no mixing between the different tastes, it is simple to remove them by taking the 1/4-th root of $\det D$[1]. This is the case in the absence of gauge-fields, where one has an exact $SU(4)$ taste symmetry. However, in the presence of gauge-links, it is possible for a quark with a given taste to interact with a hard gluon of momentum $\approx \zeta\pi$,

---

[1]$\det D$ is obtained by integrating the Grassmann valued fields in the path integral.

and remain a low momentum quark, but of a different taste. One such process is shown in Figure 1.2. This leads to the $\mathcal{O}(\alpha_s a^2)$ taste breaking effects. This is an important technical aspect that we study in this thesis.

There are other formulations of quarks on a lattice which tackle the problem of fermion doubling differently *eg.*, Wilson quarks and overlap quarks [3]. But these formulations do not suffer from taste breaking artifacts.

1.2.4 Staggered Hadron Spectroscopy

The spectrum of staggered hadrons [5, 29, 30] is complicated due to the extra taste degree of freedom. Pion, for example, has a valence up quark and a down quark. Since each flavour has four different tastes, there are 16 different taste partners for a pion. In general, the staggered meson operators are of the form $\overline{\Psi}^{\alpha',t'}(x)\Gamma_T^{t't}\Gamma_D^{\alpha'\alpha}\Psi^{\alpha,t}(x)$, where Γ_D and Γ_T are products of the Dirac gamma matrices, and they act in the spin and taste space respectively. For a pion $\Gamma_D = \gamma_5$. When expressed in terms of the staggered fields χ, meson operators are of the form

$$\mathcal{O}_l(x) = \phi_l(x)\overline{\chi}(x)\nabla\chi(x), \tag{1.13}$$

where $\phi_l(x)$ are phases which determine the quantum channel l, and ∇ are products of gauge-covariant lattice derivative operators Δ_i along directions i in a time slice. Local mesons are those which have $\nabla = 1$, or equivalently as those with $\Gamma_D = \Gamma_T$. If ∇ involves only a single derivative Δ_i, the meson is said to be one-link separated. Similar such definitions for two-link and three-link separated mesons. We refer the reader to [29] for a detailed list of staggered phases for the taste partners of mesons. The masses m_l of the hadrons are determined by the exponential decay of the zero momentum correlation functions

$$C_l(t - t_o) = \sum_{\mathbf{x}} \langle \mathcal{O}_l(\mathbf{x}, t)\, \mathcal{O}_l(\mathbf{x_o}, t_o) \rangle \xrightarrow{\lim |t-t_o| \to \infty} e^{-m_l(t-t_o)} \tag{1.14}$$

for sufficiently large $t - t_o$, with summation over $\mathbf{x}$ in the time-slice containing t. We have been cavalier with regard to the presence of staggered even-odd oscillations and the presence of periodic boundary condition. We come back to the discussion on how to extract masses of staggered hadrons in the next subsection.

In free field theory (FFT), all the taste partners of a meson are degenerate due to taste

symmetry. When interactions are turned on, the taste symmetry is explicitly broken, and thereby the masses of the taste partners get split. It is the local pion with $\Gamma_D = \Gamma_T = \gamma_5$ which is the pseudo-Goldstone boson at finite lattice spacing, while the other pion taste partners remain heavier. We use this fact to measure the degree of taste breaking. We define the pion taste splitting δm_Γ as the difference between the mass m_Γ of a pion taste partner with $\Gamma_T = \Gamma$, and the mass m_{γ_5} of the Goldstone pion:

$$\delta m_\Gamma = m_\Gamma - m_{\gamma_5}. \tag{1.15}$$

These splittings vanish in the case of FFT as well as in the continuum, where taste symmetry is restored.

Quark Sources

Extended quark sources help to improve the overlap with the hadronic states — we use wall [31] and Wuppertal [32] quark sources, while using point sink in our zero temperature studies. The extended quark fields X are constructed out of the original fields, χ, as

$$X^a(x) = \sum_{\text{t-slice}} S_{x,y}^{ab} \chi^b(y), \tag{1.16}$$

where the super-scripts are color indices. The choice of the smearing kernel $S_{x,y}^{ab}$ determines the quark source. For a wall source, $S_{x,y}^{ab} = \delta_{ab}$ for all y lying in the same time-slice as x and with all its coordinates even. Otherwise $S_{x,y}^{ab} = 0$ [2]. We gauge-fix the configurations to the Coulomb gauge [33] before using Wall source. The Wuppertal source is constructed in order to remove the rapid fluctuations in quark fields. The smeared quark field is $X = \exp(\sigma^2 \nabla)\chi(x)$, where ∇ is the gauge covariant 3d Laplacian

$$\nabla_{xy} \equiv -6\delta_{xy} + \sum_{\pm\mu=1}^{3} V_{x,\mu}^{(n)} \delta_{x,y-\mu}. \tag{1.17}$$

The matrices $V_{x,\mu}^{(n)}$ are the n-level 3d-APE smeared links (*i.e.*, the APE smearing involves only the staples lying within the time-slice). Taking $\exp(\sigma^2\nabla) = \lim_{N\to\infty}(1 + \sigma^2\nabla/N)^N$,

---

[2]We discuss the modification for wall source at finite temperature when we discuss about screening masses later in this chapter

Wuppertal smearing is implemented by N successive application of the kernel

$$S_{x,y} = \delta_{xy} + \kappa \nabla_{xy} \tag{1.18}$$

to a point source. The parameter κ is σ^2/N.

Extracting Masses by Fit

This subsection deals with the determination of the ground state screening masses through fit to the respective correlators. The correlator C_γ for a a meson γ has contributions also from its parity partner γ' which occurs as a contribution which oscillates in sign between even and odd separations. When the ground state screening masses in the oscillating and non-oscillating components of a meson screening correlator, it can be parametrized as

$$C_\gamma^{fit}(t) = A_\gamma \cosh\left[m_\gamma\left(\frac{N_t}{2} - t\right)\right] + (-1)^t A'_\gamma \cosh\left[m'_\gamma\left(\frac{N_t}{2} - t\right)\right]. \tag{1.19}$$

The alternating component is absent for the Goldstone pion (PS) and its local time taste partners. Following [5], the nucleon correlator is parametrized as

$$
\begin{aligned}
C_N^{fit}(t) = A_N &\left\{\exp\left[m_N\left(\frac{N_t}{2} - t\right)\right] + (-1)^t \exp\left[-m_N\left(\frac{N_t}{2} - t\right)\right]\right\} \\
&+ A'_N\left\{(-1)^t \exp\left[m'_N\left(\frac{N_t}{2} - t\right)\right] + \exp\left[-m'_N\left(\frac{N_t}{2} - t\right)\right]\right\}.
\end{aligned}
\tag{1.20}
$$

We extract the masses, m_γ, m_N, and the remaining parameters from the measured correlators, $C_\gamma(z)$, by fitting to the above forms over z lying in a range $[z_{min}, z_{max}]$. The number of data points being fitted in this range, $n_{fit} = z_{max} - z_{min} + 1$, are at least 3 in the case of pseudoscalar, while it is at least 5 for all other channels. This is to ensure that there is at least one degree of freedom in the fit. The best fit parameters are obtained by minimizing [10]

$$\chi^2 = \Delta^T \Sigma^{-1} \Delta, \tag{1.21}$$

where Δ is a n_{fit}-tuple with the elements

$$\Delta_z = C_\gamma(z) - C_\gamma^{fit}(z). \tag{1.22}$$

The covariance between the measurements at two different z are taken care of by using the $n_{fit} \times n_{fit}$-dimensional covariance matrix, Σ, whose estimator is given by

$$\Sigma_{z,z'} = \frac{1}{N(N-1)} \sum_{i=1}^{N} \left[C^{(i)}(z) - C(z) \right] \left[C^{(i)}(z') - C(z') \right], \qquad (1.23)$$

where $C^{(i)}$ is the correlator measured on the i-th configuration.

1.2.5   Continuum Limit and Improved Operators

In the end of a lattice computation, it is mandatory to take the $a \rightarrow 0$ limit, while keeping the ratios of physical quantities, such as m_π/m_ρ, constant in order to make contact with experiments. This process goes by the name of "taking the continuum limit". In a typical lattice QCD simulation, the continuum limit is taken by repeating the calculations at different values of lattice spacing on the same line of constant physics. One then extrapolates to the continuum by knowing how the physical quantity scales with a (for small enough a). Even though the whole process sounds simple, it is computationally expensive — the inversion of Dirac operator through iterative methods, such as the conjugate gradient, takes more iterations to converge at smaller lattice spacings. Also, there is an increase in the auto-correlation times encountered in the generation of gauge-configurations through Monte Carlo methods. In addition to that, if one uses approximate algorithms such as the R-algorithm [34], our studies (discussed in Appendix A) suggest that one has to push the parameters of the algorithm towards more expensive parts of the parameter space. Thus, it is essential to reduce the computational cost by reducing the lattice spacing corrections to observables on the lattice.

There are two important techniques available for reducing lattice artifacts — Gauge-link smearing and Symanzik improvement [35]. Symanzik improved lattice operators are constructed by adding irrelevant operators, whose coefficients are tuned to cancel the lattice spacing corrections to a desired order *eg.*, the Clover term [36] in the case of Wilson quarks, and the "p4 improvement" for staggered quarks [37]. On the other hand, Gauge-link smearing is motivated as a method to improve lattice measurements by suppressing the ultra-violet fluctuations in the gauge-field, since they are sensitive to the non-zero lattice spacing. Its algorithm, roughly, is to replace the links, $U_\mu(x)$, with a gauge covariant average over paths, $V_\mu(x)$, connecting x to $x + \hat{\mu}$. While Symanzik improvement is
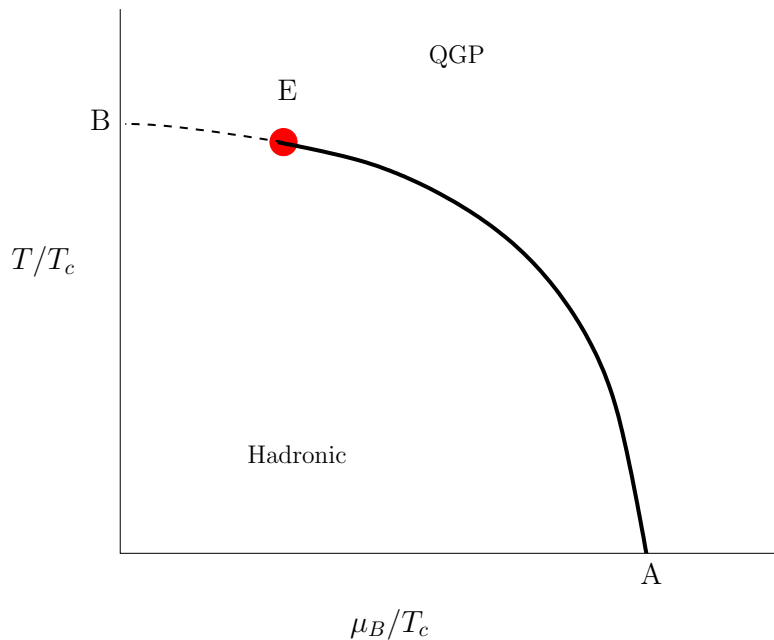
Figure 1.3: A schematic phase diagram of QCD. The deconfinement transition is believed to be first-order along the solid line which ends in the critical end-point E. Beyond E, it is a cross-over, which is indicated by the dashed line. Region close to $\mu_B = 0$ axis is accessible to lattice QCD.

firmly footed on Renormalization Group, the method of gauge-link smearing needs to be understood in a greater detail, even though the motivation is clear.

In Chapter 3, we discuss our studies on the effects of gauge-link smearing on the ultra-violet modes in the gauge-fields, and their effect on taste breaking at zero and finite temperature.

1.3   Aspects of Hot and Dense QCD

1.3.1   Phase Diagram

The phase diagram of QCD as a function of baryon density and temperature is still being understood theoretically and experimentally. For a recent short review on this topic, reader can refer to [38]. The property of asymptotic freedom of QCD means that the quarks are weakly interacting at short distance scales or at high momentum transfer. Thus, at very

temperature when the typical momentum is of $\mathcal{O}(T)$, the quarks are weakly interacting. The other extreme of large baryon density, the interaction again becomes weak. This leads to the existence of quark-gluon plasma at high temperatures and densities, where the quarks and gluons get deconfined. The properties of this phase of matter is being probed through ultra-relativistic collision of heavy ions at Relativistic Heavy Ion Collider at BNL and the ALICE experiment at LHC.

Instead of baryon-density, it is customary to use baryon chemical potential μ_B which in terms of quark chemical potentials μ_u and μ_d is $3(\mu_u + \mu_d)/2$ [3]. The schematic of a simple version of the phase diagram is shown in Figure 1.3. There are two different phases in the diagram — confined or the hadronic phase, and the deconfined or the QGP phase. The transition from one phase to the other is first-order along the solid line as expected from effective field theories.

From lattice QCD simulations [39], it is now well established that there is a cross-over between the two phases at $\mu_B = 0$ (denoted by B). These are determined by the positions of peaks of the susceptibilities of the Wilson line L and chiral condensate $\langle \overline{\psi}\psi \rangle$. They are defined as

$$L = \frac{1}{3}\text{ReTr}\prod_{t=1}^{N_t} U_{x,\hat{t}} \quad \text{and} \quad \chi_L = \langle L^2 \rangle - \langle L \rangle^2, \tag{1.24}$$

and

$$\langle \overline{\psi}\psi \rangle = \frac{T}{V}\frac{\partial}{\partial m}\ln Z \quad \text{and} \quad \chi_M = \frac{\partial}{\partial m}\langle \overline{\psi}\psi \rangle, \tag{1.25}$$

where Z is the partition function, and V is the spatial volume of the lattice. In the studies of [40] and [41], L and $\langle \overline{\psi}\psi \rangle$ were renormalized. The currently accepted values of the cross-over temperature T_c from $\langle \overline{\psi}\psi \rangle$ is about 155 MeV while that from L is about 170 MeV. It is interesting to note that, until recently, there seemed to be a disagreement between the values of T_c obtained by HotQCD collaboration which used p4-staggered quarks, and the one obtained by Budapest-Wuppertal-Marseilles (BMW) collaboration which used a version of gauge-link smearing called stout. The issue was resolved when it was found that the p4-staggered results suffered from larger lattice artifacts than the one with stout smearing. The agreement was further seen, when HotQCD collaboration used HISQ actions which combine a variant of gauge-link smearing with Symanzik improvement[42]. This was an early indication that taste breaking effects might play an important role in

---

[3]We are working with two light flavours of quarks.

certain aspects of finite temperature studies using staggered quarks.

It is believed that the first order line ends at a critical end-point E. Finding the position of such a critical point is of current challenge to both experiments and lattice QCD. There have been many attempts at finding the critical end-point on lattice [43–45]. The state-of-the-art prediciton on the position of the critical end-point from the Taylor series method [46] is that $T_E \approx 0.94 T_c$ and $\mu_E \approx 1.8 T_c$ [47].

1.3.2   Screening in Equilibrated Medium

Screening of a test charge by the medium is a well known phenomenon that one comes across in an electrical plasma. In the case of hadronic medium, the response of the medium to the introduction of sources of different hadronic quantum numbers could be studied [10]. Screening of a quantum number l is studied using the correlation between a source and sink $\mathcal{O}_l$ at two space-like separated points in an equilibrated medium. On a lattice, screening correlators are measured along one of the spatial directions (z in our case)

$$C_l(z - z_o) = \sum_{\mathbf{x}^\perp} e^{i\phi t} \left\langle \mathcal{O}_l^\dagger \left(\mathbf{x}^\perp, z\right) \mathcal{O}_l \left(\mathbf{x_o}^\perp, z_o\right) \right\rangle, \tag{1.26}$$

where $\mathbf{x}^\perp$ are the coordinates in the z-slice at z. For mesons, the phase $\phi = 0$. But for a nucleon, $\phi = \pi/N_t$ since it is the lowest frequency it can be projected to in the temporal direction. At large separations, the screening correlators decay exponentially [4].

$$C_l(z - z_o) \sim e^{-\mu_l(z - z_o)}, \tag{1.27}$$

and the exponent μ_l is the screening mass in the hadronic channel l. At $T = 0$, these screening masses are identical to the masses of the respective hadrons. At finite temperature, this is not true. However, the screening correlators are related to the spectral function at finite temperature. In the confined phase, the screening masses are dominated by the peaks in the spectral function at bound states of quarks and gluons. While for an ideal gas of quarks and gluons, the screening mass depends only the temperature as $2\pi T$ for mesons and $3\pi T$ for baryons. This cross-over between the two kinds of behaviour provides a probe to the presence of interactions in the medium.

---

[4]The effect of periodicity of lattice and parity partners are taken care of in the actual calculation by making use of eq. (1.19) and eq. (1.20) after the replacements $N_s \to N_t$ and $t \to z$.

Screening masses also control finite volume effects at finite temperature in equilibrium. Studies of the final state of fireballs produced in heavy-ion collisions indicate that they are near equilibrium. So the study of screening masses a little below the QCD cross over temperature, near the freeze out, should improve our understanding of experimental conditions. In addition, the vector screening masses below T_c should be of direct relevance to the study of mass spectra of dileptons and photons.

In this thesis, we study the screening masses μ_γ of the local mesons γ: the scalar (S), the spatial and temporal polarizations of vector (V_s and V_t), and the spatial and temporal polarizations of axial-vector (AV_s and AV_t). We also determine the screening mass of the nucleon, μ_N. We use wall source at finite temperature to improve the overlap with the ground-state, as well as to suppress the oscillating contribution from the parity partner.

Wall Source and Free Field Theory

The presence of anti-periodicity in the time direction requires a minor modification of the kernel, S, for the wall source — the smallest momentum to which the quark field can be projected to is the lowest Matsubara frequency π/N_t. Incorporating this modification, S for the wall source at finite temperature is

$$S_{xy}^{ab} = \exp(i\pi y \cdot \hat{t}/N_t)\delta_{ab} \qquad (1.28)$$

if y belongs to the same z-slice as that of x, and all the coordinate components of y are even. Otherwise, $S_{xy}^{ab} = 0$.

We use wall source for two reasons. Firstly, it offers a noise reduction by suppressing the staggered oscillations. Secondly, it removes the higher momentum components of the quark field. This lets us to extract a precise value of free field theory (FFT) value of screening masses on the lattice, unlike the case of point-source where a plateau in effective masses does not exist in FFT. This value of the FFT screening mass for a meson is given by [17]

$$a\mu_{FFT} = 2\sinh^{-1}\sqrt{(am)^2 + \sin^2(\pi/N_t)}. \qquad (1.29)$$

For a nucleon, it is 3/2 of the above value. We computed quantities in FFT by numerical inversion of the fermion matrix on a trivial gauge configuration (all links being the unit matrix). These quark propagators were then subjected to exactly the same analysis as
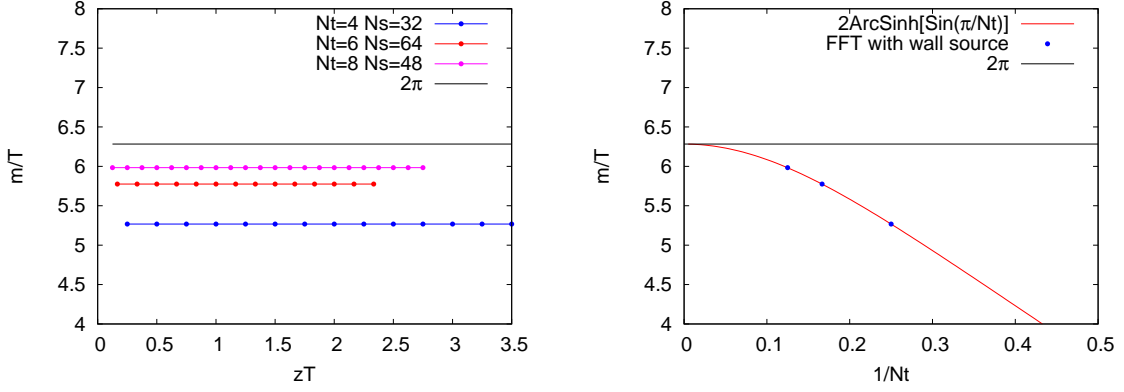
Figure 1.4: Wall source used on free field theory configurations show no finite volume effects (left) and show controlled finite lattice spacing effects (right).

in the interacting theory. Doing so, the effective mass of PS at z, obtained by fitting eq. (1.19) over the four consecutive z-slices, is shown as a function of z and N_t in the left panel of Figure 1.4. Finite volume effects are removed in the projection to the lowest Matsubara frequency. In the right panel, one can see the expected FFT behaviour in all the meson channels.

1.3.3 Screening Correlators and Restoration of Symmetries

Restoration of the spontaneously broken chiral symmetry, $\mathrm{SU}_V(2) \to \mathrm{SU}_L(2) \otimes \mathrm{SU}_R(2)$, implies a degeneracy between the vector and axial vector correlators (with both of them being isovectors). An approximate restoration of $U_A(1)$ will lead to a degeneracy between the scalar and pseudoscalar correlators (again both of them are isovectors). On a lattice, the continuum symmetries are broken and one has to address this symmetry restoration in terms of the symmetries of the transfer matrix, $\mathbf{T}$, for staggered fermions [48].

At finite temperature, $\mathbf{T}$ involves translation across z-slices. The symmetry of $\mathbf{T}$ is the rest frame group, $\underline{RF}$, which is obtained by the breaking of cylindrical symmetry of the z-slice due to lattice discretization [5]. However, the different correlators, $C_\gamma(z)$, which are of the form $\mathrm{Tr}\left[\mathbf{T}^{N_s-z}O_\gamma(z)\mathbf{T}^z O_\gamma(0)\right]$ belong to the different irreps of the point group of the z-slice, which is a subgroup of $\underline{RF}$. The irrep is decided by the symmetries of O_γ.

---

[5] The actual symmetry being broken is $C \otimes Z_2(I) \otimes U_B(1)$, where C is the cylindrical symmetry and $Z_2(I)$ is the inversion

At finite temperature, the point group is the discrete group D_4^h. This group has 16 irreps in six conjugacy classes [49]. The local mesons we study in this chapter — PS, S, V and AV, they all belong to the same one dimensional irrep A_1^+.

In FFT, the point group symmetry is the symmetry of **T**, and all the four correlators are degenerate. However, in an interacting theory, this may not be true. Since the A_1^+ to which PS and S belong to, descend from the same irrep of $\underline{RF}$, they have to be degenerate (provided the spontaneously broken symmetries are restored). Similarly, V and AV have to be degenerate. We characterize such pairwise degeneracy using the negative parity projections

$$C^{-V} = C^V - (-1)^z C^{AV} \quad \text{and} \quad C^{-S} = C^S - (-1)^z C^{PS}, \tag{1.30}$$

which vanish when symmetries are restored. In the same spirit, the positive projections C^{+V} and C^{+S} are obtained by adding the two correlators in the right hand sides of the above expressions, instead of finding the difference. These remove the staggered oscillations and project onto a parity partner.

One interprets any deviation between the two pairs of A_1^+ as due to the presence of interactions. This interpretation using the earlier studies provided a confusing picture. The V/AV correlators were found to be close to FFT by $2T_c$ indicating weakly interacting quarks, in which case the splitting between V/AV and S/PS correlators should be very small. However, the S/PS correlators were found to deviate from FFT by more than 20% [20] at these temperatures. This could be true if the symmetries of the deconfined phase were the same as in the confined phase, and the V/AV correlators do not differ from the zero temperature ones. In this thesis, we study this problem after improving the valence quarks.

1.4   A Problem with Staggered Screening Masses

Due to asymptotic freedom, one would expect that the quarks are weakly interacting at temperatures higher than the cross-over temperature T_c. Due to the presence of an additional mass scale temperature T, the infra-red behaviour of a naive perturbation theory around the $T = 0$ vacuum, at high temperatures is different from the one at $T = 0$. Dimensional reduction (DR) [50] and Hard thermal loop (HTL) [51] are better techniques of doing such weak-coupling expansions.
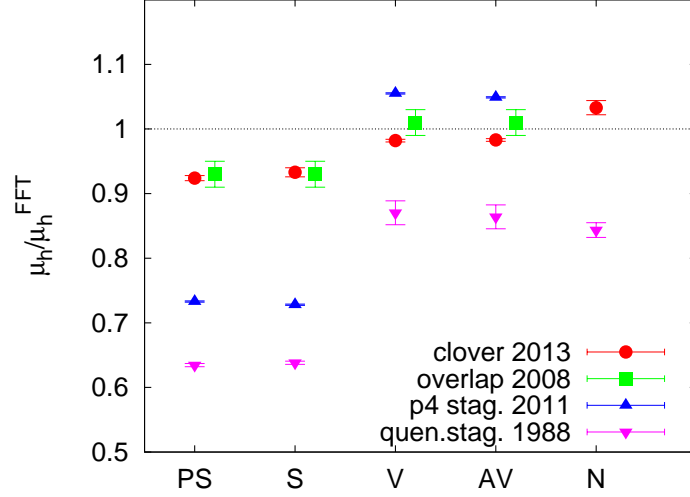
Figure 1.5: Comparison of screening masses with different quark actions at $1.5T_c$ (Clover 2013 [54], overlap 2008 [55], p4 stag [19] and quen. stag. 1988 [56]). Note that the staggered results do not agree with results from other quark actions. The disagreement is large in the case of PS/S.

There are three different scales in the QCD plasma: $g^2T \ll gT \ll T$. Dimensional reduction is an effective theory obtained by integrating out degrees of freedom from the hard scale T down to soft scale g^2T. On the other hand, HTL improves the perturbation theory by instead expanding around a vacuum of non-interacting dressed quarks and gluons. Though the results from these weak-coupling calculations have to agree with those from lattice, it is a priori not known at what temperatures they begin to agree. However, the fermionic part of the pressure, as well as its derivatives with respect to chemical potentials, the quark number susceptibilities (QNS), seem to admit reasonably accurate weak-coupling descriptions at temperatures of $2T_c$ or above [50, 52, 53].

However, even among static fermionic quantities, screening masses (the inverses of screening lengths) present a confused picture. In the deconfined phase, both HTL and DR calculations [11, 12] predict that the screening masses approach the free field theory (FFT) value, μ_{FFT}, as

$$\mu = \mu_{\text{FFT}} + \alpha_S\Delta \quad \text{with} \quad \Delta > 0, \tag{1.31}$$

where α_S is the strong coupling constant at a momentum scale of $2\pi T$. Most computations were performed with staggered quarks, and these seemed to indicate that there are

strong deviations from the above weak coupling prediction [10, 17–20] especially in the pseudoscalar/scalar channel. On the other hand, computations with Wilson quarks give results which are closer to free field theory [13], although they deviate in detail from predictions of weak coupling theory [11, 12]. Since the same pattern is visible in the quenched theory [54] (refer Figure 1.5), we can attribute the major part of the discrepancy to valence quark artifacts.

In this thesis, we examine this question systematically using staggered sea quarks and gauge-link smeared staggered valence quarks. Indeed, we see that smeared valence quarks provide a significant improvement. Using these we find that a weak coupling expansion does work quantitatively for the description of fermionic screening masses at finite temperature. In addition, our results may constrain models of thermal effects on hadrons below and close to the QCD cross over.

A significant technical component of this work is the exploration of the cause of improvement in lattice measurements when smeared gauge fields are introduced into the staggered quark propagators [6–9]. Smeared operators have been explored extensively in the literature earlier [14–16]. Here we explore optimization of smearing parameters by direct observation of the effects on UV and IR modes separately.

Chapter 2

Simulations and Setting of Scale

2.1   Set N, O and P

In this thesis, the thermal ensembles consist of $N_t \times N_s^3$ lattices with 2 flavours of dynamical staggered sea quarks, with anti-periodic boundary condition in the temporal direction for quarks. We used three different ensembles for our studies at finite temperature: set N, O and P. The set N consists of lattices with $N_t = 4$ and bare quark mass of $am = 0.015$. This set was newly generated, and we discuss its scale setting in the rest of this chapter. The pion mass for this ensemble (found using the mass of rho meson) is about 190 MeV. The set O [45] also has $N_t = 4$, but a heavier bare quark mass $am = 0.025$. Both the sets O and P [57] have the same pion mass of about 240 MeV, but the set P has a finer lattice spacing with $N_t = 6$. The bare quark mass on this lattice is $am = 0.0125$. The spatial extent in set O and P were both $N_s = 24$ at all temperatures. In each of the ensembles, we used about 50 independent configurations at all β for the measurement of correlators.

For the configuration generation for set N, we used the standard staggered fermion action, and Wilson gauge action for the simulation using R-algorithm. We tuned the parameters of the algorithm, the molecular dynamics step size Δt and the number of steps in a trajectory N_{MD}, by finding the largest Δ whose plaquette values were consistent $\Delta t \to 0$ limit. We refer the reader to Appendix A for details on this tuning. We merely state here that the runs were made with an MD step size $\Delta t = 0.01$. The number of MD time steps in the trajectory was scaled with the linear dimension of the lattice: $N_{\mathrm{MD}} = 100(N_s/8)$ on an $N_t \times N_s^3$ lattice. The simulations were started from a configuration consisting of all unit link matrices. During thermalization, we used larger values of Δt

β	$T = 0$, 16^4			4×16^3			4×24^3		
	am	P	T/T_c	am	τ	N	am	τ	N
5.25	0.0165	0.4790 (3)	0.92 (1)	0.0165	19	65			
5.26	0.0160	0.4827 (4)	0.96 (1)	0.0160	31	51			
5.27	0.0153	0.4860 (5)	0.98 (1)	0.015	72	48			
5.2746	0.015	0.4873 (4)	1.00						
5.275	0.015	0.4873 (5)	1.01 (1)	0.015	328	76			
5.28	0.0146	0.4887 (6)	1.02 (1)	0.015	65	62			
5.29			1.06 (1)	0.015	21	49			
5.3	0.0138	0.4957 (7)	1.10 (1)	0.0138	8	59			
5.335			1.20 (1)	0.0125	7	75			
5.34	0.0115	0.5100 (2)	1.29 (3)				0.0115	6	50
5.38	0.01	0.5243 (1)	1.51 (5)				0.01	6	57
5.48	0.0075	0.5480 (2)	2.03 (9)				0.0075	3	79

Table 2.1: The number of independent configurations, N, obtained with the coupling, β, the bare quark mass, am, and the auto-correlation time, τ, for that simulation. Also given are the plaquette value, P, measured at $T = 0$, and the temperature, T/T_c, inferred from it.

(0.04 at the beginning), and switched gradually to $\Delta t = 0.01$. In this way, we found the configurations to thermalize within 300 trajectories. We discarded the first 300 trajectories for thermalization at all temperatures. The auto-correlation time remained stable when this thermalization cut was further increased to 500 trajectories.

We generated configurations on four sets of spatial volumes: $N_s = 8, 12, 16$ and 24. The lattices with $N_s = 8$ and 12 were used only for bracketing the location of the cross-over coupling β_c. The details on finding β_c are given in the next section. The bare quark masses in $N_s = 16$ and 24 simulations, were tuned such that m/T_c was kept fixed at 0.06 at all temperatures. The number of auto-correlation time separated configurations at each β in these lattices were about 50. The temperature scale, T/T_c, was set using the $T = 0$ plaquette values which were determined on 16^4 lattice. The physical scale was set by determining the light hadron masses at $T = 0$. These are discussed in the subsequent sections in this appendix. Details of configurations that we generated on $N_s = 16$ and 24 lattices are tabulated in Table 2.1.

2.2 Determination of Cross-over Coupling β_c through Reweighting

This section deals with the determination of cross over coupling β_c using multi-histogram reweighting [58]. Reweighting is a method used to interpolate or extrapolate observables based on Monte-Carlo measurements of the observables at a few simulation points. This method is especially useful near the critical point as an actual simulation near it would be very expensive due to critical slowing down. In the next subsection, we briefly outline this method. Then, we present the details on our determination of the cross over coupling.

2.2.1 Multi-histogram Reweighting

Let the partition function for a system be

$$Z(\beta) = \sum_S g(S) \exp\left(-\beta S\right), \tag{2.1}$$

with β being the coupling, and $g(S)$ is the density of states with the action, S. Taking the simple example of single histogram reweighting, let us assume that the system is simulated at a coupling β_1, with the total number of independent configurations being n_1. During the simulation, the histogram $\{N_1(S)\}$ of S from the n_1 configurations are also stored. For a Monte-Carlo simulation, the histogram is distributed according to eq. (2.1). From this, one gets an estimator of $g(S)$

$$\overline{g}(S) = Z(\beta_1)\frac{N_1(S)}{n_1} \exp\left(\beta_1 S\right). \tag{2.2}$$

Using the above estimator for the density of states, the expectation value of an observable O can be extrapolated to another coupling β as

$$\langle O \rangle_\beta = \frac{\sum_S O(S)\overline{g}(S) \exp\left(-\beta S\right)}{\sum_S \overline{g}(S) \exp\left(-\beta S\right)} = \frac{\sum_S O(S)N_1(S) \exp\left(\delta\beta_1 S\right)}{\sum_S N_1(S) \exp\left(\delta\beta_1 S\right)}, \tag{2.3}$$

where $\delta\beta_1 = \beta_1 - \beta$. Instead of a histogram, one can store the list of S obtained during the simulation. In which case, $N_1(S) = 1$ for each of the S in the list.

Extending to a multi-histogram reweighting, one has R different simulation points at

$\beta_1, \dots, \beta_i \dots, \beta_R$. In each of the simulation points, one has the histogram of S: $\{N^{(i)}\}$. Using the histogram from β_i, the density of states can be estimated from eq. (2.2) as $g^{(i)}(S)$. One can combine the R such estimates to get a new estimator

$$\overline{g}(S) = \sum_i^R p_i g^{(i)}(S) \quad \text{with} \quad \sum_i p_i = 1. \tag{2.4}$$

The values of p_i are chosen to minimize the error in $\overline{g}(S)$. For the calculation beyond this point, we refer the reader to [58]. For this method to work, there must be sufficient overlap between the different histograms in the region of interpolation (or extrapolation) so that all the $g^{(i)}(S)$ are not equal to zero. Finally, we quote the final working formula when $R = 2$ (two histogram method):

$$\langle O \rangle_\beta = \sum_{r=1}^2 \frac{\sum_{i=1}^{n_r} O_i^{(r)} P_i^{(r)}}{\sum_{i=1}^{n_r} P_i^{(r)}} \quad \text{with} \quad P_i^{(r)} \equiv \frac{\exp(-\beta S_i^{(r)})}{n_1 \zeta \exp(-\beta_1 S_i^{(r)}) + n_2 \exp(-\beta_2 S_i^{(r)})}, \tag{2.5}$$

where $\{S_i^{(r)}\}$ is a list of n_r independent values of the action from the simulation point at β_r. $\{O^{(r)}\}$ is the corresponding list of measurements of the observable. The constant $\zeta = Z(\beta_1)/Z(\beta_2)$ is determined by numerically solving the above equation for the condition $\langle 1 \rangle_{\beta_1} = 1$.

2.2.2 β_c from Susceptibilities

We determined the cross-over coupling, β_c, by positions of the peaks of different suscepti-bilities. The width of the cross-over, $\Delta\beta_c$, is defined to be the full width at half maximum (FWHM) of the same susceptibilities. We measured the unrenormalized Wilson line sus-ceptibility, χ_L, the bare chiral susceptibility, χ_M, and the fourth order QNS, χ_{22} and χ_{40}, at various values of β in the crossover region. We also measured a renormalized quantity related to the chiral susceptibility [59],

$$\frac{m_r^2 \chi_M^r}{T^4} = \frac{m^2}{T^4} \left(\chi_M(T) - \chi_M(0) \right). \tag{2.6}$$

m_r and χ_M^r are the renormalized quark mass and chiral susceptibilities respectively. We determined $\chi_M(0)$ on 16^4 lattice at the same values of β as the finite temperature ones
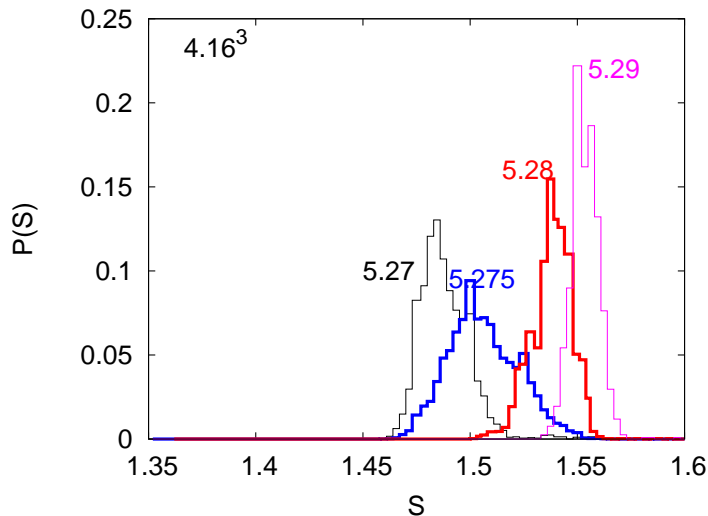
Figure 2.1: The probability distribution of the Wilson action S (which is the plaquette value). The color code is black:$\beta = 5.27$, blue: 5.275, red: 5.28 and magenta: 5.29. The histograms from $\beta = 5.275$ and 5.28 (shown in bold) were used for multi-histogram reweighting due to their long overlapping tails.

(refer Table 2.1).

To determine β_c accurately, we interpolated the data for susceptibilities using multihistogram reweighting [58] in the cross over region. In Figure 2.1, we show the histogram of the Wilson action, S, (which is the plaquette value) at various β on $N_s = 16$ lattice. The histograms of S are very different at the two extreme values of β. The change takes place over a very narrow range, where the histograms have long overlapping tails. We choose a pair of couplings in this range for multi-histogram reweighting; we choose $\beta = 5.275$ and 5.28 in the case shown. The results for χ_L and χ_M are shown in Figure 2.2. The data points are measurements at various simulation points. The 1-σ error band from multihistogram reweighting is also shown. The error band is obtained by bootstrap sampling of the histograms. From the reweighted curves for each of the bootstrap samples, we determined the peak values along with their statistical errors, and tested the hypothesis that no volume dependence is seen in the peak of each of the susceptibilities for $N_s \geq 12$. We find that the χ^2 values for this hypothesis to be $0.57, 1.16, 0.77$ and 1.07 for $\chi_M, \chi_L, \chi_{22}$ and χ_{40} respectively. This is consistent with the fact that there is a cross over. However, we do not pursue this direction any further, and take it as a well established fact.
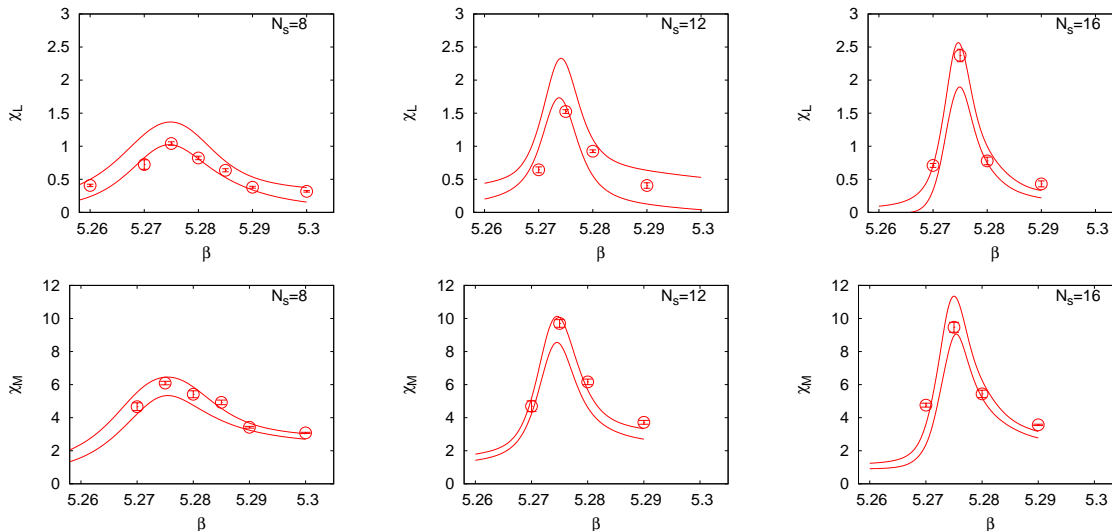
Figure 2.2: Dependence of the chiral susceptibility, χ_M, and the Wilson line susceptibility, χ_L, on coupling, β, and spatial extent, N_s. The variation with β for χ_M (top three panels) and χ_L (bottom three panels) are given for $N_s = 8$, 12 and 16 from left to right in that order. The cross-over coupling, β_c, is determined through the location of the peaks of the susceptibilities. The width of the cross-over, $\Delta\beta_c$ is determined from the full-width at half the maximum.

We determined the means and errors in the position of the peak of reweighted curves for each susceptibility and its FWHM, so obtaining β_c and $\Delta\beta_c$ [60]. We found β_c and $\Delta\beta_c$ for each of the susceptibilities on the three different lattice volumes. The results are shown in Figure 2.3. Since we found very little volume dependence in β_c, we made a fit to a constant, independent of volume. The values of β_c so determined are displayed in Table 2.2. In Figure 2.3 we also show the volume dependence of $\Delta\beta_c$. This decreases with the volume, and gives some indication of saturating, within errors, close to our largest lattice. So we take $\Delta\beta_c$ obtained on $N_s = 16$, as our best estimate. These estimates are also listed in Table 2.2. We find that the variation in β_c with different susceptibilities occur well within the width of the cross over measured from each indicator separately. In fact, the four estimates of β_c are consistent with each other within 68% confidence limits. Combining all four measurements, we quote $\beta_c = 5.2744(7)$ and $\Delta\beta_c \approx 0.006$.

In Figure 2.4, we show the temperature dependence for the renormalized quantity $m_r^2 \chi_M^r / T^4$. The figure shows that with this cutoff, the deconfining and chiral cross overs
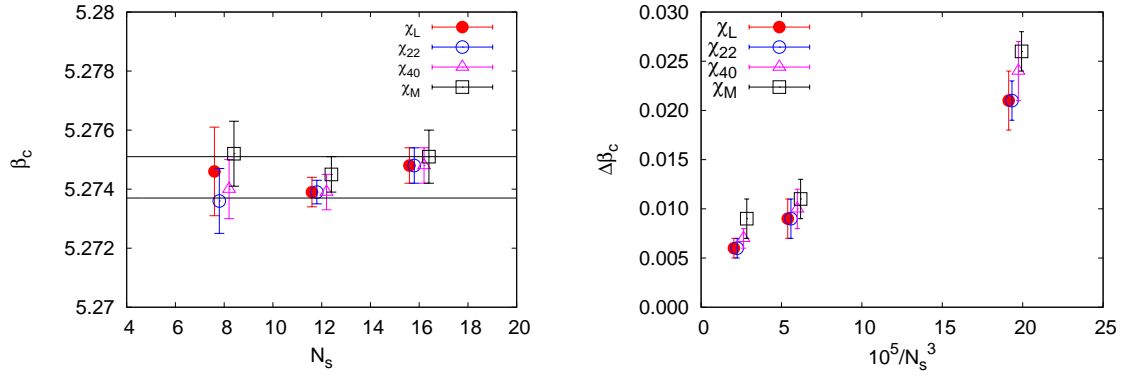
Figure 2.3: The spatial size dependence of β_c (left) and $\Delta\beta_c$ (right). The lines enclose 68% confidence limits on β_c, obtained by fitting a single constant to all the estimates.

	β_c	$\Delta\beta_c$
χ_M	5.2747(6)	0.009(2)
χ_L	5.2743(5)	0.006(1)
χ_{22}	5.2741(5)	0.006(1)
χ_{40}	5.2743(6)	0.007(1)

Table 2.2: β_c and $\Delta\beta_c$ as determined from different susceptibilities. $\Delta\beta_c$ is much larger than the statistical error in β_c.
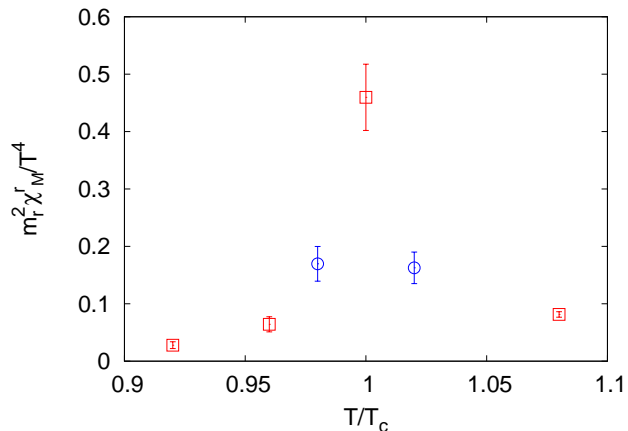
Figure 2.4: Dependence of $m_r^2 \chi_M^r / T^4$ on T/T_c. The data points marked by boxes are measurements made on line of constant m/T_c, whereas those marked by circles are obtained with constant am.

in QCD coincide; $m_r^2 \chi_M^r / T^4$ peaks between 0.98 and $1.02 T_c$.

2.3   Setting of Scale using Hadron Masses

All the measurements made on the lattice are in units of lattice spacing. In order to express the quantities in physical units, we determined the pion, rho and nucleon masses with $T = 0$ computations. We determined the hadron masses at β_c for set N ($\beta_c = 5.2746$) and set O ($\beta_c = 5.2875$) on 16^4 lattices. In addition, we also determined the masses on a 24^4 lattice with a fine lattice spacing at $\beta = 5.53$ with a bare quark mass of $am = 0.0125$. An earlier hadron mass measurements for set O was done on a $8^3 \times 24$ lattice [61]. Here we redo the analysis using a larger lattice and using extended quark sources.

For set N, the quark mass being comparatively lighter, it presented the problem of noisy hadron correlators. We were able to tackle the this problem by using extended quark sources — we used wall [31] and Wuppertal [32] quark sources, while using point sink (refer Section 1.2.4).

By trial and error, we found Wuppertal smearing (refer eq. (1.18)) with $N = 2$ and $\kappa = 0.11$ to work better than with other values. The RMS radius of the quark source with this choice of parameters is $\sqrt{3}\sigma \approx 0.8$ fm, which is about the charge radius of the proton.

am	β	am_ρ	m_π/m_ρ	m_N/m_ρ
0.015	5.2746	1.31(8)	0.25(2)	1.34(9)
0.025	5.2875	1.3(1)	0.32(3)	1.2(2)
0.0125	5.53	0.64(5)	0.50(4)	1.8(2)

Table 2.3: Hadron mass measurements for set N at β_c (top row), set O at β_c (middle row), and a fine lattice with half the lattice spacing as set N and O.

Perhaps, this explains why this choice works. The noise in rho and nucleon correlators were further reduced when 10-level 3d-APE smeared links (with smearing parameter $\epsilon = 0.6$) is used in the Laplacian.

With the source at $t = 0$, the effective mass for the pion at a time-slice t is determined by fitting the correlator using a single mass fit (eq. (1.19) with no parity partner) over two successive time-slices, t and $t + 1$. In order to account for the staggered oscillations in the rho and nucleon correlators, the effective masses at t are determined by fitting the correlator using eq. (1.19) and eq. (1.20) over the four consecutive time-slices respectively. The results for the effective masses of the hadrons are shown in Figure 2.5. The panels on the left are for the wall source, and the ones on the right are for the Wuppertal source. With wall source, we still could not determine the nucleon mass. With Wuppertal smearing, we were able to determine all the masses.

We tabulate the masses of hadrons for all the three zero temperature ensembles in Table 2.3. By using $m_\rho = 770$ MeV, the lattice spacing at β_c for set N is about 0.32 fm. The pion mass for set N configurations is about 190 MeV, while the nucleon is about 1000 MeV. The cross over temperature from both the confinement-deconfinement and deconfinement order parameters is about 150 MeV.

2.4 The Temperature Scale

We determined the temperature scale by determining the plaquette values, P, at $T = 0$ on 16^4 lattices, for the same set of values of β as at finite T [62]. Using the plaquette values, we used three different renormalization schemes (namely E-scheme [63], V-scheme [64] and $\overline{\text{MS}}$-scheme) in order to determine the renormalized coupling α at the scale of the lattice spacing a. With the assumption that a is small enough to use the 2-loop QCD

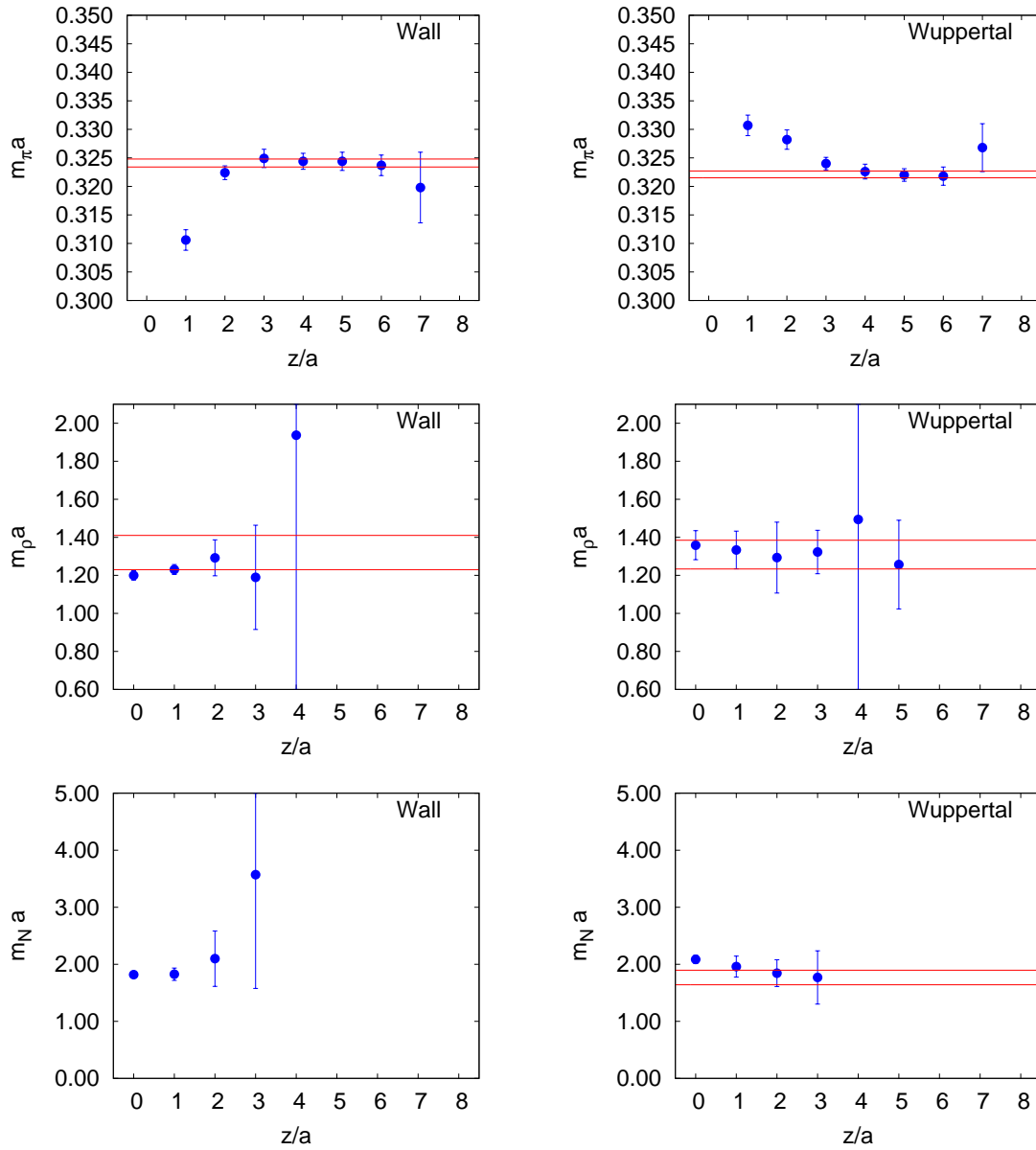Figure 2.5: The effective masses of different hadrons with wall source (left panels) and Wuppertal source (right panels). The red bands are the 1-σ bands of best fit values of the hadron mass. The top panels are for the pion, the middle ones for the vector meson, and the bottom ones for the nucleon.

β	ma	E	V	$\overline{MS}$	m/Tc
		T/T_c	T/T_c	T/T_c	
5.25	0.0165	0.9276(28)	0.9147(34)	0.9187(32)	0.0606
5.255	0.0162	0.9450(20)	0.9353(23)	0.9383(22)	0.0608
5.26	0.0160	0.9628(18)	0.9563(21)	0.9584(20)	0.0613
5.27	0.0153	0.9905(20)	0.9889(23)	0.9894(22)	0.0606
5.2746	0.0150	1.0000(18)	1.0000(21)	1.0000(20)	0.0600
5.275	0.0150	1.0096(30)	1.0113(36)	1.0107(34)	0.0606
5.28	0.0146	1.0194(29)	1.0227(34)	1.0216(33)	0.0597
5.3	0.0138	1.0915(26)	1.1067(30)	1.1018(29)	0.0608
5.3406	0.0115	1.2590(24)	1.3007(28)	1.2866(27)	0.0592
5.367	0.0104	1.3818(56)	1.4422(62)	1.4213(60)	0.0591
5.381	0.0100	1.4699(17)	1.5435(19)	1.5176(18)	0.0607
5.42	0.0088	1.6229(26)	1.7194(29)	1.6848(28)	0.0593
5.483	0.0075	1.9432(28)	2.0870(30)	2.0337(29)	0.0610
5.56	0.0063	2.2739(29)	2.4667(31)	2.3935(31)	0.0603

Table 2.4: Temperature scale set using three different schemes (E, V and $\overline{MS}$). β_c is taken to be 5.2746. ma is the bare mass given in lattice units for a given β. The error due to scheme dependence of T/T_c is about 0.01 for all β which is greater than the statistical error. $m/T_c \approx 0.06$ for all β.

β-function, the lattice spacing is related to α through

$$a\Lambda = kR(1/4\pi\beta_0\alpha) \quad \text{where} \quad R^2(x) = \exp(-x)x^{(\beta_1/\beta_0^2)}, \tag{2.7}$$

where Λ is the QCD scale parameter determined in a particular scheme. k is a renormalization scheme dependent constant. β_0 and β_1 are the scheme independent first and second coefficients in the β-function. From the plaquette values at β and β_c, we found the temperature scale $T/T_c = a_c/a$. We determined both T/T_c and ma self consistently such that $m/T_c \sim 0.06$. The temperature scale set by the above procedure is given in Table 2.4. As it can be seen, the scheme dependence is more than that of statistical error at this lattice spacing. Therefore, we quote the error from scheme dependence for T/T_c in Table 2.1.

Chapter 3

Studies on Gauge-link Smearing

3.1 Introduction

Gauge-link smearing is based on the wisdom that the average of random variates fluctuate less than the variates themselves. The gauge-link smeared links are constructed by replacing the original unsmeared link (henceforth called thin-links) connecting two points, with a gauge-covariant average of different paths connecting the same two points. The choice one makes by choosing a smearing scheme is the set of paths that are being included, and the weightage given to each of them.

A qualitative reasoning as to why gauge-link smearing should be useful to ameliorate taste breaking, is useful at this point. The different tastes of the quark field, $\psi^t(x)$, are different combinations of the staggered fields, χ, on a hypercube. Thus, in the presence of gauge fields, the different tastes experience different gauge-links within the hypercube. Therefore, a rapidly fluctuating gauge field is expected to increase taste breaking. Given the motivation of gauge-link smearing as a tool to suppress the UV fluctuations, this chapter is therefore mainly on the aspects of smearing in the context of staggered quarks.

The chapter is organized as follows. In Section 3.3, we demonstrate that gauge-link smearing suppresses UV more than IR in both the quark and glue sectors. Then, we understand the effect of smearing on the mean value of plaquette using tree-level weak-coupling expansion in Section 3.4. After that, we present our results on the factorization of pion-taste splitting into a smearing dependent factor and a lattice spacing dependent factor in Section 3.5. This explains how smearing helps to obtain results closer to their continuum values, but at finite lattice spacings. We show that by improving taste symmetry through

gauge-link smearing at zero temperature, one obtains a quadratic taste improvement in the deconfined phase.

3.2   Constructions of Smearing

In the following subsections, we briefly outline the constructions of four gauge-link smearing schemes — APE [6], Stout [7], HYP [8], and HEX [9].

3.2.1   APE

APE smearing is the oldest, and also the simplest construction of smeared links[6]. The gauge-covariant average is taken only over the paths which form the staple around the link. The exact construction of APE smeared link, $V_{x,\mu}$, is

$$V_{x,\mu} = \mathrm{Pr}\left[(1-\epsilon)U_{x,\mu} + \frac{\epsilon}{6}C_{x,\mu}\right], \tag{3.1}$$

where the staple, $C_{x,\mu}$, is given by

$$C_{x,\mu} = \sum_{\pm\nu\neq\mu}^{4} U_{x,\nu}U_{x+\hat{\nu},\mu}U_{x+\hat{\mu},\nu}^{\dagger}. \tag{3.2}$$

The real coefficient ϵ is a tunable parameter, and it determines the weightage given to the neighbouring staples over the original thin-link. Henceforth, ϵ is called the smearing parameter in this thesis. Tuning this coefficient to its optimal value is one of the goals in this study. As the sum of SU(3) matrices do not in general lie in SU(3), the resulting averaged link is projected to SU(3) as indicated by $\mathrm{Pr}[\ldots]$. The choice for the projection is not unique; we use the method of polar decomposition [65] of arbitrary matrices. A pictorial representation of the construction of APE is shown in Figure 3.1.

3.2.2   Stout

Stout smearing was proposed in [7] as a method of smearing which avoids the problem of projection to SU(3). For this, one constructs a traceless anti-hermitean matrix out of the products of neighbouring links, which form the plaquettes hinged on the original thin-link,
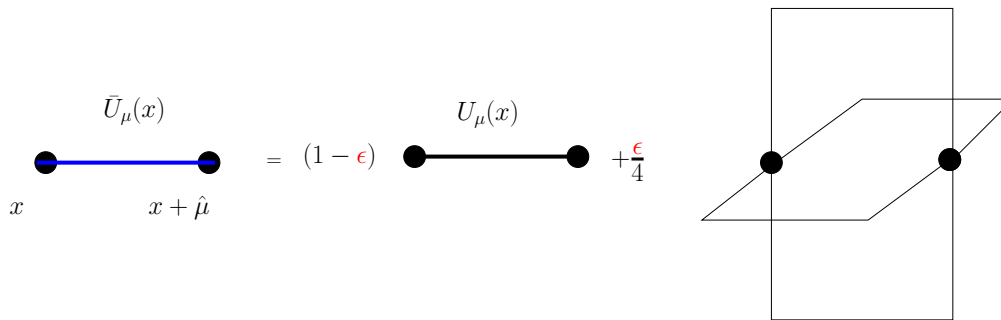
Figure 3.1: Construction of APE smeared link in 3d. The APE smeared link (blue) is constructed as a weighted sum of the original thin-link and the neighbouring paths (staples in this case) connecting the same two points. The resulting link is projected to SU(3).

and then exponentiate it to get a matrix which lies in SU(3). The Stout smeared link is obtained by multiplying this with the thin-link. The construction is given by

$$V_{x,\mu} = \exp\left(\epsilon \left[C_{x,\mu}U_{x,\mu}^\dagger\right]_{\mathrm{TA}}\right) U_{x,\mu}, \tag{3.3}$$

where $[\ldots]_{\mathrm{TA}}$ is the traceless anti-hermitean part of its argument. Again, a tunable smearing parameter, ϵ, controls the weightage given to the neighbouring links.

3.2.3   Hypercubic schemes

It is possible to iterate APE or stout smearing n_{lev} successive times. But, it has the disadvantage of making the construction of smeared links non-local; an n_{lev}-APE smeared link involves the thin-links that are n_{lev} lattice spacings apart. Hypercubic smearing schemes are constructed to overcome this problem of locality. HYP [8] is the hypercubic version for APE, and HEX [9]is based in Stout. A single level of HEX has three nested sub-levels constructed such that the smeared links at the n-th sub-level, $V^{(n)}$, are built only out of the thin-links that are within a hypercube. The final HEX smeared links, $V_\mu^{(3)}$

obtained in the third sub-level, are given by

Sub-level 1: $V^{(1)}_{x,\mu;\nu\rho} = \exp\left(\frac{\epsilon_1}{2}\left[C^{(1)}_{x,\mu;\nu\rho}U^\dagger_{x,\mu}\right]_{\text{TA}}\right)U_{x,\mu},$ $C^{(1)}_{x,\mu;\nu\rho} = \sum_{\pm\sigma\neq\mu\nu\rho}\left[U_{x,\sigma}U_{x+\sigma,\mu}U^\dagger_{x+\mu,\sigma}\right]$

Sub-level 2: $V^{(2)}_{x,\mu;\nu} = \exp\left(\frac{\epsilon_2}{4}\left[C^{(2)}_{x,\mu;\nu}U^\dagger_{x,\mu}\right]_{\text{TA}}\right)U_{x,\mu},$ $C^{(2)}_{x,\mu;\nu} = \sum_{\pm\sigma\neq\mu\nu}\left[V^{(1)}_{x,\sigma;\mu\nu}V^{(1)}_{x+\sigma,\mu;\sigma\nu}V^{(1)\dagger}_{x+\mu,\sigma;\mu\nu}\right]$

Sub-level 3: $V^{(3)}_{x,\mu} = \exp\left(\frac{\epsilon_3}{6}\left[C^{(3)}_{x,\mu}U^\dagger_{x,\mu}\right]_{\text{TA}}\right)U_{x,\mu},$ $C^{(3)}_{x,\mu} = \sum_{\pm\sigma\neq\mu}\left[V^{(2)}_{x,\sigma;\mu}V^{(2)}_{x+\sigma,\mu;\sigma}V^{(2)\dagger}_{x+\mu,\sigma;\mu}\right],$

$$(3.4)$$

where $C^{(n)}$ are staples constructed out of the smeared links in the $(n-1)$-th sub-level. In this thesis, we take $\epsilon_1 = \epsilon_2 = \epsilon_3$ for the sake of simplicity. HYP smeared links are similarly constructed, based on APE, as

Sub-level 1: $V^{(1)}_{x,\mu;\nu\rho} = \Pr\left[(1-\epsilon_1)U_{x,\mu} + \frac{\epsilon_1}{2}C^{(1)}_{x,\mu;\nu\rho}\right]$

Sub-level 2: $V^{(2)}_{x,\mu;\nu} = \Pr\left[(1-\epsilon_2)U_{x,\mu} + \frac{\epsilon_2}{4}C^{(2)}_{x,\mu;\nu}\right]$ (3.5)

Sub-level 3: $V^{(3)}_{x,\mu} = \Pr\left[(1-\epsilon_3)U_{x,\mu} + \frac{\epsilon_3}{6}C^{(3)}_{x,\mu}\right].$

The plethora of directional indices seen in the above definitions, means a memory requirement which is twelve times more than that for thin-links, merely used as work-space. We developed a memory optimized implementation of HEX, which reduces the memory requirement for work-space by more than 50%. We discuss this in Appendix B.

3.3   Suppression of UV

The effectiveness of smearing in suppressing the UV has been studied earlier [8] indirectly, by constructing the histogram of plaquettes, and noting the effect of smearing on atypically small plaquette values. In this section, we present a direct method of studying how smearing affects UV and IR modes in both the gauge and quark sectors. Through this, we learn how the suppression in UV and IR are different, and also obtain different estimates of the optimum values of ϵ. For this part of the study, we use one level of smearing for all the schemes.

3.3.1 Gluon Sector

In order to study the rapid space-time variations of gauge-field, configuration by configuration, we need to suitably choose a quantity which is local, and gauge-invariant. The simplest such pure-gauge observable is the plaquette; the definition of plaquette we use in this study is

$$P(x) \equiv \sum_{\mu=1}^{4} \text{ReTr} \left(C_{x,\mu} U_{x,\mu}^{\dagger} \right). \tag{3.6}$$

We study the effects of gauge link smearing on the high frequency modes of the gauge field by constructing the power spectrum, $E(k)$, of plaquettes:

$$P(k) = \sum_{x} \exp\left(ik \cdot x\right) P(x) \qquad \text{and} \qquad E(k) = |P(k)|^2. \tag{3.7}$$

The mode numbers $k_\mu = \pi(2\ell_\mu + \zeta_\mu)/N_\mu$, N_μ is the size of the lattice in the direction μ, the integers $0 \le \ell_\mu < N_\mu$, and $\zeta_\mu = 0$ for periodic boundary conditions and 1 for anti-periodic. Periodic or anti-periodic boundary conditions imply that the independent modes are those with ℓ_μ inside the Brillouin hypercube whose body diagonal, BD, joins the corners (0,0,0,0) and $(N_x/2, N_y/2, N_z/2, N_t/2)$. We use this power spectrum to find how smearing affects the UV and IR modes. As shown in Figure 3.2, we separate the IR and UV using the hyperplanes perpendicular to BD. All modes within the Brillouin zone closer to the origin than a hyperplane σ_{IR} are called IR modes; conversely all modes within the Brillouin zone closer to the far corner than the plane σ_{UV} are called UV modes. Everything else is a generic mode— neither IR, nor UV. Quantitatively, if $\hat{n}$ is a unit vector along BD, then the mode $\mathbf{k} = (k_1, k_2, k_3, k_4)$ is classified as UV or IR based on whether

$$\mathbf{k} \cdot \hat{n} < 2\pi f \quad \text{or} \quad \mathbf{k} \cdot \hat{n} > 2\pi(1-f) \tag{3.8}$$

respectively. The fraction, f, of the total length of BD where σ_{IR} intercepts BD, is arbitrary and less than 1. We check that our results do not depend on the choice of f.

We monitor how the total power in IR and UV regions behave with smearing. We define the suppression of power in the IR and UV as a function of ϵ

$$Q_{UV} = \frac{E_{UV}(\epsilon)}{E_{UV}(0)}, \qquad \text{and} \qquad Q_{IR} = \frac{E_{IR}(\epsilon)}{E_{IR}(0)}, \tag{3.9}$$
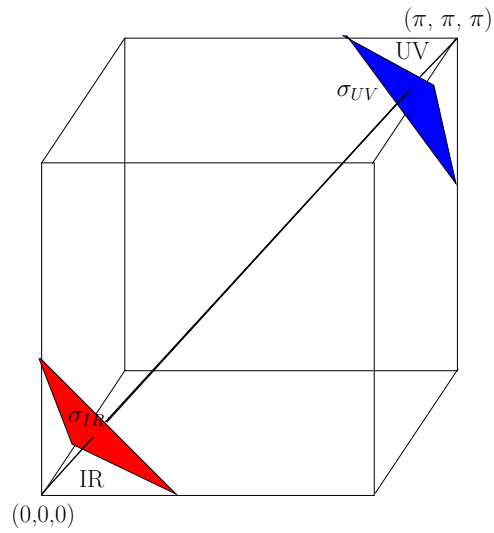
Figure 3.2: Defining UV and IR. The cube represents a three dimensional Brillouin zone for illustration. The body diagonal connects the origin to the opposite corner of the cube. The modes between the origin and the plane σ_{IR}, which is perpendicular to the body diagonal, are defined as IR modes. Similarly, the modes between σ_{UV} and the farthest corner are defined as UV. The rest of the modes are generic. The distances of the planes from the origin are arbitrary.

Figure 3.3: Suppression of power in UV and IR plotted as a function of smearing parameter, ϵ, and different smearing schemes. The top panel is on a coarse lattice at $\beta = 5.2875$, while the bottom panel is in a finer lattice with $\beta = 5.53$. UV is more suppressed than the IR at small values of ϵ. Optimal values of ϵ are the ones which suppresses the UV the most.
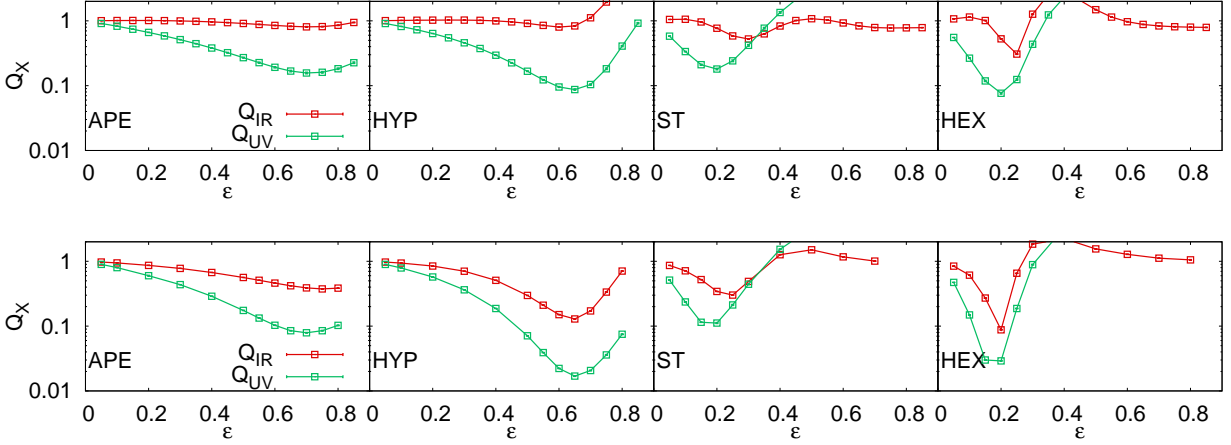
where $E_{UV}(\epsilon)$ is the power summed over all modes in the UV for a fixed value of ϵ, and $E_{IR}(\epsilon)$ is a similar quantity obtained by summing over all modes in the IR. If Q is less than 1, then smearing is successful is suppressing the modes.

We investigated Q numerically with thermalized configurations at $T = 0$ using $\beta = 5.2875$ and $\beta = 5.53$ (corresponding to lattice spacings of 0.34 and 0.17 fm as discussed in Section 2.3) on 16^4 and 24^4 lattices respectively. Periodic boundary conditions were used so that all $\zeta_\mu = 0$. We used fast Fourier transforms [66] to determine the power spectrum on 16^4 lattices, while using brute-force to determine the Fourier transform on 24^4 lattice. The variation of Q_X with ϵ is shown in the top two panels of Figure 3.3. First focusing on the top panel, one sees that the slope of the curve for Q_{UV} always starts off larger than that for Q_{IR}. Also, the slope of the latter seems to be close to zero. This shows that smearing can be used to modify the UV without modifying the IR. One can use this to seek an optimum value of ϵ, such that Q_{UV} is as small as possible. From the bottom panel, we find that there is a change in the overall suppression of power in the IR and UV, but the change in the optimum ϵ is not large even when the lattice spacing is halved. The optimum values of ϵ move down slightly. This movement is compatible with the intuition
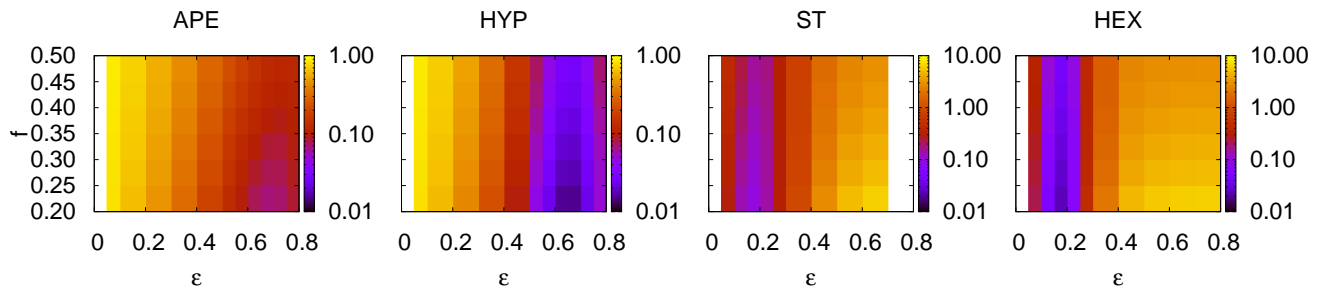
Figure 3.4: Q_{UV} as a function of ϵ and the distance, f, of the plane, σ_{UV}, from the farthest corner of the Brillouin zone. The minimum of Q_{UV} seems to not depend on the distance f.

that finer lattices require less improvement. One could argue that there are more UV modes on finer lattices, and therefore more smearing would be required. The fallacy lies in the fact that the increasing number of UV modes leads to divergences which are taken care of by renormalization. The contribution from the UV modes to the lattice corrections to renormalized quantities should reduce, since these lattice corrections are irrelevant, in the sense of renormalization group.

Since the definitions of IR and UV are arbitrary, one needs to check whether the results are sensitive to this definition. We place the planes σ_{IR} and σ_{UV} at a fraction f of the length of the diagonal (with $0 < f < 0.5$, so that no mode is simultaneously in the IR and UV) from the nearest corner, and varied f. The result for Q_{UV} is shown in Figure 3.4. The colour code is such that Q_{UV} decreases when we go from yellow to blue. We find that the optimum ϵ is insensitive to f. The results on the optimum values of ϵ for different smearing schemes are collected in Table 3.1.

3.3.2   Quark Sector

Having shown that, for a range of ϵ, UV is suppressed more than IR in the glue sector, we now study the corresponding behaviour in the quark sector. For this, we choose the maximum and minimum eigenvalues of $D^\dagger D$, λ_{max} and λ_{min} respectively, as proxies for UV and IR (refer eq. (1.12) for the definition of massive staggered Dirac operator D). This is

justified, given the dimension of the eigenvalues of D to be that of energy.

We determine the eigenvalues of $D^\dagger D$ using the Lanczos algorithm [67]. It is an iterative method for tridiagonalizing positive definite hermitian matrices:

$$T = Q^\dagger \left(D^\dagger D\right) Q, \tag{3.10}$$

where T is tridiagonal, and Q is unitary. The k-th step of the algorithm computes a tridiagonal matrix, T_k, which is the $k \times k$ sub-matrix of T. The extremal eigenvalues of T_k rapidly converges towards the extremal eigenvalues of $D^\dagger D$, as shown using Kaniel-Paige convergence theory[67]. Therefore, it is a suitable method for us to determine the extremal eigenvalues of $D^\dagger D$. We construct T_k and determine its extremal eigenvalues using the Lapack subroutine *dstevx*. The stopping criterion for the algorithm is that the extremal eigenvalues do not change by more than δ for 5 successive Lanczos iterations; we take $\delta = 10^{-8}$. With this value for δ, we find the extremal eigenvalues to converge within $k = 2000$ steps.

In Figure 3.5, we show the behaviour of the extremal eigenvalues as a function of ϵ for all the four smearing schemes. The top panel is for the coarser lattice with $\beta = 5.2875$, and the bottom panel is for the finer lattice having $\beta = 5.53$ (which has half the lattice spacing as that at $\beta = 5.2875$). We find that smearing reduces λ_{max} when small values of ϵ are used. The maximum reduction occurs at values of ϵ which are very close to that of the optimal values obtained in the gauge sector. Unlike in the gauge-sector, this effect remains intact when the lattice spacing is halved. Within our precision of determination of λ_{min}, which is $\delta = 10^{-8}$, we do not see any changes due to smearing. The values of optimal ϵ, as determined from the maximum reduction in λ_{max}, are also tabulated in Table 3.1.

Smearing also provides a computational advantage by reducing the effort to invert the Dirac operator — an operation which is ubiquitous in lattice QCD. It is required, for example, in the Hybrid Monte Carlo algorithms [68] and for constructing quark propagator. Since the typical size of the Dirac operator is $\mathcal{O}(10^6 \times 10^6)$, one typically uses iterative methods such as the conjugate gradient (CG) [67]. It converts the problem of finding the vector $x = \left(D^\dagger D\right)^{-1} b$ into a problem of finding the minimum of the parabola

$$y = \frac{1}{2} x^\dagger \left(D^\dagger D\right) x - x^\dagger b, \tag{3.11}$$
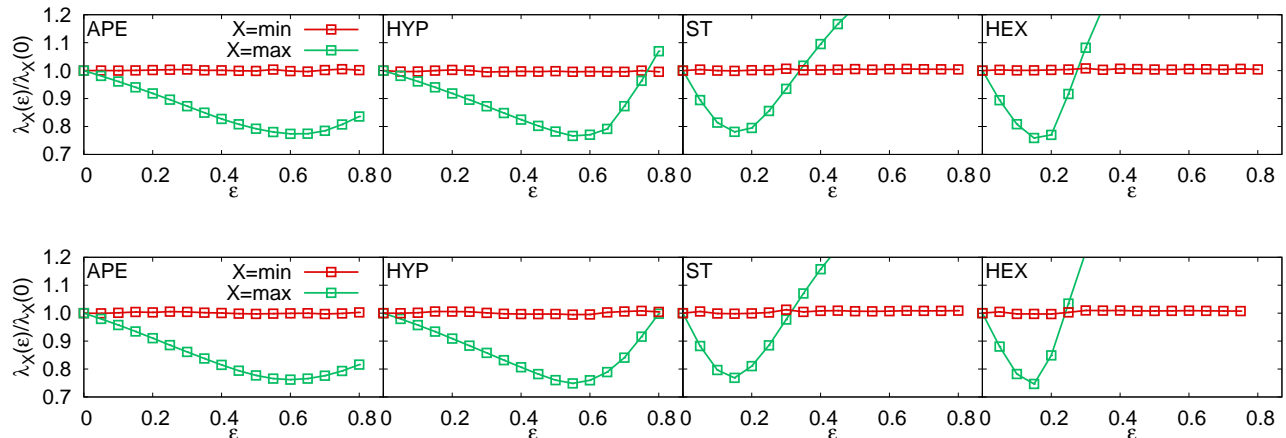
Figure 3.5: The extremal eigenvalues of the massive Dirac operator as a function of ϵ. The top panel is at $\beta = 5.2875$, while the bottom one at $\beta = 5.53$. The maximum eigenvalue is reduced to the minimum at values of ϵ which are close to the optimum values obtained from the gauge sector. The changes in minimum eigenvalue are much smaller than the bare quark mass.

which is easy to check by equating $\nabla y = 0$. The convergence of the solution, x, is monitored through the residue

$$\delta_{CG} = \sqrt{r^\dagger r}, \tag{3.12}$$

where $r = b - D^\dagger D x$. At the minimum (equivalently, after a complete inversion), $\delta_{CG} = 0$. However, in an actual computation, one stops the CG iterations after the residue is less than a tolerance. We call the number of CG iterations taken for $\delta_{CG} < 10^{-5}$ as N_{CG} [45].

Interestingly, conjugate gradient inversion is also optimized at similar values of ϵ. In Figure 3.7, we show N_{CG} in a representative configuration drawn from thermalized ensembles at $\beta = 5.53$. In all the cases, there is about 30% reduction in N_{CG}. Note that the performance of the APE and HYP smeared operators are very similar to each other, just as before. The behavior of the Stout and HEX smearing are also similar, but quite different from the previous pair. Again, the lattice spacing and pion mass make little difference to the optimization. These results on CG are intimately linked to the results on the extremal eigenvalues. In fact, an upper bound on N_{CG}, denoted as N_{CG}^{max}, is related to the condition number

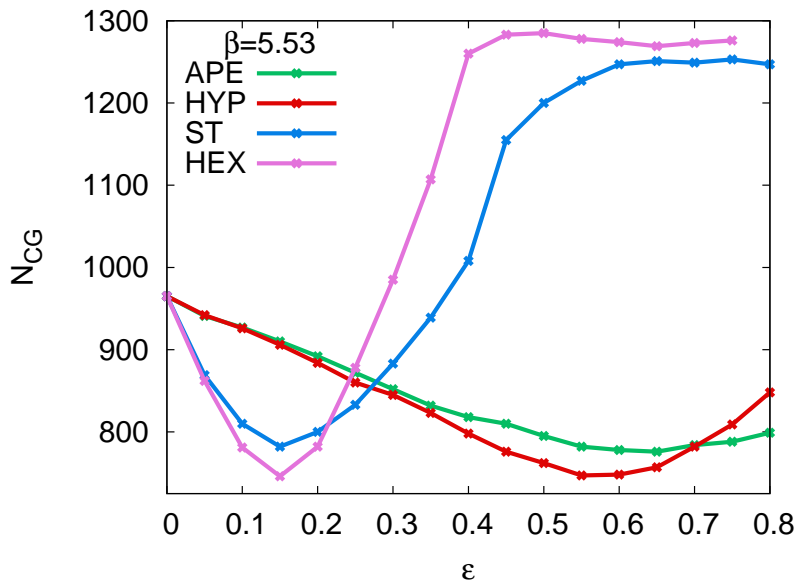$$\kappa \equiv \frac{\lambda_{max}}{\lambda_{min}}, \tag{3.13}$$

Figure 3.6: Computational advantage offered by smearing by a reduction in the number of CG iterations.

as [67, 69]

$$N_{CG}^{max} = \frac{1}{2}\sqrt{\kappa}\ln\left(2\delta_{CG}^{-1}\right). \tag{3.14}$$

In the top panel of Figure 3.7, we plot N_{CG}^{max} as a function of ϵ for HEX. We also show the data points from simulation for comparison. We find that the data points always lie below the upper bound as expected. However, the value of the upper bound itself changes with ϵ, with a minimum value at $\epsilon = 0.15$. Similar behaviours are seen for all the other smearing schemes. We study how N_{CG} is reduced in relation to its upper bound, in the bottom panel of Figure 3.7. Without smearing, CG takes about 12% lesser number of steps than the upper bound. With optimal smearing, we find that it takes about 23% less number of iterations than the upper bound with hypercubic schemes, while it is about 19% for APE and Stout. Thus, the effect of smearing is two fold — it reduces the condition number which in turn reduces the upper bound on N_{CG}, and it reduces the N_{CG} further below this upper bound than in the case of thin-links. Also, as seen in Figure 3.5, the reduction in κ is because of the reduction in λ_{max}.

We collect the results on optimal values of ϵ, as determined from the maximum reduction in Q_{UV}, λ_{max} and N_{CG}, in Table 3.1.
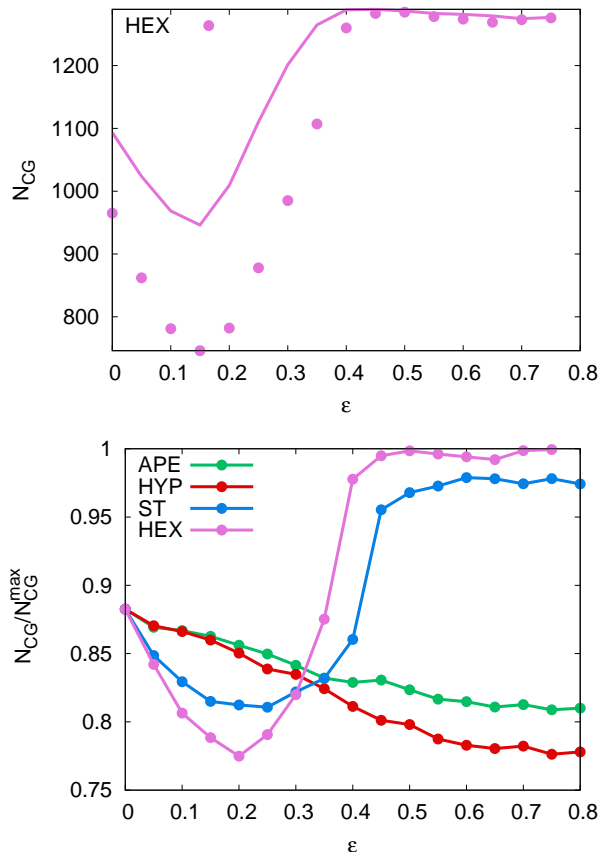
Figure 3.7: Improvement with respect to theoretical maximum. On the top plot, the solid line is the expected upper bound on N_{CG}, given the condition number of $D^\dagger D$ at ϵ. The points are the actual data. On the bottom panel, the ratio of N_{CG} to the upper bound N_{CG}^{max} is shown as a function of ϵ for various smearing schemes.

Scheme	$a = 0.34$fm			$a = 0.17$fm		
	Q_{UV}	N_{CG}	λ_{max}	Q_{UV}	N_{CG}	λ_{max}
APE	0.71	0.65	0.62	0.70	0.65	0.60
HYP	0.65	0.60	0.56	0.65	0.55	0.55
Stout	0.19	0.15	0.16	0.18	0.15	0.14
HEX	0.20	0.15	0.17	0.17	0.15	0.14

Table 3.1: Table of optimum values of smearing parameter, ϵ, obtained through different methods. It is interesting to note that the optimal values obtained through the different methods are close to each other.

3.4 Understanding through Weak-coupling Expansions

In this section, we try to understand the behaviour of plaquette with smearing, using tree level lattice perturbation theory. We follow the calculation done in [70] and [9]. First, we compute the gauge-link smeared plaquette. Using this, we study the behaviour of plaquette with smearing parameter. This gives us an understanding of what values of ϵ can be deemed safe to use.

In a lattice perturbation theory with smeared links [70], one deals with the "familiar" gauge-fields $A_\mu^{(n)}(x + \hat{\mu}/2)$ that are associated with the mid-points of links. These are 3×3 traceless Hermitean matrices belonging to the algebra of SU(3), and they are related to the n-level smeared gauge-links as $U_{x,\mu}^{(n)} \approx \exp\left(iagA_\mu^{(n)}(x + \hat{\mu}/2)\right)$. For the tree-level calculation, we expand $U_{x,\mu}^{(n)}$ to $\mathcal{O}(g^2)$:

$$U_{x,\mu}^{(n)} \approx 1 + igaA_\mu^{(n)}(x + \hat{\mu}/2) - \frac{g^2a^2}{2}A_\mu^{(n)2}(x + \hat{\mu}/2) + \mathcal{O}(g^3a^3). \tag{3.15}$$

The unitarity of gauge-links is lost in such a truncation of the exponential, and it could lead to values of plaquette which are larger than 1 in the case of repeated smearing. Expanding both sides of eq. (3.3) to $\mathcal{O}(g)$, one obtains a recursive formula

$$A_\mu^{(n)}(x) = \sum_{\nu,y} \left[\omega(y)\delta_{\mu\nu} + \omega_{\mu\nu}(y)\right] A_\nu^{(n-1)}(x + y), \tag{3.16}$$

where

$$\omega(y) = \delta_{y,0} + \epsilon \sum_{\hat{\rho}} (\delta_{y,\hat{\rho}} - 2\delta_{y,0} + \delta_{y,-\hat{\rho}}) \quad \text{and}$$

$$\omega_{\mu\nu} = \epsilon \left[\delta_{y,-\hat{\mu}/2+\hat{\nu}/2} - \delta_{y,-\hat{\mu}/2-\hat{\nu}/2} - \delta_{y,\hat{\mu}/2+\hat{\nu}/2} + \delta_{y,\hat{\mu}/2-\hat{\nu}/2}\right]. \tag{3.17}$$

Let $\tilde{\omega}$ and $\tilde{\omega}_{\mu\nu}$ be the Fourier transforms of $\omega(y)$ and $\omega_{\mu\nu}(y)$ respectively. They are given by

$$\tilde{\omega}(k) = 1 - \epsilon\hat{k}^2 \quad \text{and} \quad \tilde{\omega}_{\mu\nu}(k) = \epsilon\hat{k}_\mu\hat{k}_\nu, \tag{3.18}$$

with $\hat{k}_\mu = 2\sin(k_\mu/2)$. Then, one can write eq. (3.16) in terms of the Fourier transforms $\tilde{A}^{(n)}$ of gauge-fields as

$$\tilde{A}_\mu^{(n)}(k) = \sum_{\nu} \left[\tilde{\omega}(k)\delta_{\mu\nu} + \tilde{\omega}_{\mu\nu}(k)\right] \tilde{A}_\nu^{(n-1)}(k). \tag{3.19}$$

By rewriting the above equation in terms of the transverse and longitudinal parts, and then using the recursive formula so obtained, one finally gets an expression in terms of the Fourier transform of thin links

$$\tilde{A}_\mu^{(n)}(k) = \left[\tilde{\omega}^n(k) \left(\delta_{\mu\nu} - \frac{\hat{k}_\mu \hat{k}_\nu}{\hat{k}^2} \right) + \frac{\hat{k}_\mu \hat{k}_\nu}{\hat{k}^2} \right] A_\nu^{(0)}(k). \tag{3.20}$$

Thus, only the transverse part is successively affected, while the longitudinal part remaining unaffected. As interpreted in [70], this is because the gauge-link smearing algorithms are gauge-covariant, and the longitudinal part being fixed by the gauge.

The plaquette, $P^{(n)}$, after n-levels of smearing is

$$P^{(n)} = \frac{1}{3N_P} \sum_x \sum_{\mu\neq\nu} \mathrm{ReTr} \left\langle U_{x,\mu}^{(n)} U_{x+\hat{\mu},\nu}^{(n)} U_{x+\hat{\nu},\mu}^{(n)\dagger} U_{x,\nu}^{(n)\dagger} \right\rangle, \tag{3.21}$$

where the thermal expectation, $\langle\ldots\rangle$, is taken with respect to the Wilson gauge action constructed out of thin-links. N_P is the number of plaquette in the lattice. Using eq. (3.15) and considering only up to $\mathcal{O}(g^2)$, one is left with different contractions of the form $\left\langle \mathrm{Tr}\left[A_\mu^{(n)}(x)A_\mu^{(n)}(x+\hat{\mu})\right] \right\rangle$ and $\left\langle \mathrm{Tr}\left[A_\mu^{(n)}(x)A_\mu^{(n)}(x)\right] \right\rangle$. We reduce these contractions to that among $\tilde{A}_\mu^{(0)}(k)$ using eq. (3.20), after Fourier transformation. These contractions are greatly simplified using the lattice gluon propagator in Feynman gauge, which is $\langle \tilde{A}_\mu^{(0)}(k)\tilde{A}_\nu^{(0)}(k)\rangle = \delta_{\mu\nu}/\hat{k}^2$. Terms such as $\left\langle \mathrm{Tr}\left[A_\mu^{(n)}(x)A_\nu^{(n)}(x)\right] \right\rangle$ do not enter the calculation due to this choice of gauge. Through such simplifications, eq. (3.21) becomes

$$P^{(n)} = 1 - \frac{2}{\beta} w^{(n)}(\epsilon) \quad \text{where} \quad w^{(n)}(\epsilon) = \int_{-\pi}^{\pi} \frac{d^4k}{(2\pi)^4} \tilde{\omega}^{2n}(k). \tag{3.22}$$

The integral in $w^{(n)}$ is evaluated over the entire Brillouin zone.

Using the above result, we study how the mean value of plaquette, after a level of stout smearing, behaves as a function of ϵ. For $n = 1$, the expression for $w^{(1)}$ is simply a quadratic in ϵ: $w^{(1)} = 1 - 16\epsilon + 72\epsilon^2$. This weak coupling result (at $\beta = 10$) is compared with results from simulations at $\beta = 5.2746$ and 5.53 in Figure 3.8. It is interesting to find the tree-level calculation to have the same features as seen in the non-perturbative results; for small values of ϵ, the value of plaquette increases with ϵ and reaches a maximum at $\epsilon = \epsilon_{max}$. The value of ϵ_{max} in the non-perturbative results is about 0.15, while it is 0.11
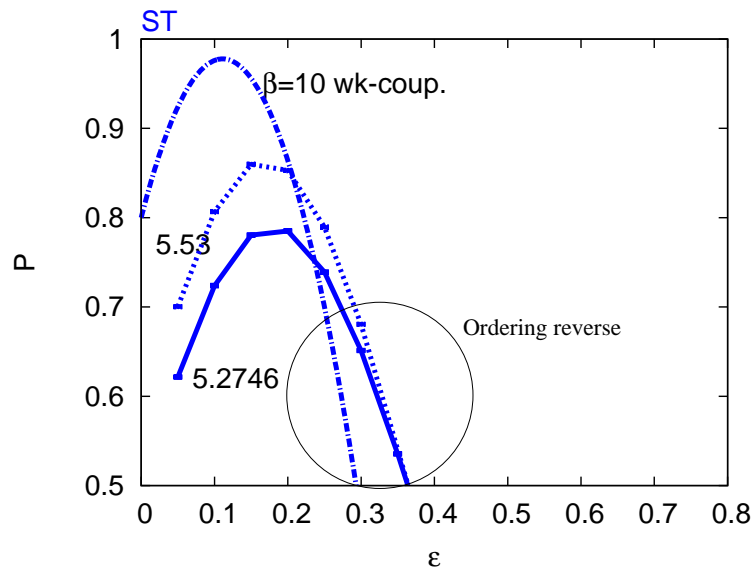
Figure 3.8: The behaviour of mean value of plaquette as a function of ϵ. The result from tree-level weak-coupling calculation is compared with the results at $\beta = 5.53$ and $\beta = 5.2746$, and it is found to describe the ϵ dependence of plaquette qualitatively. The value of ϵ where the plaquette value turns over is ϵ_{max}. At large values of ϵ, there is a reversal of the ordering of plaquette with lattice spacing.

for the perturbative result. With thin-links, value of plaquette increases towards 1 with increase in the value of β. While this ordering of plaquette values with β is preserved for $\epsilon < \epsilon_{max}$, the ordering reverses for values larger than ϵ_{max}. Hence, above ϵ_{max}, the behaviour seems to be disconnected from the behaviour expected without smearing.

A way to understand the behaviour with ϵ, is by considering eq. (3.16). It can be written qualitatively as $A^{(1)} \sim A^{(0)} + \epsilon A^{(0)}$, with $A^{(0)}$ being a place-holder for the unsmeared fields as well as numerical factors excluding ϵ. We call the first term in the right hand side as the unsmeared part and the second term linear in ϵ as the smeared part. The constant term in $w^{(1)}(\epsilon)$ comes from Wick contractions between unsmeared parts, and the term linear in ϵ comes from the contractions between smeared and unsmeared parts. This linear term leads to an increase in the value of plaquette. However, the term quadratic in ϵ is from contractions only among smeared parts. When this term starts dominating, the plaquette value starts decreasing again indicating that this is a result of over-smearing.

3.5   Factorization of Taste Splitting

In the previous sections, we showed quantitatively that smearing indeed suppresses UV. In this section we study the effect of this UV suppression on the pion taste splittings, δm_Γ (refer eq. (1.15) for the definition). Pion taste spectrum has been studied before [14–16] as a function of lattice spacing and due to the reduction in bare quark mass. However, we study the taste spectrum by treating the smearing parameter as one of the variables. This enables us to find an interesting feature of factorization of taste splitting into a purely lattice spacing dependent factor and a smearing dependent factor.

3.5.1   At $T = 0$

We studied the pion taste spectrum, δm_Γ, at $T = 0$ with the couplings $\beta = 5.2746$ and 5.53. The lattice spacing at $\beta = 5.53$ is about half the lattice spacing at 5.2746. We used 16^4 lattice at $\beta = 5.2746$ and 24^4 lattice at 5.53. Using these lattices, we investigated the behaviour of the local-time pions, namely, $\Gamma = \gamma_5, \gamma_i\gamma_5, \gamma_i\gamma_4$ and γ_4 [5, 29]. The non-local time pions occur as parity partners of local time scalar mesons, which we found hard to get a good signal for. We used point quark source and sink. For each configuration, we determined the quark propagators by placing the quark source at the 27 corners of a 3d cube in a time-slice. These are required to construct all the local time pion correlators, as outlined in Section 1.2.4. Our measurements of the pion taste spectrum at the two values of β were partially quenched — the configurations were generated using dynamical standard staggered sea quark action, but the valence quarks were improved using different smeared links in the quark propagators. A caveat is that we did not tune the valence quark mass at different various values of ϵ so as to keep the mass of the pseudo-Goldstone pion constant.

In Figure 3.9, we show the results for the pion taste spectrum on the finer lattice at $\beta = 5.53$. The different panels show the spectrum as a function of ϵ for different smearing schemes. We find that the pion splitting is indeed substantially reduced near the values of ϵ where the UV is optimally reduced. Among the four smearing schemes, HYP smearing seems to perform the best — the taste splittings near the optimal ϵ is reduced by a factor of 5. The ordering of splittings, $\delta m_{\gamma_4} \geq \delta m_{\gamma_4\gamma_i} \geq \delta m_{\gamma_5\gamma_i}$, as expected from staggered chiral perturbation theory [71] is maintained at all the values of ϵ that we investigated.

The taste splittings are functions of lattice spacing, smearing scheme (and its smearing
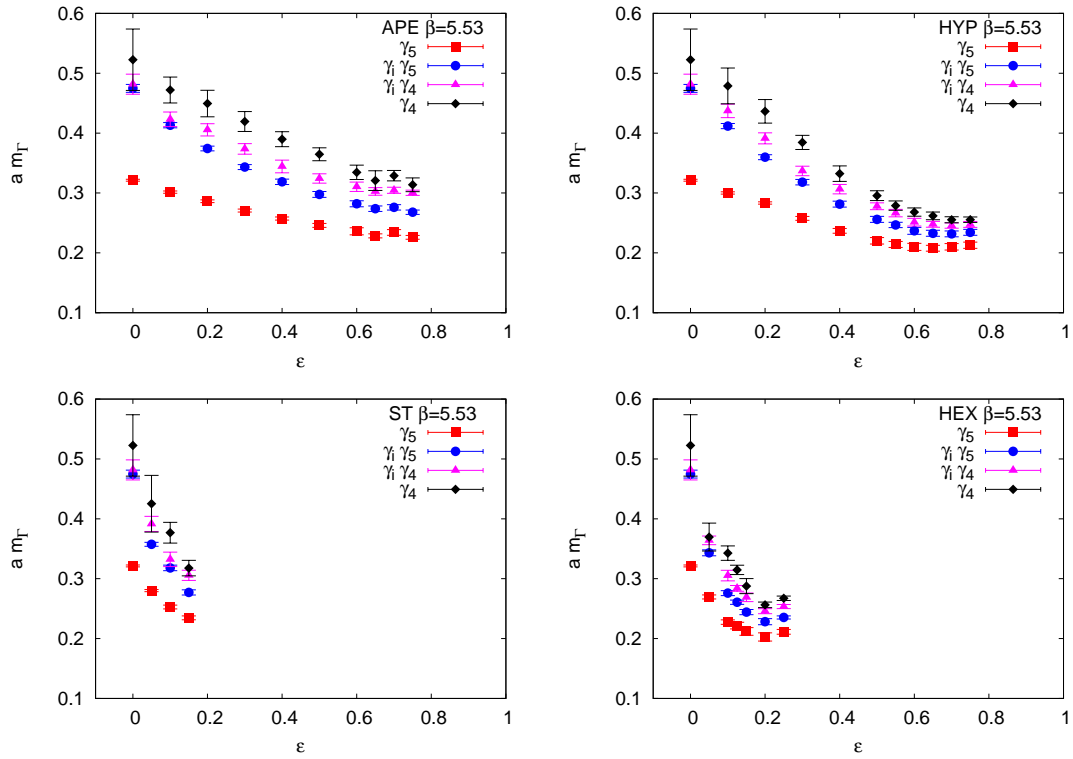
Figure 3.9: Effect of smearing on pion taste partners. Each panel shows the ϵ dependence of the masses of pion taste partners. Taste splitting is reduced by 5 times at optimal ϵ with HYP smearing.
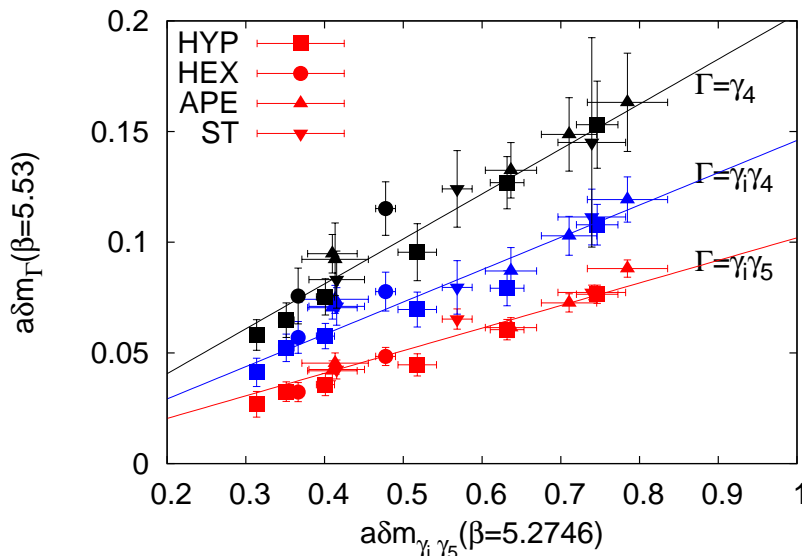
Figure 3.10: Evidence for factorization of pion taste splittings, δm_Γ, into smearing and lattice spacing effects: $\delta m_\Gamma = f(\epsilon)g_\Gamma(a)$. Different δm_Γ at a lattice spacing of $a = 0.17$ fm is plotted against $\delta m_{\gamma_i \gamma_5}$ at $a = 0.34$ fm, with both measured using the same smearing schemes and the smearing parameter values. The different symbols correspond to various smearing schemes, while the color specifies the taste Γ.

parameter). For $\epsilon < \epsilon_{max}$, we find evidence that the dependence on lattice spacing and smearing factorize:

$$\delta m_\Gamma = f(\epsilon)g_\Gamma(a), \tag{3.23}$$

with a suitable normalization $f(0) = 1$. The factor $f(\epsilon)$ is both smearing scheme and smearing parameter dependent. With the above normalization, the factor $g_\Gamma(a)$ is the taste splitting with thin-links. We arrive at the conclusion in eq. (3.23) by plotting the taste splittings, $a\delta m_\Gamma$, at $\beta = 5.53$ as a function of the taste splitting, $a\delta m_{\gamma_i\gamma_5}$, at $\beta = 5.2746$. The taste splittings at the two lattice spacings were determined using the same set of smearing schemes and smearing parameter values. From the plot, we find that irrespective of smearing schemes, the data fall on universal straight lines. This implies the factorization in eq. (3.23). The slopes being different for different taste splittings implies that $g_\Gamma(a)$ indeed depends on the taste Γ. We test these observations quantitatively by fitting a straight line, $y = cx$, to data from each Γ and smearing schemes. The best fit values of c,

| Scheme | $\Gamma = \gamma_i\gamma_5$ | | $\Gamma = \gamma_i\gamma_4$ | | $\Gamma = \gamma_4$ | |
	c	χ^2/DOF	c	χ^2/DOF	c	χ^2/DOF
HYP	0.09(1)	0.17/5	0.14(1)	0.3/5	0.19(2)	0.3/5
APE	0.10(2)	0.1/4	0.15(3)	0.2/4	0.21(3)	0.1/4
HEX	0.11(3)	0.03/2	0.15(3)	0.2/2	0.21(4)	0.1/2
ST	0.09(2)	0.13/1	0.15(2)	0.1/1	0.22(3)	0.4/1

Table 3.2: Testing of hypothesis that $a\delta m_\Gamma(\beta = 5.53)$ versus $a\delta m_{\gamma_i\gamma_5}(\beta = 5.2746)$, for a given Γ, is described by $y = cx$ for all smearing schemes. For each Γ, the best fit values of c are tabulated. Note that the values of c for a given Γ are all consistent with each other.

and χ^2/DOF for the fit are tabulated in Table 3.2. The values of χ^2/DOF are less than 2 for all cases. For each Γ, we find that the values of c are consistent with each other within errors. Thus, the effects of smearing and lattice spacing factorize completely.

This gives a better understanding of smearing — gauge-link smearing offers a computational advantage by making taste splittings nearer to zero at finite a, while their dependences on a remain the same.

3.5.2 At $T > T_c$

Temperature scale with partial quenching

In order to see if there is a shift in the value of cross-over coupling β_c due to gauge-link smearing, we determined β_c using the peak positions of partially quenched Wilson line susceptibility, χ_L, and the unrenormalized chiral susceptibility, χ_M. The result on the cross-over temperatures with various optimal smearing schemes, in terms of T_c without smearing, is shown in Figure 3.11. Smearing seems to have no effect on T_c as determined from χ_L. However, the T_c determined from χ_M seems to slightly shift to smaller values with smearing, but such variations are statistically insignificant. Therefore, we use the same temperature scale as obtained without smearing, for our partially quenched studies.

Super-linear improvement

More information can be extracted from the taste-splitting of the screening masses at finite T,

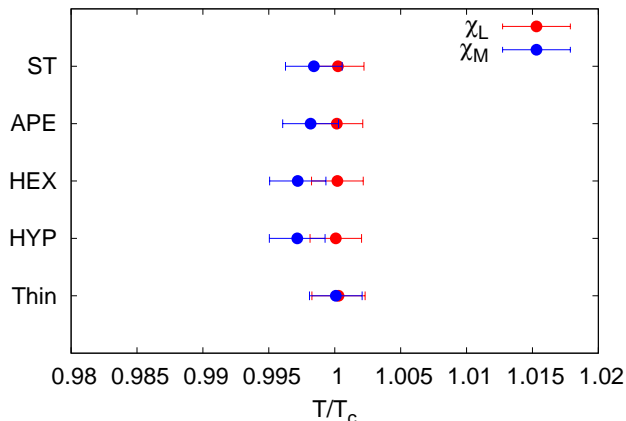$$\delta\mu_\Gamma = \mu_\Gamma - \mu_{\gamma_5}. \tag{3.24}$$

Figure 3.11: Effect of smearing on the cross-over. The width of cross-over is the range of x-axis. No significant change in T_c from the confining-deconfining and the chiral order parameters is seen. This also means that in our partially quenched studies we can use the same temperature scale as set for the thin-links.

The only previous study of this kind was reported in [20]. In Figure 3.12, we show $\delta\mu_{\gamma_i\gamma_5}$ as a function of $a\delta m_{\gamma_i\gamma_5}$. In making this comparison we held the lattice spacing fixed, with one set of measurements at $T = 0$, one at $T = 2T_c$ in set O and a third at $T = 1.33T_c$ in set P. We find

$$\frac{\delta\mu_{\gamma_i\gamma_5}}{T} \propto (a\delta m_{\gamma_i\gamma_5})^2, \tag{3.25}$$

over the range of values we obtained. This removes the ambiguity remarked upon in [20] about the T dependence of taste splitting in the deconfined phase. This super-linear dependences between the taste splittings at $T = 0$ and $T > T_c$ is seen with other sets of taste splittings as well. This means that, if taste splitting is improved by the factor $f(\epsilon)$ at $T = 0$, this leads to an $f^2(\epsilon)$ improvement in the deconfined phase.

One can argue for this on general grounds. A hadron mass, M, can be written as $Ma = f(a\Lambda_{\overline{MS}}, ma, \epsilon)$, where we treat ϵ as a generic label for all the parameters which control smearing. A screening mass, μ, can be written as $\mu/T = g(a\Lambda_{\overline{MS}}, ma, \epsilon, N_t)$, since $N_t = 1/(aT)$, or as $a\mu = g'(a\Lambda_{\overline{MS}}, ma, \epsilon, N_t)$. For data taken at fixed cutoff, $a\Lambda_{\overline{MS}}$, we need not show this parameter explicitly. Although we work at fixed ma, it is profitable to consider the dependence on this variable. A series expansion in ma near the chiral limit
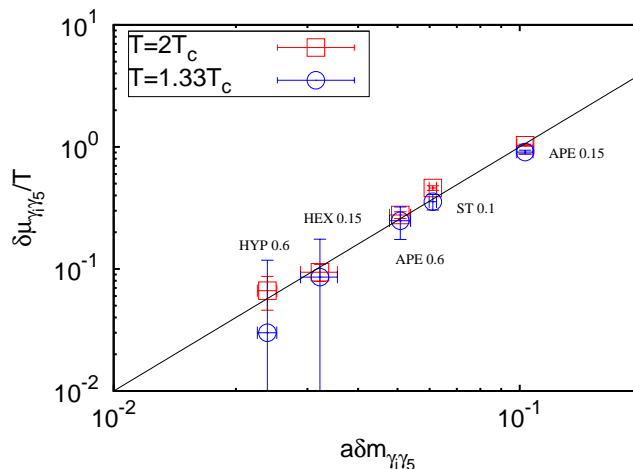
Figure 3.12: Factorization in the deconfined phase. The taste splitting, $\delta\mu_\Gamma$, in the deconfined phase as a function of the corresponding taste splitting, δm_Γ, at $T = 0$ for the taste $\Gamma = \gamma_i\gamma_5$. The different points correspond to the optimal ϵ in different smearing schemes. From the figure, we find that the two taste splittings are related quadratically.

would yield different dependence for the Goldstone pion mass

$$am_{\gamma_5} = \alpha_1\sqrt{ma} + \mathcal{O}\left(ma\right)^{3/2}, \qquad \text{and} \qquad aM = \gamma_0 + \gamma_1 ma + \mathcal{O}\left(ma\right)^2, \qquad (3.26)$$

where M is any other mass scale, and the coefficients depend on ϵ. As a result,

$$a\delta m_\Gamma = \gamma_0 - \alpha_1\sqrt{ma} + \gamma_1 ma \quad \text{and} \quad \delta\mu_\Gamma/T = \gamma_0' + \gamma_1' ma. \qquad (3.27)$$

If taste symmetry were recovered in the chiral limit by tuning ϵ, then one might argue that $\gamma_0 = \gamma_0' = 0$ and hence $a\delta\mu_\Gamma \propto (a\delta m_\Gamma)^2$. This would also mean that all pion tastes are forced to be Goldstones, with an expansion starting at order $\sqrt{ma}$. Chiral logarithms, which we have neglected here, could become important at smaller masses and spoil this scaling.

Even if smearing achieves a more limited goal of significantly decreasing δm_Γ at finite ma without actually recovering taste symmetry completely, one might still recover quadratic scaling. All that is needed is that γ_0 and γ_0' become much smaller than the

actual $T = 0$ taste splitting in the problem. In general one would have

$$\delta\mu_\Gamma/T - \gamma_0' \propto (a\delta m_\Gamma - \gamma_0)^2. \tag{3.28}$$

The data in Figure 3.12 shows that γ_0' and γ_0, are small compared to $a\delta m_\pi$. This quantifies how well smearing works. The fact that it seems to work better at finite temperature than at $T = 0$ with fixed values of $a\Lambda_{\overline{MS}}$ and ma possibly indicates that the Dirac eigenvalue spectrum is simpler. We shall return to this point later.

The main conclusions from these studies of smearing are the following. Optimising the suppression of UV modes automatically improves taste symmetry in the hadron spectrum at $T = 0$, as long as the smearing dependent factor, $f(\epsilon)$, is less than 1. This leads to an $f^2(\epsilon)$ improvement in taste symmetry in the hot phase of QCD. In order to gain most from such an improvement, one should then choose the best possible smearing scheme. With partial quenching, as here, this would mean working with the optimized HYP scheme; with dynamical smeared quarks it would mean working with the optimized HEX scheme.

Chapter 4

Screening Masses with Improved Valence Quarks

This chapter deals with finite temperature staggered lattice QCD with reduced taste breaking. The main emphasis is on the measurement of hadronic screening masses in the deconfined phase. In Section 4.2, we show results pertaining to chiral symmetry restoration in the deconfined phase. In particular, we show that there is an increased degeneracy among mesonic screening correlators as expected from such a restoration. Section 4.3 deals with the spectrum of screening masses using various smearing schemes. In particular, we find that the mesonic screening masses approach the free field theory from above, as predicted by weak-coupling theory. We also demonstrate that an improvement in taste plays a more important role than just decreasing $\mathcal{O}(a^2)$ taste breaking lattice artifacts. In Section 4.4, we understand the reason for such drastic changes in the long distance behaviour of staggered lattice QCD with taste improvement, as due to a slow increase with temperature in the lowest eigenvalue of the unimproved Dirac operator, in the cross-over region.

4.1   Methods

We used set N, O and P in this study. For improving the valence quarks, we used optimal HYP, HEX, Stout and APE smeared links during the construction of quark propagators. We used one level smeared links so that to maintain locality. We used wall source for determining the quark propagators. For this, we gauge-fixed the configurations in Coulomb
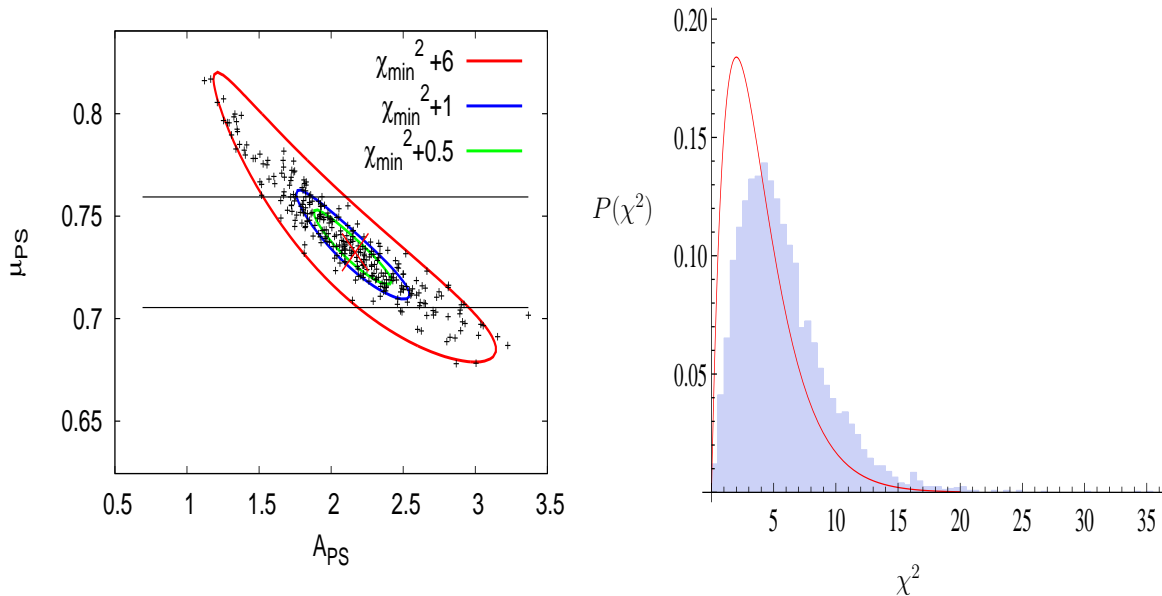
Figure 4.1: **Left panel:** Confidence intervals for the fit parameters for PS at $1.06T_c$. The black points are the scatter of bootstrap values of the fit parameters. χ^2_{min} is the minimum value of χ^2 when the entire sample is used for the fit. The different curves are the lines of constant χ^2. **Right panel:** Comparison of bootstrap histogram (blue) of χ^2_{min} with the χ^2-distribution with 4 degrees of freedom (red curve). Deviations between the two suggest that the underlying distributions are not Gaussian. Deviations from Gaussian behaviour is also suggested by curves of constant χ^2 not being ellipses.

gauge.

We determined the hadronic screening masses by fit, as described in Section 1.2.4. The statistical errors on fit parameters were determined through bootstrap sampling [72]. This helps to avoid the assumption that the distributions of fit parameters are Gaussian. This is important given that the functions being fit (eq. (1.19) and eq. (1.20)) are highly non-linear. Indeed, in many cases there were deviations from a Gaussian behaviour. In the left panel of Figure 4.1, we show the scatter plot for the best fit values of A_{PS} and μ_{PS} in each of the bootstrap samples at $T = 1.06T_c$. The minimum value of χ^2 is χ^2_{min}. The blue solid curve is parametrized by $\chi^2 = \chi^2_{min} + 1$. In the case of a Gaussian distribution, the curve would be an ellipse and its projection onto the screening mass axis would give the 68% confidence interval for μ_{PS}. However, even by eye, the curves are not ellipses. Also, the curve $\chi^2_{min} + 1$ encloses $45(2)\%$ of the scatter, while the expected fraction from

χ^2-distribution with 2 degrees of freedom is 39.3%. In the right panel of Figure 4.1, we compare the bootstrap histogram of χ^2_{min} with the expected χ^2-distribution for 4 degrees of freedom in this particular fit. The two of them should agree in the case of Gaussian distribution, while deviations between the two are clearly seen. This justifies the superiority of bootstrap over a naive estimation of confidence intervals using the covariance matrix for the fit parameters. The band in the left panel, shows the 68% confidence interval for μ_{PS} as estimated from the scatter.

The fit range was varied such that z_{max} was never more than two sites from the middle of the lattice, z_{min} was never less than two sites from the source. Among the fits satisfying $\chi^2/\text{DOF} < 2$, we chose as the reported estimate of the parameter and its error to be that which was consistent with the smallest μ within 2σ and had the smallest error.

4.2 Chiral Symmetry Restoration through Improved Screening Correlators

In Section 1.3.3, we discussed how chiral symmetry restoration in the high temperature phase of QCD is easily seen in hadronic correlation functions. Here we present our results on the correlation functions using optimal HYP-improved valence quarks.

In Figure 4.2, the HYP-improved hadronic screening correlators below and above T_c are shown. Below T_c, the local meson correlators: S, PS, V, and AV are quite distinct, but above T_c they collapse into one (see Figure 4.2). A pairwise degeneracy of the S/PS and V/AV shows chiral symmetry restoration (as discussed in the last subsection), and has been demonstrated earlier as well with thin-link staggered valence quarks. However, we now find the two pairs of A_1^+ irreps to be nearly degenerate at high temperature. This is visible only after smearing and it is a new observation. This occurs in all the data sets: N, O, and P. The confusion that was mentioned in the last subsection, seems to be resolved with improved taste.

Pairwise degeneracy arising from chiral symmetry restoration is most easily seen in the vanishing of $C^{(-S)}$, $C^{(-V_t)}$ and $C^{(-V_s)}$ at high temperature [18]. On examining these combinations, it turns out that the degeneracy for $T > T_c$ becomes clearer with smearing. For example, $C^{(-V_t)}(z = 1/T)$ is $(6 \pm 8) \times 10^{-3}$ at T_c with thin-link valence quarks, but becomes $(0 \pm 2) \times 10^{-3}$ when optimal HYP smeared valence quarks are used. The
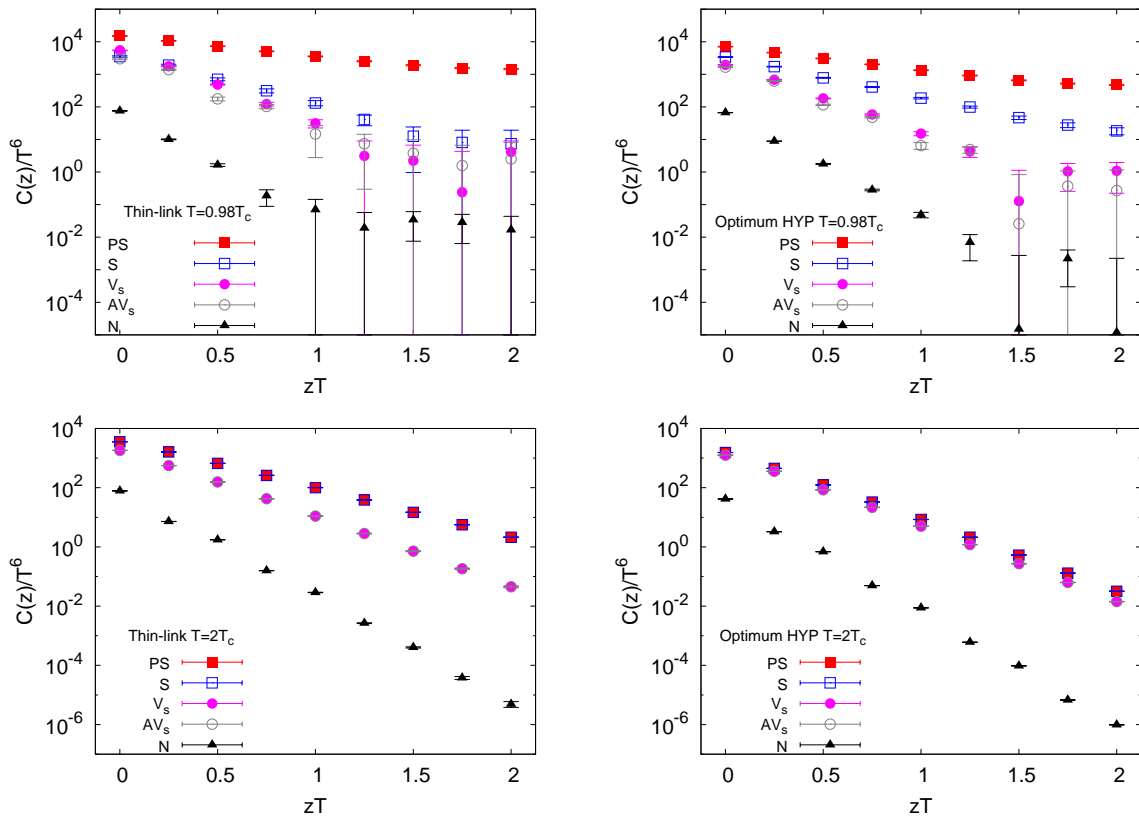
Figure 4.2: Screening correlators from data set N above and below T_c. The signs of chiral symmetry restoration are clear with either thin-link or improved valence quarks in the form of pairwise degeneracies of correlators above T_c. However, improved correlators show even higher degeneracies at high temperature. Similar results are obtained for data sets O and P.
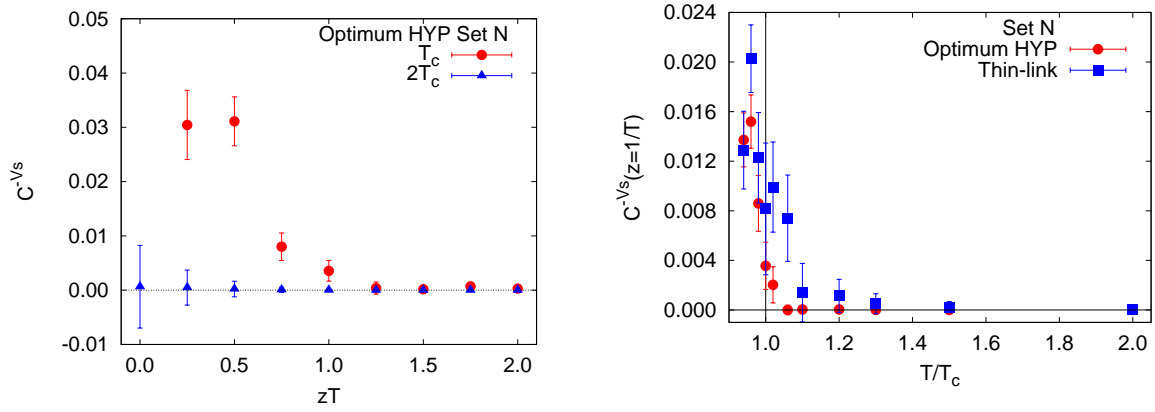
Figure 4.3: The correlator $C^{(-V_s)}$ shows interesting short distance ($z \leq 1/T$) spatial structure slightly above T_c (left). This effect barely persists into the hot phase (right). The results are displayed for set N. Sets O and P show similar behaviour.
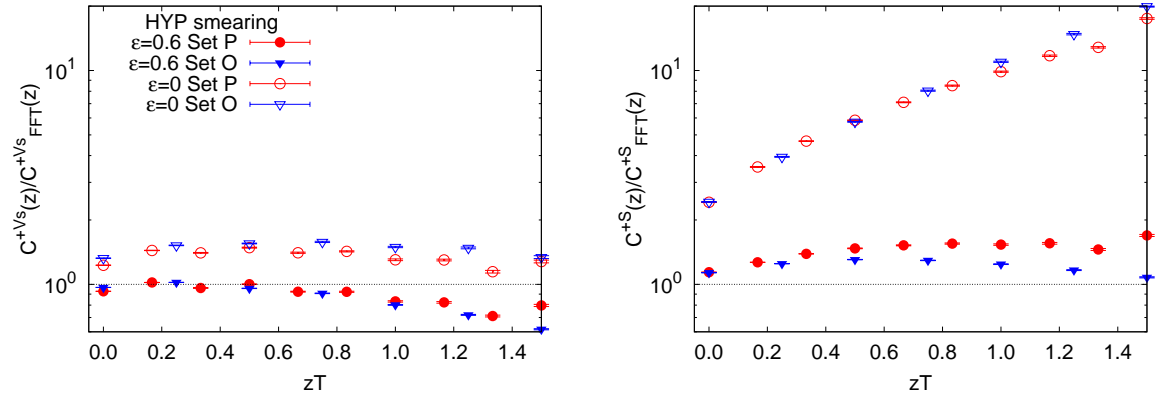

Figure 4.4: The ratio of chiral projections $C^{(+V_s)}$ (left) and $C^{(+S)}$ (right) at $2T_c$ to the respective FFT prediction with data sets O and P. The smeared correlators come close to FFT in both cases, whereas the unsmeared $C^{(+S)}$ is quite different.

improvement is most remarkable in the S/PS sector, where we found $C^{(-S)}(z = 1/T) = -3.3 \pm 0.1$ at T_c using thin-link valence, but -0.57 ± 0.04 using optimal HYP smeared valence. At larger T all the negative chiral projections vanished.

It was seen earlier [18] that $C^{(-V_s)}$ for $T \geq T_c$ vanished when $z > 1/T$, but remained non-zero at short distances. In Figure 4.3 we show this effect at T_c and also, that it vanishes at $2T_c$. A more detailed view of the temperature dependence is exhibited by showing how $C^{(-V_s)}(z = 1/T)$ changes with T. Below T_c the correlator does not vanish, but the spatial structure seems to have entirely disappeared for $T > 1.05T_c$. This gives one definition of the width of the chiral crossover; it is larger than the one implied by $\Delta\beta_c$ (see Section 2.2.2).

$C^{(+V_s)}$ is close to the FFT prediction with either thin-link or smeared valence quarks. With thin-link staggered valence quarks, we see that $C^{(+S)}$ is different from FFT, as previously observed. However, on smearing, they become compatible with FFT (see Figure 4.4). This is a more detailed understanding of why the meson screening correlators are nearly degenerate in Figure 4.2.

4.3   Screening Masses with Improved Taste Symmetry

We determined the screening masses of local mesons and the nucleon using optimal smearing. We did the computation with optimal value of ϵ in each of the four smearing schemes. In the next subsection, we analyse how taste breaking is an important issue to be dealt with in the study of staggered screening masses. In the second subsection, we show the temperature dependence of the screening masses using optimal HYP, where we find a good agreement between meson screening masses in the deconfined phase and the weak-coupling prediction.

4.3.1   Effect of Taste Breaking

In this subsection, we show that the lattice artifacts from taste breaking play a greater role in screening masses than the lattice artifacts that arise from lattice discretization alone.

In Figure 4.5, we show the screening masses of PS, V and the nucleon at $2T_c$ as a function of the taste splitting, $\delta m_{\gamma_i\gamma_5}$. We chose the partner with taste structure $\gamma_5\gamma_i$ as
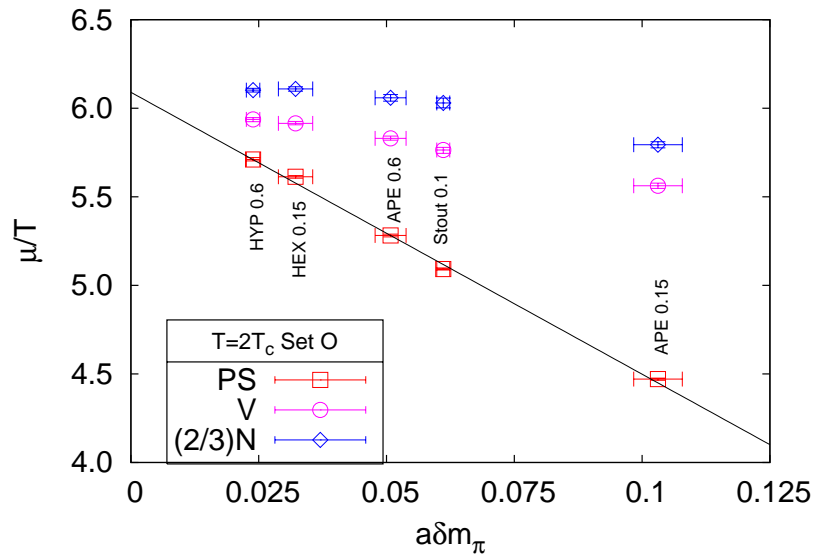
Figure 4.5: The local S/PS, V/AV and N at $2T_c$ as functions of the pion taste splitting $a\delta m_{\gamma_i\gamma_5}$ at $2T_c$ in set O. The screening mass of the nucleon has been multiplied by $2/3$ in order to compress the vertical scale. Each set of screening masses varies linearly with a measure of the pion taste splitting, $a\delta m_{\gamma_i\gamma_5}$. The universal behaviour seen across all smearing schemes means that the variation in screening masses due to smearing is an effect of reduction in taste splitting, and not an artifact of smearing.

an indicator of taste splitting since it is relatively easy to measure. The taste splittings at $T = 0$ and the screening masses were both determined at the same value of $\beta (= 5.53)$. The reduction in taste splitting arises due to gauge-link smearing. The various data points correspond to smearing schemes at optimal values of ϵ (except the data point from APE at $\epsilon = 0.15$ which is non-optimal). We find that they depend on the smearing parameter ϵ essentially only through the taste splitting, δm_Γ. This shows that the changes in the screening masses are due to reduction in taste breaking, and not a smearing artifact.

Figure 4.5 shows the nearly linear dependence of μ/T on $\delta m_\Gamma a$. This linear dependence on taste splitting, along with the factorization which we observed in eq. (3.23) implies a behaviour

$$\mu(a) = \mu_o + h(a) + \lambda f(\epsilon) g_\Gamma \left(\alpha_s a^2 \right), \tag{4.1}$$

where the constant λ is the slope. We have written the y-intercept in Figure 4.5 as $\mu_o + h(a)$, where μ_o is the continuum value of μ, and $h(a)$ is the lattice artifact that remains after the removal of taste-breaking. We have made the argument of g_Γ as $\alpha_s a^2$ to indicate that this term arises due to taste breaking, and it vanishes in FFT. Both h and g_Γ vanish in the continuum limit, but the difference is that h arises from lattice discretization and persists even in FFT. This lattice artifact cannot be altered by gauge-link smearing. In the case of FFT, $\mu_o + h(a)$ would be given by eq. (1.29). Thus, the lattice artifacts contributing to the screening mass split into a purely discretization effect (h), and a purely taste breaking effect (g_Γ) which can be suppressed by smearing through the factor f.

For the sake of illustration, let us assume that for small a, $h(a) \propto a^2$ and $g_\Gamma \propto \alpha_s a^2$. With these lattice artifacts, the schematic dependence of μ on both a and ϵ is shown in Figure 4.6. Without smearing, the slope for the continuum limit is much steeper than the one with optimal smearing. Therefore the results with optimal smearing are expected to be nearer to the continuum even at finite lattice spacing.

Next, we show that the taste breaking artifact contributes largely to the lattice correction in screening mass than the discretization effect from h. In Figure 4.7, we show the temperature dependence of μ_{PS} from three different cases. The blue and the red data points are the optimal HYP-smeared and unsmeared results from set P respectively. Since they are from the same lattice spacing, a comparison between the two shows the contribution from the taste breaking part g_Γ. The black data points are optimal HYP smeared results from set O. Since the taste breaking artifacts are suppressed by a factor
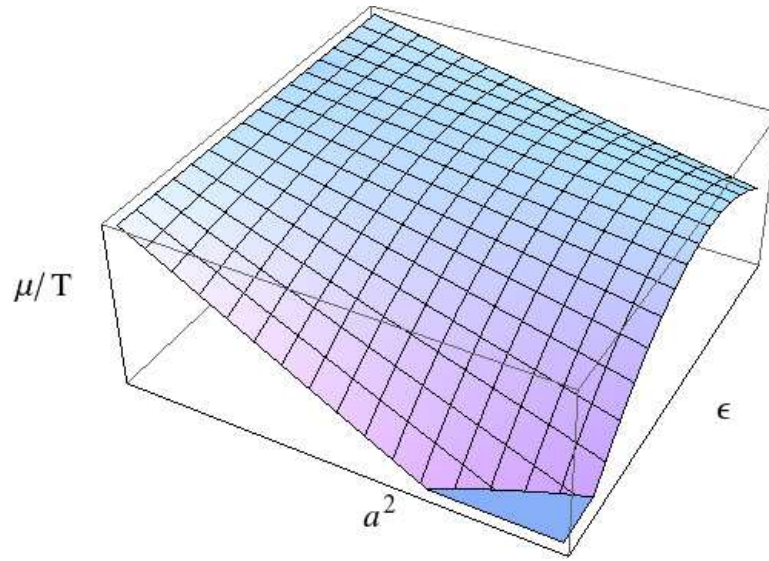
Figure 4.6: Schematic of lattice spacing, a, and smearing parameter, ϵ, dependence of screening mass. At a given value of a, the value of screening mass is closest to the continuum value at optimal ϵ.
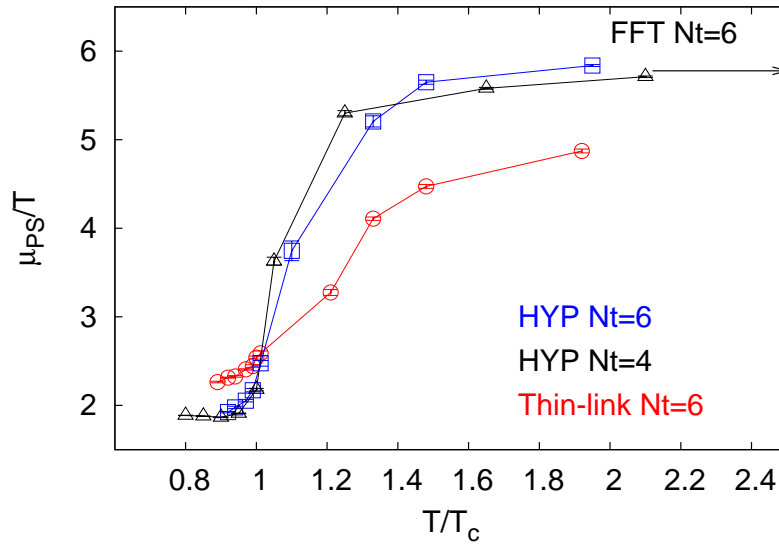

Figure 4.7: The screening masses of PS from two different lattice spacings with optimal HYP and thin-link are shown. The change in values of μ_{PS} measured on two different lattice spacings is much smaller compared to the observed variation due to smearing. This implies that the $\mathcal{O}(\alpha_S a^2)$ corrections are more significant than the $\mathcal{O}(a^2)$ corrections.

6 through optimal smearing, a comparison of these data points with the blue ones show the contribution from discretization artifact h. Above T_c, the shift seen between smeared and unsmeared results is much larger than due to h. This implies that the taste breaking lattice artifacts dominate screening masses in the deconfined phase. The above observations, along with results from Section 3.5, clearly indicate HYP smearing to be the best choice for the study of staggered screening masses.

Below T_c, the screening masses shift to a lower value with decrease in taste breaking. This could be due to improper tuning of valence quark masses. However, the fact that the smeared results at $N_t = 4$ and 6 fall on top of each other seems to indicate that merely reducing the bare quark mass from 0.025 to 0.025(2/3) offers a correct tuning. This is not true in the unsmeared case, where such a tuning leads to a pion which is heavier than expected at finer lattice spacing.

4.3.2 Comparison with Weak-coupling Prediction

The results for the screening masses as functions of T are shown in Figure 4.8 for all three data sets with optimal HYP smearing. Also shown are the values expected in FFT on lattices with the same size (refer eq. (1.29)). The analysis of correlation functions obtained with these smeared valence quarks shows that the screening masses in all channels approach FFT at high T. The most striking new feature of this data is that this approach is from above, in conformity with the predictions of [11]. Similar results are obtained with optimal HEX smeared quarks.

We have shown in Figure 4.5 that there is a remaining uncertainty of around 15% in the determination of the S/PS screening mass. This comes from the residual taste symmetry breaking at the best optimization of the screening parameters possible at this lattice spacing. Reduction of this uncertainty requires going to finer lattices.

From the discussions in Section 1.4, the weak coupling prediction for the meson-like screening masses is

$$\mu = \mu_{FFT} + \frac{4}{3}\alpha_s[1 + 2E_0]T. \tag{4.2}$$

Here α_s is the 2-loop QCD coupling evaluated in the $\overline{MS}$ scheme at the scale $2\pi T$. $E_0 = 0.3824$ for two flavours of quarks in a dimensional reduction (DR) scheme [11]. A hard thermal loop (HTL) re-summation which neglects soft gluon contributions to the vertex yields $E_0 = 0$ [12]. These weak-coupling predictions are also shown in Figure 4.8. The
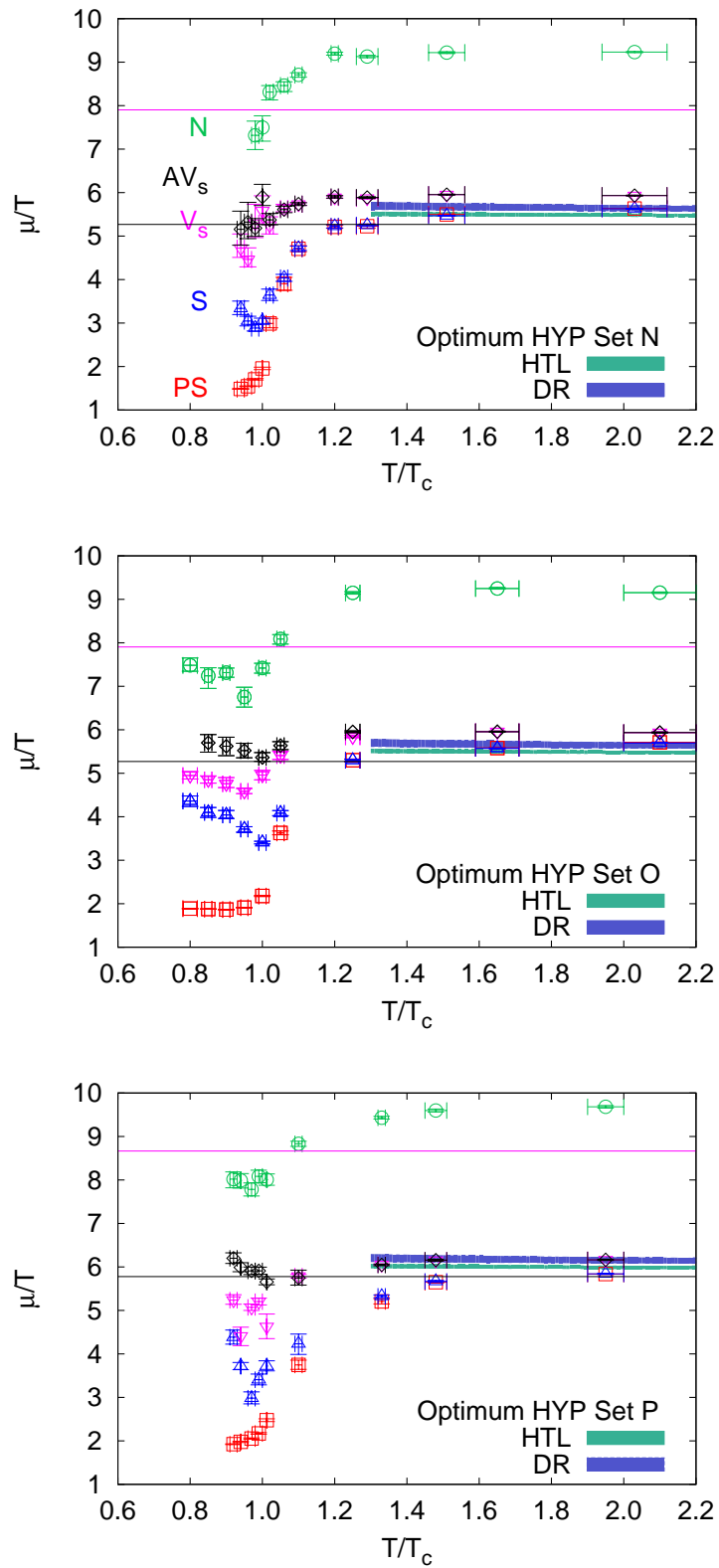
Figure 4.8: Hadron screening masses for the data sets N, O, and P using optimum HYP smeared correlators. The horizontal lines are the free theory screening mass for the nucleon and the mesons respectively. The error bands for HTL and DR weak coupling predictions are shown.

uncertainty bands are obtained by varying the momentum scale for the determination of α_s from πT to $4\pi T$, and also from the uncertainty in $T_c/\Lambda_{\overline{MS}} = 0.49(2)$ [62].

Since there is no computation with weak coupling on a lattice, the effect of finite lattice spacing on E_0 cannot be estimated. Therefore, we use the continuum value of E_0 in our calculations. We take care of the leading $\mathcal{O}(a^2)$ correction by replacing the continuum FFT value of $2\pi T$ with the lattice value in eq. (1.29). Our approximation is justified because any leading $\mathcal{O}(a^2)$ correction to E_0 will only contribute as an $\mathcal{O}(\alpha_s a^2)$ correction to μ. But, as we have seen, gauge-link smearing greatly reduces this $\mathcal{O}(\alpha_s a^2)$ lattice corrections.

As one can see, both the weak-coupling predictions are close to the observed screening masses. Very little difference in screening masses is seen above $1.5T_c$ between set N and O. This means that we commit less error by using the same value of bare quark mass for both the valence and sea quarks. The agreement with weak coupling is seen in both the lattice spacings of set O and P. We defer our speculations about the continuum limit to the discussions.

In addition, we also find the nucleon to approach FFT from above, which is not a prediction from weak coupling calculations.

4.4   Smallest Eigenvalue of Dirac Operator

The rapid approach to behaviour similar to weak-coupling theory has implications for the spectrum of the staggered Dirac operator. It was shown earlier in a study of set O with thin-link quarks that a gap developed in the massless staggered eigenvalue spectrum a little above T_c, and that the hot phase contained localized Dirac eigenvectors [21]. We determined the lowest eigenvalue using Lanczos algorithm. We refer the reader to Section 3.3.2 for details.

4.4.1   Spectral Gap with Improved Taste

Here, we studied the spectral gap by measuring the smallest eigenvalue of the massless staggered Dirac operator, λ_0. The ensemble average, $\langle \lambda_0 \rangle$, at a given temperature was generally seen to be within a factor of four of the minimum over the ensemble. In view of this, we report $\langle \lambda_0 \rangle$.

As can be seen in Figure 4.9, it climbs by two orders of magnitude between T_c and
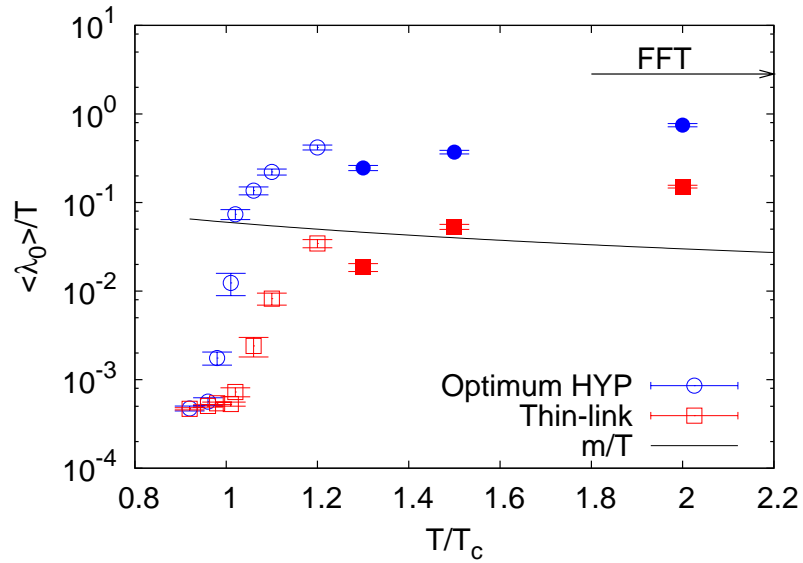
Figure 4.9: The ensemble averaged smallest eigenvalue of the massless staggered Dirac operator, $\langle \lambda_0 \rangle$. The open symbols are measurements made on lattices with aspect ratio $LT = 4$, while the filled symbols corresponds to $LT = 6$. The results are shown for set N; with optimal HYP smearing (blue circles), the eigenvalue rises by two orders of magnitude in a narrow range above T_c. For the thin-link Dirac operator, the rise is much slower (red squares). The effect of taste breaking is to make $\langle \lambda_0 \rangle$ rise slowly with temperature, thereby affecting all other screening phenomena.
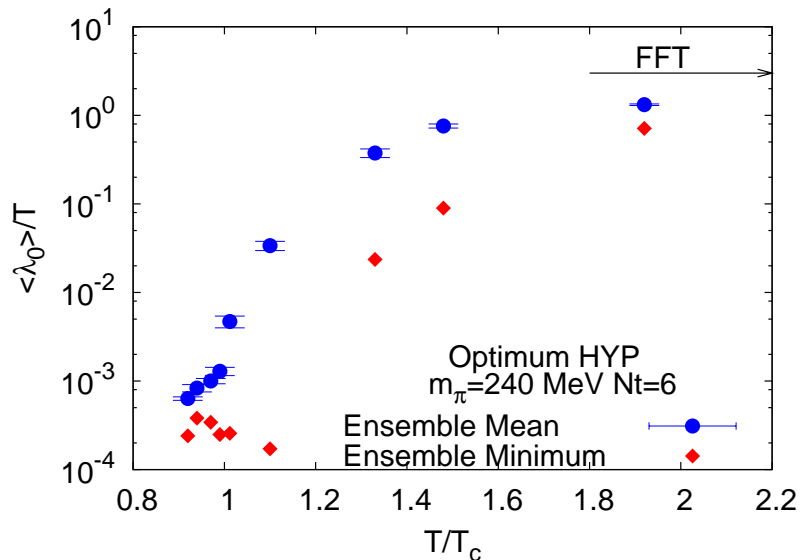
Figure 4.10: The ensemble minimum of the smallest eigenvalue of the massless staggered Dirac operator. The ensemble minimum of λ_0 is shown along with $\langle\lambda_0\rangle$ for set P. Atypically small eigenvalues are seen even till $1.2T_c$.

$1.06T_c$ for the smeared Dirac operator. For the thin-link operator, $\langle\lambda_0\rangle$ rises at significantly higher temperature. One sees some volume dependence in the result. This was studied extensively in [21], where it was found that the volume dependence becomes negligible when the spatial size, L, is of the order of $1/\langle\lambda_0\rangle$. For $LT = 4$, this would be at $\langle\lambda_0\rangle \simeq 0.25$, which seems to happen at $1.5T_c$.

It is also of interest to note that $a\langle\lambda_0\rangle$ becomes comparable to am at $T = T_c$ with optimum HYP smearing. With thin-link quarks this crossing is delayed to $T/T_c \simeq 1.5$, thus affecting all screening phenomena.

4.4.2   Existence of Atypical Configurations

Atypical configurations with very small eigenvalues have been linked to topological configurations by observations with overlap [73] or HISQ quarks in [74]. This is interesting to a study of axial U(1) symmetry at finite temperature.

We characterize the occurrence of extremely small eigenvalues by finding the smallest eigenvalue in $N, N/2, N/4, \ldots$ randomly sampled configurations (where N is the total

number of configurations). Smallest such sample where such extremely small eigenvalues are found characterizes the rare event. In both the sets N and P, even at $1.2T_c$, we spotted one configuration out of the 50 for which λ_0 was two orders of magnitude below $\langle\lambda_0\rangle$. The result for set P is shown in Figure 4.10. This implies the existence of a small fraction of atypical configurations in the thermal ensemble. However, this requires a much larger statistical sample, and we therefore leave it to the future.

Chapter 5

Conclusions

Several properties of quarks at experimentally accessible temperatures above T_c seem to be explained in weak coupling QCD. However, one which showed puzzling departures from weak-coupling predictions was screening masses from hadronic excitations. In quenched computations it was seen that the results depended strongly on the kind of valence quark used [54]. With this clue in hand we performed computations with dynamical staggered sea quarks and improved valence quarks in three sets of computations, one new (set N, see Table 2.1) and two older, (sets O [45] and P [57]). Studies with staggered valence quarks were reported earlier with set P [18].

A part of this work was the optimization of the valence quarks. We used four popular versions of fat-link staggered quarks. We optimized the smearing parameter, ϵ, in each case by observing changes to the power spectrum of the plaquette (see Figure 3.3) and the largest and smallest eigenvalues of the Dirac operator (see Figure 3.5). The optimum ϵ was chosen so that the UV was suppressed as much as possible without changing the IR behaviour in both cases. This also improved the performance of the conjugate gradient algorithm used for the inversion of the Dirac operator. Such a tuning was done at $T = 0$. We measured the spectrum of local-time taste partners of pion as a function of smearing parameter in the four different schemes at two different lattice spacings. Through this study, we learnt that taste splitting factorizes into a smearing dependent part $f(\epsilon)$ and a lattice spacing dependent part $g(a)$. As long as $f(\epsilon)$ is less than 1, smearing offers a computational advantage. This factor reduces the taste splitting by about a factor of 6 in the case of optimal HYP at our finest lattice spacing. Such a factorization is also seen in the taste splitting of pseudoscalar screening masses in the deconfined phase. However, we
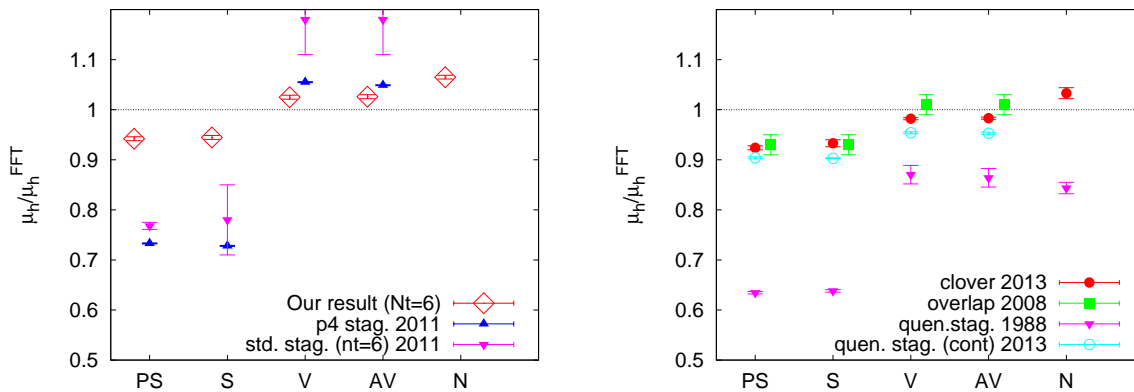
Figure 5.1: Comparison of screening masses with different quark actions at $1.5T_c$. Results for dynamical calculations are shown in the left panel, while quenched calculations in the right. The left panel now includes our results on $N_t = 6$ with optimum HYP (red diamonds). The right panel now includes the continuum extrapolated result from the quenched staggered calculation [75] (aqua circles). The panels also include the older results: Clover 2013 [54], overlap 2008 [55], p4 stag [19], std. stag 2011 [18] and quen. stag. 1988 [56].

found that the smearing dependent factor to behave as $f^2(\epsilon)$. Thus, an improvement in taste at $T = 0$ is found to cause a super-linear improvement at $T > T_c$ (see Figure 3.12).

Smearing causes systematic changes in finite temperature properties of interest. We found that the screening mass in the hot phase increases systematically as taste symmetry breaking is reduced at $T = 0$ (see Figure 4.5). Since recovery of taste symmetry has been used as the main indicator of the reduction of UV effects, it is natural in this study to use optimized HYP smearing in order to best reduce lattice artifacts.

On doing this we find that the screening correlator recovers the degeneracies that a theory of weakly coupled fermions would predict (see Figure 4.2). This happens very close to, and above, T_c (see Figure 4.3). The correlators themselves are also close to the predictions of a free fermion field theory (see Figure 4.4). Consistent with this, the screening masses at high temperature are found to be close to weak-coupling theory (see Figure 4.8) in all the three sets N, O and P — meson screening masses approach free field theory from above. We could find by comparisons between screening masses, found with and without smearing at two different lattice spacings, that the taste breaking artifact in screening masses are more dominant than the purely discretization artifacts.

The updated version of Figure 1.5 with results on screening masses at $1.5T_c$ from studies after the year 2013, are given in Figure 5.1. This now includes our partially quenched results on $N_t = 6$ with HYP smearing (shown as open red diamonds), and the quenched results from [75], where both the continuum and thermodynamic limits are taken (shown as the unfilled aqua circles). Only in the continuum and thermodynamic limit, the unimproved staggered results are seen to be in rough agreement with results from other quark actions. Our result on the other hand suggests that by taking care of taste breaking, one can obtain results which are closer to the continuum even at finite lattice spacings.

We also see that the smallest eigenvalue of the optimally HYP smeared massless staggered Dirac operator shows a rapid jump from extremely small values in the mean below T_c to fairly large values above (see Figure 4.9). The behaviour of the thin-link staggered operator is qualitatively similar, although quantitatively slower to change, thereby affecting all screening phenomena. Since the smallest eigenvalue of the massless smeared operator is comparable to the bare mass already at $T = T_c$, the limit of physical renormalized mass becomes easy to take in the high temperature phase. There is evidence for a very small fraction of completely atypical configurations in the hot phase (see Figure 4.10). A study of the topology of these gauge configurations lies outside the scope of this thesis.

Appendix A

Tuning R-algorithm

A.1   Reversibility of the Algorithm

A standard method for dynamical simulation of QCD is by simulating an equivalent micro-canonical ensemble of a fictitious classical system [76]. A trajectory in hybrid molecular dynamic evolution consists of an initial refreshment of momenta $\Pi_{x,\mu}$ conjugate to $U_{x,\mu}$, followed by classical evolution of gauge fields and the conjugate momenta through the molecular dynamics time, τ, (called MD time) according to a fictitious Hamiltonian, H. The momenta are evolved such that H is conserved. But in an actual simulation, a trajectory of length T_{traj} is discretized into N_{MD} time steps each of size Δt.

R-algorithm [34] is one of the hybrid molecular dynamics methods [3]. At finite values of Δt, R-algorithm is only approximate, as there is no Metropolis accept-reject step [3, 77] at the end of a trajectory, unlike the case of Hybrid Monte Carlo [68]. This introduces Δt-corrections to measured quantities, and these are reduced to $\mathcal{O}(\Delta t^2)$ in R-algorithm. This means that approximations at the same order could be made in the algorithm.

Exact reversibility of the algorithm is one of the requirements to maintain detailed balance. Since R-algorithm is accurate only to $\mathcal{O}(\Delta t^2)$, the implementation of leap-frog integrator used in R-algorithm is reversible only to $\mathcal{O}(\Delta t^2)$. This is in addition to re-versibility violations that arise due to rounding errors and stopping criterion for conjugate gradient (which are the only factors contributing if HMC is used [78]).

We study the violation of MD time reversibility by evolving the gauge-links $U_{x,\mu}$ through a trajectory with N_{MD} time steps, each of size Δt. At the end of the trajectory, we reverse the momenta, $\Pi_{x,\mu} \rightarrow -\Pi_{x,\mu}$, and the links are made to retrace the

trajectory in reverse [78]. The gauge-links obtained after this to-and-fro MD evolution is called $U'_{x,\mu}$. At the end, we measure the overlap between U and U' using

$$\rho = 1 - \frac{1}{12V_{lat}} \sum_{x,\mu} |\text{Tr}\left(U^\dagger_{x,\mu} U'_{x,\mu}\right)|. \tag{A.1}$$

With perfect reversibility, ρ would be zero.

A.2 Tuning with Plaquette

As noted earlier, R-algorithm is approximate due the absence of Metropolis accept-reject step in order to correct for the finite step size errors. Therefore, the values of N_{MD} and Δt have to be tuned so that different measured quantities are consistent with the values obtained in the $\Delta t \to 0$ limit. A quantity which is well measured on the lattice is the plaquette, making it suitable for tuning the algorithm. In Figure A.1, we show the spatial plaquette, P_s, as a function of N_{MD}. The data are taken from simulations on 4×8^3 lattice at $\beta = 5.25$, with the bare quark mass $am = 0.015$. In all the runs, the trajectory length, T_{traj}, was fixed as 1 in MD time units. We optimized the algorithm by finding the largest possible value of Δt, whose plaquette value is consistent with the value obtained on the smallest value of Δt used. We found $\Delta t = 0.01$ to satisfy this criterion, and we chose this to be the optimum value to be used in our configuration generation of the finite temperature ensemble with $am = 0.015$, called set N and discussed in Chapter 2.

Changes due to an update of a gauge-link, propagate to other parts of the lattice ballistically [79] (as opposed to, say, being diffusive). Therefore, in order to maintain a fixed auto-correlation time in simulations across different lattice sizes, one needs to increase the length of the trajectory (*i.e.*, increase N_{MD}) in proportion to the linear dimension of the lattice. Which means, for the set N, we use $N_{\text{MD}} = 100(N_s/8)$, where N_s is the spatial extent of the lattice. But, not all values of N_{MD} are acceptable for a given value of Δt. In Figure A.2, we show the Monte Carlo history of P_s for the case of $\beta = 5.275$ in set N on 4×24^3 lattice. We used $\Delta t = 0.01$ as before, while changing N_{MD} to larger values than $N_{\text{MD}} = 300$. The runs with $N_{\text{MD}} = 500, 600$ and 700 were started from the same thermalized configuration. It is easily seen that the run time histories are different as one goes to larger values of N_{MD}. This means that the $\mathcal{O}(\Delta t^2)$ errors are getting amplified by the increase in N_{MD}. Thus, one has to be judicious in the choice of the pair $(\Delta t, N_{\text{MD}})$.
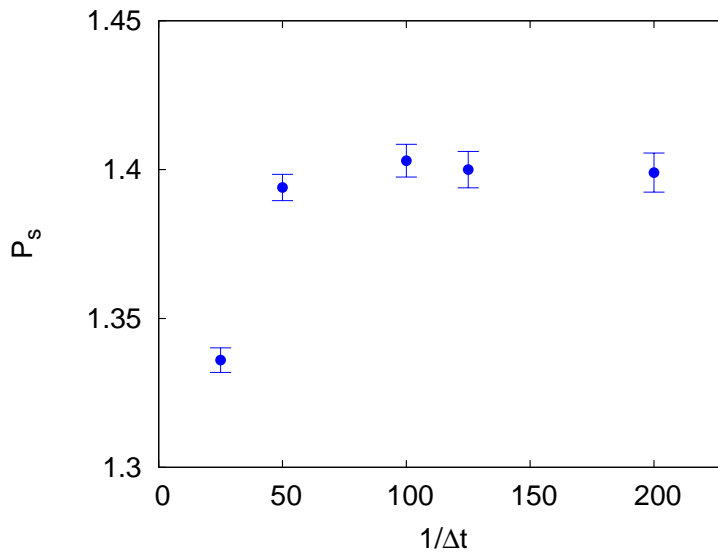
Figure A.1: Plot of spatial plaquette at $\beta = 5.25$ on 4×8^3 lattice, as a function of the number of MD time steps, N_{MD}, keeping a fixed length of trajectory, $T_{traj} = 1$.

This is explored in detail in the next section.

A.3 Reversibility as a Criterion for Tuning

We find that ρ offers a quick way of tuning the algorithm, instead of running actual simulations to choose the pair of parameters by trial and error. Since an exact time reversibility is required for an exact algorithm, any measure of deviations from it should serve to tune the algorithm. Also, the violation in time reversibility in R-algorithm is $\mathcal{O}(\Delta t^2)$ like the Δt-corrections to measurements, making it a good proxy for actual measurements.

In Figure A.3, we show ρ as a function of the pair $(\Delta t, N_{\mathrm{MD}})$. The bare quark mass decreases as we go from black, blue and green points, in that order. The difference between the green and blue data sets lie only in the lattice size used in the study. We arbitrarily chose a tolerance in ρ to be $\rho_c = 0.001$, which is shown as the magenta line. We chose this value because the typical statistical errors in plaquette encountered in our finite temperature simulations were of that order, and thereby requiring the algorithm to be accurate only to that significant digit. For a given am, the values of N_{MD} that can be used to maintain ρ to be less than ρ_c, becomes smaller with increase in Δt. For the set
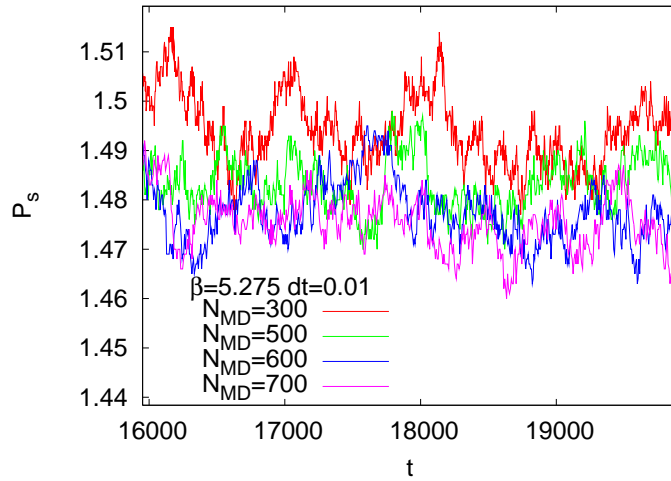
Figure A.2: Run time history of spatial plaquette, P_s, along the MD time, t. The value of MD time step, Δt, is 0.01 for all the runs. The different colours are for different values of N_{MD}. As N_{MD} increases, the histories are very different from each other.
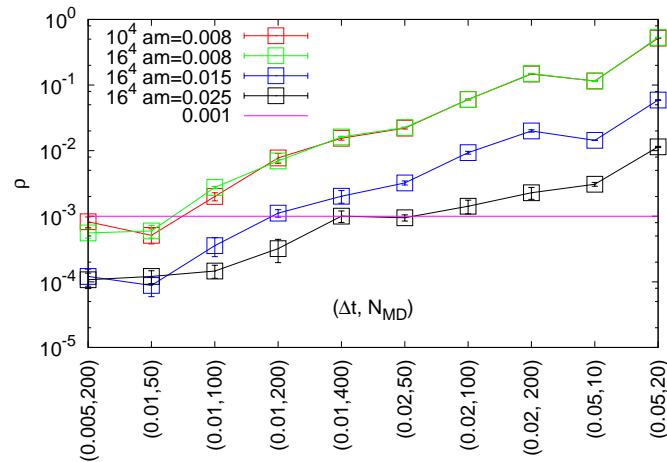

Figure A.3: The result for ρ for different sets of $(\Delta t, N_{\mathrm{MD}})$ are shown below. The black points are for a quark mass of 0.025, the blue ones for am=0.015 and the green ones for $am = 0.008$, on 16^4 lattice. The volume dependence is tested at $am = 0.008$ using 10^4 lattice which is shown using red points. The magenta line marks a tolerance of 0.001, which is chosen as the typical error encountered for plaquette.

N which has $\Delta t = 0.01$, the largest value of N_{MD} that can be used seems to be around 200. This explains why the run-time histories in Figure A.2, with $N_{\mathrm{MD}} > 300$ are very different. When the quark mass is decreased, the value of Δt that can be used for a given value of T_{traj}, becomes smaller. This means an additional increase in the computational effort when simulating at smaller quark mass using R-algorithm.

By making a detailed scan of different sets of $(\Delta t, N_{\mathrm{MD}})$ at $am = 0.008$, we were able to divide the parameter space into allowed and disallowed regions (based on whether ρ is less than or greater than ρ_c respectively). Ten different configurations were used for this purpose. The data points are from actual simulations — the magenta points had plaquette values which differed from the values at $(0.002, 100)$ by less than the statistical error, while the black point differed by more than 1-σ. The blue band is the error band for finding $\rho = \rho_c$. From the plot we find that $\rho = \rho_c$ clearly separates the parameter space into two, consistent with what we observe from actual simulation. This boundary between the allowed and disallowed regions seems to be described by

$$(\Delta t)^2 N_{\mathrm{MD}} = A \tag{A.2}$$

with the value of $A = 0.0074$ in this particular case. This means that the $\mathcal{O}(\Delta t^2)$ discretization errors get accumulated with every MD time step in a trajectory. This again reiterates the observation that not all values of N_{MD} are allowed for a given Δt.

The value of the coefficient A in eq. (A.2), indeed depends on the value of ρ_c which is chosen. In Figure A.5, we plot ρ as a function of N_{MD} for different fixed values of Δt. Over a wide range of T_{traj}, which is not very large, ρ seems to scale with N_{MD} as $\rho \propto N_{MD}^{\gamma}$, where $\gamma \approx 1.38$. Along with eq. (A.2), this scaling implies $(\Delta t)^2 N_{\mathrm{MD}} \propto \rho^{1/\gamma}$.
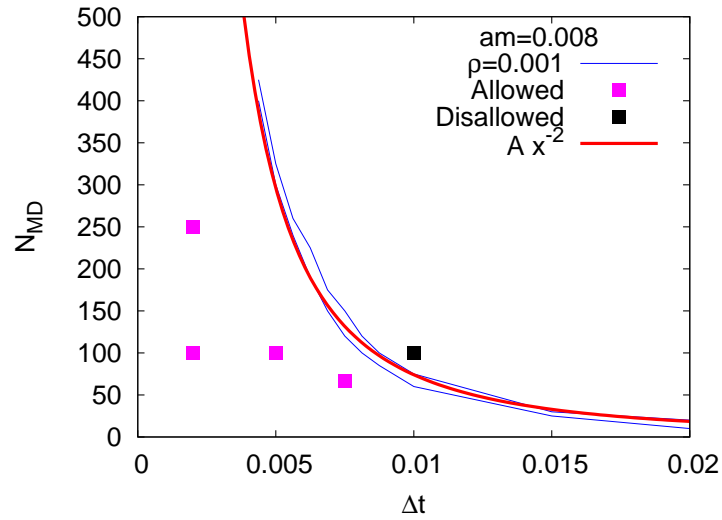
Figure A.4: Allowed and disallowed regions of the parameter space for a bare quark mass $am = 0.008$. The blue band separates regions which have values of ρ less than and greater than a tolerance $\rho_c = 0.001$. The symbols are from actual dynamical simulations.
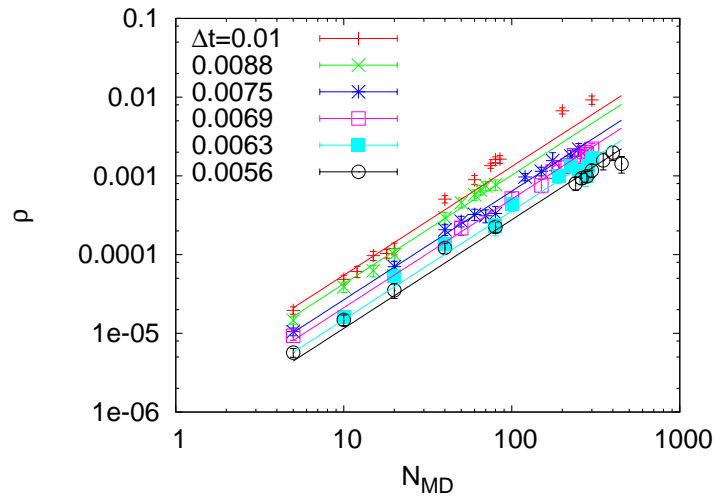

Figure A.5: Scaling of ρ with N_{MD} for fixed values of Δt. The different symbols belong to different Δt. The lines describe the power-law $\rho \propto N_{MD}^{\gamma}$ for different Δt. The value of the exponent $\gamma \approx 1.38$ in all the cases.

Appendix B

Memory Optimized Implementation of HEX

A code implementation of eq. (3.4) requires arrays U_μ and $V_{\mu;\nu}$ to store thin-links and the subsequent smeared links in various sub-levels respectively. Each of these arrays store 3×3 matrices at all lattice points and hence each of them is of size $9V_{lat}$. Since each step consists of updates done at all lattice points, we do not show the position indices of these arrays. In addition to them, we require arrays W_i for $1 \leq i \leq N_w$. These are required in order to provide work space to enable updating the same array $V_{\mu;\nu}$ with smeared links, when going from one sub-level to the next. Each of these arrays are again of size $9V_{lat}$. The problem is to minimize N_w. The first sub-level is easy to implement as it requires only thin-links and the $V_{\mu;\nu}$ are empty to begin with. This step does not require any working arrays.

The smeared links, $V_{\sigma;\mu\nu}^{(1)}$, used in the second sub-level can also be written as $V_{\sigma;\eta}^{(1)}$, where η is the direction orthogonal to σ, μ and ν. With this observation, it is clear that both $V_{\sigma;\mu\nu}^{(1)}$ and $V_{\sigma;\eta}^{(2)}$ can be stored in the same array of the form $V_{\sigma;\eta}$. The brute force implementation of this sub-level would require $N_w = 12$, as two copies of V are required: one to store $V^{(1)}$ and the other for $V^{(2)}$.

A graphical representation of an algorithm to compute the second sub-level, so that N_w is reduced to 7, is given in Figure B.1. The vertices (μ, ν) stand for the arrays $V_{\mu;\nu}$. Two vertices (μ, ν) and (ρ, η) are adjacent, if eq. (3.4) for $V_{\mu;\nu}^{(2)}$ involves $V_{\rho;\eta}^{(1)}$. If this is true, then by observation, $V_{\rho;\eta}^{(2)}$ also involves $V_{\mu;\nu}^{(1)}$ and hence this graph is not directed. At the beginning of the second sub-level, (μ, ν) contains $V_{\mu;\nu}^{(1)}$ at all lattice points. (μ, ν)

cannot be updated with $V_{\mu,\nu}^{(2)}$ until the $V_{\rho;\eta}^{(2)}$ corresponding to all the adjacent vertices have been computed. The way to proceed becomes clear through the circular embedding of the graph. The algorithm is detailed in the caption of Figure B.1. Here, we give a walk-through of the first two steps as follows. In the first step, we arbitrarily pick a vertex — we choose $(1,2)$ in this example. The calculation of $V_{3;4}^{(2)}$, $V_{1;4}^{(2)}$, $V_{4;3}^{(2)}$ and $V_{1;3}^{(2)}$ requires $V_{1;2}^{(1)}$. Therefore, we first find $V^{(2)}$ for these adjacent vertices and store them in the working arrays W_1, W_2, W_3 and W_4. Now, we are free to update $(1,2)$ with $V_{1;2}^{(2)}$. This requires $V_{3;4}^{(1)}$, $V_{1;4}^{(1)}$, $V_{4;3}^{(1)}$ and $V_{1;3}^{(1)}$, which still remain untouched in the adjacent vertices. This is the reason for the specific order of these updates described in the figure. Once $(1,2)$ is updated, no other vertex requires it and it gets disconnected from the graph. The second step proceeds similarly with respect to the vertex $(3,4)$. However, at the end of the second step, $(3,4)$ is updated to $V_{3,4}^{(2)}$, which was stored in W_1 during step 1. The rest of the steps of this algorithm proceed by repeating this procedure for a specific sequence of vertices, as shown in Figure B.1, such that only 7 working arrays are required at any point of the algorithm. The total memory cost for the working space in terms of array size is $63V_{lat}$ compared to $108V_{lat}$ in the brute-force method. This cost can be further reduced by appealing to unitarity: only two rows of W_i at each lattice point are required. This reduces the memory cost further to $42V_{lat}$.

The third sub-level is again straight-forward. Only 4 working arrays are needed to compute $V_\mu^{(3)}$ (due to the 4 values of μ).
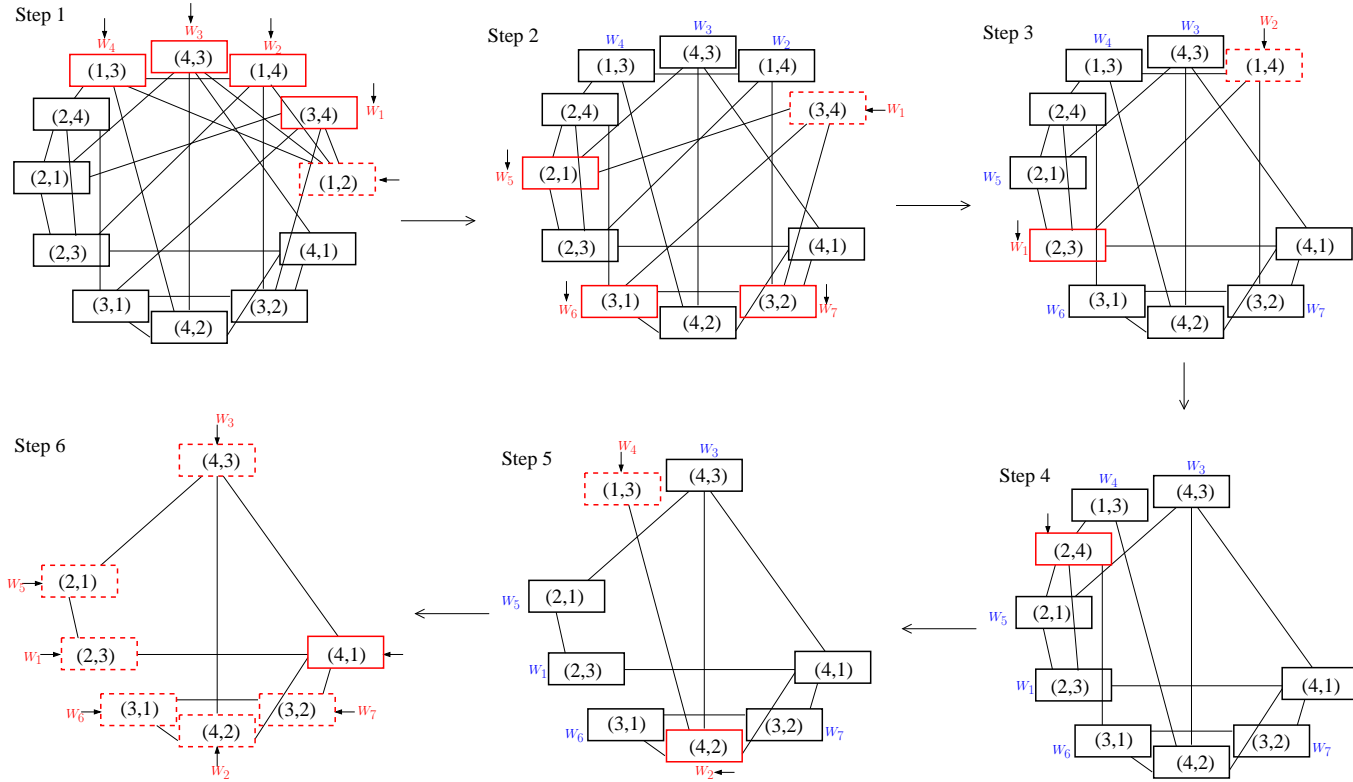
Figure B.1: Graphical illustration of memory optimized algorithm for the second sub-level of hypercubic schemes. The vertices (μ, ν) are the $9V_{lat}$ sized arrays, $V_{\mu;\nu}$, which stores 3×3 matrices at each lattice point. Two vertices, (μ, ν) and (ρ, η), are connected by an edge (*i.e.*, adjacent) if the construction of $V_{\mu;\nu}^{(2)}$ depends on $V_{\rho;\eta}^{(1)}$ (see eq. (3.4)), in which case $V_{\rho;\eta}^{(2)}$ also depends on $V_{\mu;\nu}^{(1)}$. There are 7 working arrays, W_i, which are indicated near some vertices and each of them are of size $9V_{lat}$. The algorithm proceeds from step 1 to 6 as shown in the figure. At the beginning of step 1, (μ, ν) contains $V_{\mu;\nu}^{(1)}$ at all lattice points. In each step, the red colored arrays are the ones which are relevant and the blue ones are dormant. Each step consists of the following operations. A short arrow with nothing at its tail, $\rightarrow W_i$ or $\rightarrow \boxed{(\mu, \nu)}$, indicates that $V_{\mu;\nu}^{(2)}$ is computed using $V_{\rho;\eta}^{(1)}$ contained in the vertices adjacent to (μ, ν) and stored in the array it points to. $W_i \rightarrow \boxed{(\mu, \nu)}$ means that data is copied from W_i to $V_{\mu;\nu}$. Solid or dashed red vertices indicate the order of these operations: the operations at the solid red vertices are done before the dashed ones, and amongst the solid vertices there is no hierarchy. Once $V_{\mu;\nu}$ is updated with $V_{\mu;\nu}^{(2)}$, the vertex and the edges attached to it are removed from the successive steps.

Bibliography

[1] J. Smit, *Introduction to Quantum Fields on a Lattice* (Cambridge University Press, 2002).

[2] T. DeGrand and C. DeTar, *Lattice Methods for Quantum Chromodynamics* (World Scientific Publishing Co. Pte. Ltd, 2006).

[3] C. Gattringer and C. B. Lang, *Quantum Chromodynamics on the Lattice* (Springer, 2010).

[4] L. Susskind, Phys.Rev. **D16**, 3031 (1977).

[5] M. F. Golterman, Nucl.Phys. **B273**, 663 (1986).

[6] M. Albanese et al. (APE Collaboration), Phys.Lett. **B192**, 163 (1987).

[7] C. Morningstar and M. J. Peardon, Phys.Rev. **D69**, 054501 (2004), hep-lat/0311018.

[8] A. Hasenfratz and F. Knechtli, Phys.Rev. **D64**, 034504 (2001), hep-lat/0103029.

[9] S. Capitani, S. Durr, and C. Hoelbling, JHEP **0611**, 028 (2006), hep-lat/0607006.

[10] C. E. Detar and J. B. Kogut, Phys.Rev.Lett. **59**, 399 (1987).

[11] M. Laine and M. Vepsalainen, JHEP **0402**, 004 (2004), hep-ph/0311268.

[12] W. Alberico, A. Beraudo, A. Czerska, P. Czerski, and A. Molinari, Nucl.Phys. **A792**, 152 (2007), hep-ph/0703298.

[13] B. B. Brandt, A. Francis, H. B. Meyer, H. Wittig, and O. Philipsen, PoS **LATTICE2012**, 073 (2012), 1210.6972.

[14] K. Orginos, D. Toussaint, and R. Sugar (MILC Collaboration), Phys.Rev. **D60**, 054503 (1999), `hep-lat/9903032`.

[15] E. Follana et al. (HPQCD Collaboration, UKQCD Collaboration), Nucl.Phys.Proc.Suppl. **129**, 384 (2004), `hep-lat/0406021`.

[16] T. Bae, D. H. Adams, C. Jung, . Kim, Hyung-Jin, J. Kim, et al., Phys.Rev. **D77**, 094508 (2008), `0801.3000`.

[17] K. Born et al. (MT(c) Collaboration), Phys.Rev.Lett. **67**, 302 (1991).

[18] D. Banerjee, R. V. Gavai, and S. Gupta, Phys.Rev. **D83**, 074510 (2011), `1102.4465`.

[19] M. Cheng, S. Datta, A. Francis, J. van der Heide, C. Jung, et al., Eur.Phys.J. **C71**, 1564 (2011), `1010.1216`.

[20] E. Laermann and F. Pucci, Eur.Phys.J. **C72**, 2200 (2012), `1207.6615`.

[21] R. Gavai, S. Gupta, and R. Lacaze, Phys.Rev. **D77**, 114506 (2008), `0803.0182`.

[22] D. J. Griffiths, *Introduction to Elementary Particles* (John Wiley & Sons, 1987).

[23] M. Breidenbach, J. I. Friedman, H. W. Kendall, E. D. Bloom, D. Coward, et al., Phys.Rev.Lett. **23**, 935 (1969).

[24] H. D. Politzer, Phys.Rept. **14**, 129 (1974).

[25] M. Gyulassy, pp. 159–182 (2004), `nucl-th/0403032`.

[26] M. L. Bellac, *Thermal Field Theory* (Cambridge University Press, 1996).

[27] K. G. Wilson, Phys.Rev. **D10**, 2445 (1974).

[28] E. Follana et al. (HPQCD Collaboration, UKQCD Collaboration), Phys.Rev. **D75**, 054502 (2007), `hep-lat/0610092`.

[29] R. Altmeyer et al. (MT(c) collaboration), Nucl.Phys. **B389**, 445 (1993).

[30] M. F. Golterman and J. Smit, Nucl.Phys. **B255**, 328 (1985).

[31] R. Gupta, G. Guralnik, G. W. Kilcup, and S. R. Sharpe, Phys.Rev. **D43**, 2003 (1991).

[32] S. Gusken, U. Low, K. Mutter, R. Sommer, A. Patel, et al., Phys.Lett. **B227**, 266 (1989).

[33] T. A. DeGrand and M. Hecht, Phys.Lett. **B275**, 435 (1992).

[34] S. A. Gottlieb, W. Liu, D. Toussaint, R. Renken, and R. Sugar, Phys.Rev. **D35**, 2531 (1987).

[35] K. Symanzik, Nucl.Phys. **B226**, 205 (1983).

[36] B. Sheikholeslami and R. Wohlert, Nucl.Phys. **B259**, 572 (1985).

[37] F. Karsch, E. Laermann, and A. Peikert, Nucl.Phys. **B605**, 579 (2001), hep-lat/0012023.

[38] M. Stephanov, PoS **LAT2006**, 024 (2006), hep-lat/0701002.

[39] Y. Aoki, G. Endrodi, Z. Fodor, S. Katz, and K. Szabo, Nature **443**, 675 (2006), hep-lat/0611014.

[40] A. Bazavov, T. Bhattacharya, M. Cheng, N. Christ, C. DeTar, et al., Phys.Rev. **D80**, 014504 (2009), 0903.4379.

[41] Y. Aoki, S. Borsanyi, S. Durr, Z. Fodor, S. D. Katz, et al., JHEP **0906**, 088 (2009), 0903.4155.

[42] A. Bazavov and P. Petreczky (HotQCD collaboration), J.Phys.Conf.Ser. **230**, 012014 (2010), 1005.1131.

[43] Z. Fodor and S. Katz, JHEP **0203**, 014 (2002), hep-lat/0106002.

[44] P. de Forcrand and O. Philipsen, Nucl.Phys. **B642**, 290 (2002), hep-lat/0205016.

[45] R. Gavai and S. Gupta, Phys.Rev. **D71**, 114014 (2005), hep-lat/0412035.

[46] S. Datta, R. V. Gavai, and S. Gupta, PoS **LAT2013**, 202 (2013).

[47] S. Datta, R. V. Gavai, and S. Gupta, Nucl.Phys. **A904-905**, 883c (2013), 1210.6784.

[48] S. Gupta, Phys.Rev. **D60**, 094505 (1999), hep-lat/9903019.

[49] M. Hamermesh, *Group Theory and its Applications to Physical Problems* (Addison-Wesley, 1962).

[50] A. Vuorinen, Phys.Rev. **D68**, 054017 (2003), `hep-ph/0305183`.

[51] E. Braaten and R. D. Pisarski, Nucl.Phys. **B337**, 569 (1990).

[52] J. Blaizot, E. Iancu, and A. Rebhan, Phys.Lett. **B523**, 143 (2001), `hep-ph/0110369`.

[53] Y. Schroder and M. Laine, PoS **LAT2005**, 180 (2006), `hep-lat/0509104`.

[54] S. Datta, S. Gupta, M. Padmanath, J. Maiti, and N. Mathur, JHEP **1302**, 145 (2013), `1212.2927`.

[55] R. Gavai, S. Gupta, and R. Lacaze, Phys.Rev. **D78**, 014502 (2008), `0803.1368`.

[56] A. Gocksch, P. Rossi, and U. M. Heller, Phys.Lett. **B205**, 334 (1988).

[57] R. Gavai and S. Gupta, Phys.Rev. **D78**, 114503 (2008), `0806.2233`.

[58] A. M. Ferrenberg and R. H. Swendsen, Phys.Rev.Lett. **63**, 1195 (1989).

[59] Y. Aoki, Z. Fodor, S. Katz, and K. Szabo, Phys.Lett. **B643**, 46 (2006), `hep-lat/0609068`.

[60] S. Datta and S. Gupta, Phys.Rev. **D80**, 114504 (2009), `0909.5591`.

[61] S. A. Gottlieb, W. Liu, R. Renken, R. Sugar, and D. Toussaint, Phys.Rev. **D38**, 2245 (1988).

[62] S. Gupta, Phys.Rev. **D64**, 034507 (2001), `hep-lat/0010011`.

[63] G. Martinelli, G. Parisi, and R. Petronzio, Phys.Lett. **B100**, 485 (1981).

[64] G. P. Lepage and P. B. Mackenzie, Phys.Rev. **D48**, 2250 (1993), `hep-lat/9209022`.

[65] S. Datta and S. Gupta, Nucl.Phys. **B534**, 392 (1998), `hep-lat/9806034`.

[66] J. W. Cooley and J. W. Tukey, Math. comput **19**, 297 (1965).

[67] G. H. Golub and C. F. Van Loan, *Matrix Computations* (Johns Hopkins University Press, 1996).

[68] S. Duane, A. Kennedy, B. Pendleton, and D. Roweth, Phys.Lett. **B195**, 216 (1987).

[69] J. R. Shewchuk, *An introduction to the conjugate gradient method without the agonizing pain* (1994).

[70] C. W. Bernard and T. A. DeGrand, Nucl.Phys.Proc.Suppl. **83**, 845 (2000), `hep-lat/9909083`.

[71] C. Bernard, C. E. DeTar, Z. Fu, and S. Prelovsek, Phys.Rev. **D76**, 094504 (2007), `0707.2402`.

[72] B. Efron, The annals of Statistics pp. 1–26 (1979).

[73] R. V. Gavai, S. Gupta, and R. Lacaze, Phys.Rev. **D65**, 094504 (2002), `hep-lat/0107022`.

[74] H. Ohno, U. Heller, F. Karsch, and S. Mukherjee, PoS **LATTICE2012**, 095 (2012), `1211.2591`.

[75] O. Kaczmarek, E. Laermann, and M. Mller (2013), `1311.3889`.

[76] J. Polonyi and H. Wyld, Phys.Rev.Lett. **51**, 2257 (1983).

[77] N. Metropolis, A. W. Rosenbluth, M. N. Rosenbluth, A. H. Teller, and E. Teller, The journal of chemical physics **21**, 1087 (2004).

[78] H. B. Meyer, H. Simma, R. Sommer, M. Della Morte, O. Witzel, et al., Comput.Phys.Commun. **176**, 91 (2007), `hep-lat/0606004`.

[79] P. B. Mackenzie, Phys.Lett. **B226**, 369 (1989).